Study of Plasma-surface Kinetics and Feature Profile Simulation of Poly-silicon Etching in Cl_2/HBr Plasma

by

Weidong Jin

B. E. Chemical Engineering
Tsinghua University, Beijing, 1997

M. S. Chemical Engineering Practice
Massachusetts Institute of Technology, 2001

Submitted to the Department of Chemical Engineering
in partial fulfillment of the requirements for the degree of

Doctor of Philosophy
in
Chemical Engineering

at the

Massachusetts Institute of Technology

December 2003
[February 2004]

© 2003 Massachusetts Institute of Technology
All rights reserved

Signature of Author ______________________________
Department of Chemical Engineering
December 14, 2003

Certified by ______________________________
Herbert H. Sawin
Professor of Chemical Engineering and
Electrical Engineering and Computer Science
Thesis Advisor

Accepted by ______________________________
Daniel Blankschtein
Professor of Chemical Engineering
Chairman, Committee for Graduate Students

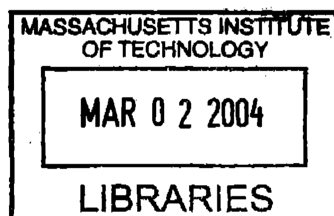
MASSACHUSETTS INSTITUTE OF TECHNOLOGY
MAR 0 2 2004
LIBRARIES

ARCHIVES

Study of Plasma-Surface Kinetics and Feature Profile Simulation of Poly-silicon Etching in Cl_2/HBr Plasma

by Weidong Jin

Submitted to the Department of Chemical Engineering on
December 14, 2003 in partial fulfillment of the requirements for
the degree of Doctor of Philosophy in Chemical Engineering

Abstract

This work characterized the Cl_2/HBr ion enhanced plasma-surface interactions with poly-silicon as a function of the gas composition, ion energy, ion incident angle and other important process parameters. A realistic inductively coupled plasma beam apparatus capable of generating ions and neutrals representative of real commercial etcher was constructed and utilized to simulate accurately a high density plasma environment. Etching rate of poly-silicon, the oxygen effect and loading effect are quantified to better describe the etching of patterned poly-silicon in fabricating the gate electrode of a transistor in VLSI manufacturing process. The kinetics model derived from these measurements are incorporated into a Monte Carlo based feature profile simulator, and profile evolution has been simulated under various processing conditions.

The realistic plasma beam was used to measure the etching yields of poly-silicon with Cl_2/HBr chemistry at different ion energies. The etching yields were found to scale linearly with $(\sqrt{E_{ion}} - \sqrt{E_{th}})$, where the threshold energies, E_{th}, are 10 eV for both Cl_2 and HBr. The etching yields at different neutral-to-ion flux ratio were measured and the sticking coefficients are derived for reactive neutrals for Cl_2 and HBr. The sticking coefficient for HBr system is lower probably due to the relatively larger size of bromine atom compared with chlorine and its relatively lower chemical reactivity. The etching yields for mixed Cl_2+HBr plasma at different compositions were also measured. The etching yield by the HBr plasma beam is similar to the Cl_2 plasma beam, although the etching rate by the HBr plasma is about 40% lower due to the lower ion flux. The angular dependence of etching yield by both Cl_2 and HBr strongly suggests the mechanism of ion enhanced chemical etching. With Cl_2 plasma beam, the etching yield almost keeps constant until the off-normal ion incident angle increased to 45°, while with the HBr plasma beam, the etching yield starts dropping even with small off-normal angle. The etching yield by Cl_2+HBr plasma at different composition exhibits a similar trend as pure HBr. The difference of angular dependent etching yield between Cl_2 and HBr might contribute to the difference of feature profile evolution in these two chemistries, i.e., more anisotropic etching in HBr plasma, as suggested by Monte Carlo feature profile evolution simulation.

The XPS peak for Cl(2*p*), Br(3*d*), and Si(2*p*) are integrated to quantify the relative concentration of different species on the sample surface after exposure to the plasma beam. The Cl coverage after etching with pure Cl_2 plasma beam is about 1.4 times higher than the Br coverage after etching with pure HBr plasma beam. The lower Br coverage is likely due to

site blocking by coadsorbed H and adjacent adsorption site blocking by the larger Br atom. The Si(*2p*) was deconvoluted to differentiate Si(bulk), SiCl, $SiCl_2$ and $SiCl_3$. About 70% of the chlorine adsorbed onto the surface is in the form of di- and tri-chloride. Similar results are observed for bromine. Inversion method was used to extract the depth profile from the angular resolved XPS measurement. The halogenation layer is about 15 – 25 Å thick, and the concentration of halogen decays exponentially as depth increases.

The effect of oxygen addition on the etching rate of poly-silicon was also studied. The etching rate has a different sensitivity to the oxygen addition with different surface composition. When the surface is chlorine rich, the etching rate is not sensitive to small amount of oxygen addition. When the surface is oxygen rich, the etching rate is more sensitive to oxygen addition. This explains that in a real commercial etcher, by adding small amount of oxygen, the poly-silicon etching rate does not change much, but the silicon oxide etching rate decreases significantly, therefore the etching selectivity can be improved.

The loading effect was studied by adding $SiCl_4$ into the feed gas to simulate the effect of etching product buildup in a real commercial etcher. The etching yield by the Cl_2 plasma beam is significantly reduced by the $SiCl_4$ addition due to the deposition of Si-containing species. The etching yield decreases drastically due to the ion enhanced deposition of Si-containing species as the concentration of $SiCl_4$ is low. As the active sites created by ion bombardment are filled with $SiCl_x$, further reduction of etching yield is due to the chemisorbtion on nonactive sites, which is much slower than ion-enhanced deposition but more temperature sensitive. A kinetics model has been developed to account for the effect of both ion-enhanced deposition and chemisorbtion on nonactive sites mechanism. The model represents the experimental data quantitatively well.

Feature profile evolution of poly-silicon gate etching under different conditions were obtained by Monte Carlo simulation and compared with experimental measurements. The neutral-to-ion ratio was found to result in the variation of surface chlorination, which could influence the feature profile evolution. Different ion energy would result in different ion directionality and the surface chlorination, thus influence the feature profile as well. Other facts, such as the mask angle, are also found to have some effects on the feature profile by our simulation, which agree with experimental results. The feature profile simulator was also used to simulate the dual damascene process, specifically the oxide fencing formation. The effect of various factors, including the via shape, etching selectivity, and etching chemistry was studied by the simulation and compared with experimental results from literature.

Thesis Advisor:
Herbert H. Sawin
Professor of Chemical Engineering and Electrical Engineering and Computer Science

Dedication

To my wife,

for loving me and supporting me everyday.

Acknowledgement

First of all, I would like to thank my thesis advisor, Professor Herbert H. Sawin, for being a great advisor offering guidance and providing support whenever I need. I am deeply indebted to Herb for showing great enthusiasm towards this project, and giving me insightful suggestions. I extend my thanks to my other committee members, Professor Karen Gleason and Professor Jackie Ying for their help and suggestions. I would like to acknowledge Semiconductor Research Corporation for their funding support to this project.

I'd like to thank the members of the Sawin Lab for sharing with me all the good time, for insightful discussions, for all the funny jokes, although some of them don't make a lot of sense to me. To Stacy, thanks for maintaining and fixing my computer and for the many technical and business talks over the last few years. Hang in there, you'll be out soon! To Ohseung, thanks for teaching me all the essential experimental skills and tricks, and helping me find those good deals. And thanks for making our office full of laughter and fun. Our group needs you, especially the "Ohseung button" on Herb's projector. To Steve and Brian, thanks for teaching me the plasma physics and etcher design during my initial stage in this lab. To Bo, thanks for always sharing your interesting ideas, although some of them may sound odd in the beginning. Thanks, Yunpeng and Hiroyo, for reminding me that I used to work hard.

I'd like to thank Peter and Glori for helping me order stuff, and correcting the forms that I filled out wrong. And also thank you for making the transactions in this lab running smooth.

I offer my sincere thanks to the staffs at the Microsystem Technology Center, machine shops for their technical support. Thanks for the group members of Professor Karen Gleason, whose names I don't know, for showing me how to use the ellipsometer.

I would thank my friends at MIT, in China, and in US for the conversations, emails, and spending some wonderful time together during vacations. Thank you for reminding me of the good old days.

Finally, I am thankful to my family for their love and encouragement.

Table of Contents

Abstract ... 3
Dedication ... 5
Acknowledgement ... 7
Table of Contents ... 9
List of Figures ... 12
List of Tables ... 18

1. Introduction ... 19

1.1. Fundamentals of plasma etching ... 21
1.2. Studies of ion enhanced Cl_2/HBr etching of silicon ... 23
1.2.1. Etching studies with plasma beam techniques ... 24
1.2.2. Etching studies in high density plasma reactors ... 26
1.2.3. Common etching artifacts ... 27
1.2.4. Studies of oxygen effect and loading effect ... 30
1.3. Feature profile evolution simulation ... 31
1.4. References ... 33

2. Experimental Apparatus and Diagnostics ... 37

2.1. Integrated Processing System ... 37
2.2. Plasma beam apparatus ... 38
2.2.1. Realistic plasma beam source ... 38
2.2.2. Plasma beam apparatus ... 41
2.3. Quartz crystal microbalance (QCM) ... 42
2.4. Ellipsometer ... 43
2.5. Gridded ion energy analyzer ... 45
2.6. Mass spectrometer ... 47
2.7. X-ray photoelectron spectroscopy ... 48
2.8. Reference ... 50

3. Beam Study of Poly-silicon Etching in Cl_2/HBr ... 51

3.1. Ion-enhanced etching yields versus ion energy ... 51
3.2. Ion-enhanced etching yields versus neutral-to-ion flux ratio ... 56
3.3. Ion-enhanced etching yields versus gas composition ... 59
3.4. Angular dependence of ion-enhanced etching yields ... 60
3.4.1. Angular dependent etching yield measurement ... 61
3.4.2. Effect of angular dependent etching yield on profile evolution ... 63
3.5. Mass spectrometer measurement of beam composition ... 67
3.6. Conclusions ... 69
3.7. References ... 70

4. XPS analysis of surface ... 73

4.1. XPS analysis of poly-silicon surface before etching.................................. 73
4.2. XPS analysis of poly-silicon surface after etching 74
4.2.1. Low resolution surface analysis.................................. 74
4.2.2. High resolution surface analysis.................................. 76
4.2.3. Deconvolution of Si(2p) spectral.................................. 80
4.3. Depth profile analysis.................................. 83
4.3.1. Depth profile inversion method.................................. 84
4.3.2. Depth profile for poly-silicon sample before etching.................................. 86
4.3.3. Depth profile for poly-silicon sample after etching by Cl_2 plasma beam..... 86
4.4. Conclusions.................................. 87
4.5. Reference.................................. 89

5. Beam Study of Oxygen Effect and Loading Effect.................................. 91

5.1. Oxygen effect on poly-silicon etching rate.................................. 92
5.1.1. The influence of oxygen addition on poly-silicon etching with Cl_2.......... 92
5.1.2. The influence of oxygen addition on poly-silicon etching with HBr.......... 93
5.1.3. Surface analysis after etching with oxygen addition.................................. 93
5.2. Loading effect on the etching rate.................................. 94
5.2.1. The influence of $SiCl_4$ addition on etching yield.................................. 94
5.2.2. The temperature effect on $SiCl_4$ reduction of etching yield.................................. 96
5.2.3. XPS analysis of surface. 98
5.2.4. Kinetics model.................................. 100
5.2.5. Implication of the kinetics model.................................. 103
5.3. Conclusions.................................. 104
5.4. References.................................. 105

6. Feature Profile Simulation of Poly-silicon Etching.................................. 107

6.1. Monte Carlo simulation.................................. 108
6.1.1. Simulations and the Monte Carlo methods.................................. 108
6.1.2. Random variable generation.................................. 108
6.2. Monte Carlo simulation for feature profile evolution.................................. 110
6.2.1. Monte Carlo model description.................................. 110
6.2.2. Estimation of ion energy from top power and bias power.................................. 112
6.2.3. Neutral and ion distribution functions.................................. 113
6.2.4. Estimate of neutral-to-ion flux ratio.................................. 114
6.3. Generalized kinetics model.................................. 114
6.4. Simulation results.................................. 116
6.4.1. Etching rates and aspect ratio dependent etching (ARDE) 116
6.4.2. Feature profile analysis.................................. 117
6.4.3. Simulated feature profile evolution and comparison with experimental results.................................. 121
6.5. Conclusion.................................. 128
6.6. References.................................. 129

7. Feature Profile Simulation of Dual Damascene Process.................................. 131

7.1. Surface kinetics model.................................. 132
7.2. Angular dependent etching yield.................................. 134

7.3. Simulation results and discussion........ 136
7.3.1. Effect of ion and neutral flux distribution........ 136
7.3.2. Effect of via shape........ 140
7.3.3. Effect of etching selectivity to BARC........ 141
7.3.4. Effect of etching chemistry........ 142
7.3.5. Inclusion of photoresist etching........ 144
7.4. Conclusion........ 145
7.5. References........ 146

8. Three-dimensional Profile Evolution Simulation........ 149

8.1. Introduction........ 149
8.2. Ion and neutral trajectories computation........ 150
8.3. Surface normal calculation........ 151
8.3.1. Six-point normal calculation........ 151
8.3.2. Least-square surface normal approximation for specular scattering........ 152
8.4. The validation of 3D simulation with 2-1/2D simulation........ 152
8.4.1. Etching with unit sticking probability for ions........ 153
8.4.2. Etching with angular dependent etching yield........ 153
8.4.3. Etching with angular dependent sticking probability........ 154
8.4.4. Surface roughness analysis........ 155
8.5. Conclusions........ 156
8.6. References........ 157

9. Conclusions........ 159

9.1. Conclusions........ 159
9.2. Suggestions for future work........ 161

Appendices........ 163
A. Mechanical drawings........ 163
B. Operating procedures........ 184

List of Figures

		Page
Figure 1-1	Historic trends and future projections for the minimum feature size used in integrated circuits in manufacturing.	19
Figure 1-2	Steps used to characterize the etching kinetics and implement profile simulation.	20
Figure 1-3	Plasma etching in integrated circuit manufacture: (a) example of isotropic etching; (b) illustrating the role of bombarding ions in anisotropic etching.	21
Figure 1-4	Inductively coupled plasma etcher with full wafer interferometry (FWI) and optical emission spectroscopy (OES) diagnostics.	22
Figure 1-5	Experimental demonstration of ion enhanced plasma etching.	23
Figure 1-6	The illustration of using scattering beam technique to simulate the effect of off-normal ions striking feature sidewall.	25
Figure 1-7	Commonly observed etching artifacts during poly-silicon gate etching process.	27
Figure 1-8	Example of two types of surface roughness: (a) isotropic roughness post-development; (b) anisotropic roughness after etching.	29
Figure 2-1	Schematic diagram of the integrated vacuum transfer system.	37
Figure 2-2	Schematic diagram of the realistic inductively coupled plasma beam source.	39
Figure 2-3	Measured ion flux profile with respect to the center of the sample.	40
Figure 2-4	Measured ion flux drift versus the time of plasma on.	40
Figure 2-5	Schematic diagram of the experimental system. A 4 inch high-density inductively coupled plasma side-chamber is working as a reactive beam source.	41
Figure 2-6	Experimental ellipsometric data and their theoretical fit for poly-silicon sample. (a) Psi, (b) Delta.	44
Figure 2-7	Schematic diagram of the gridded ion energy analyzer.	45
Figure 2-8	Characteristic ion energy distribution function measured by the gridded ion energy analyzer.	46

Figure 2-9	Argon ion beam characterization measured by a mass spectrometer.	48
Figure 2-10	Schematic diagram of the setup of the XPS system.	49
Figure 3-1	Etching yield of poly-silicon in Ar plasma as a function of incident ion energy compared to literature data.	52
Figure 3-2	The ion/neutral flux and etching rate as a function of distance from beam source.	54
Figure 3-3	The etching yield as a function of the neutral to ion flux ratio.	55
Figure 3-4	Etching yield of poly-silicon in chlorine plasma beam compared to literature data.	56
Figure 3-5	Etching yield of poly-silicon in HBr plasma beam.	56
Figure 3-6	The etching yield versus neutral-to-ion flux ratio of poly-silicon etching by 100 eV Cl_2 and HBr plasma beam, respectively.	57
Figure 3-7	Ion flux as a function of feed gas composition.	59
Figure 3-8	Etching yield of poly-silicon as a function of Cl_2 in Cl_2+HBr at different ion energies.	60
Figure 3-9	Etching yield of poly-silicon as a function of ion impingement angle.	62
Figure 3-10	Etching yield of poly-silicon as a function of ion impingement angle in Cl_2+HBr plasma.	63
Figure 3-11	Feature profile evolution by Monte Carlo simulation, assuming 100 eV ion energy, neutral-to-ion flux ratio=20:1, and ion angular distribution with FWHM of 5°: (a) $\alpha = 1$ and (b) $\alpha = 0.9$.	64
Figure 3-12	Feature profile evolution by Monte Carlo simulation, assuming 100 eV ion energy, neutral-to-ion flux ratio=20:1, and ion angular distribution with FWHM of 5°: (a) simulated profiles and (b) corresponding angular dependence of etching yield.	65
Figure 3-13	Feature profile evolution by simulation, assuming 100 eV ion energy, neutral-to-ion flux ratio=20:1, and ion angular distribution with FWHM of 5°: (a) etching in Cl_2 plasma and (b) etching in HBr plasma.	66
Figure 3-14	Cross sections of nominally 0.35 μm nested trenches etched with 250 W source power, 150 W bias power, 10 mTorr chamber pressure, 80 sccm flow rate in: (a) Cl_2; (b) HBr.	67

Figure 3-15 Mass spectra of ion flux from plasma beam source with pure Cl_2 and HBr plasmas. 68

Figure 3-16 Ion flux composition of mixed Cl_2+HBr plasma measured by mass spectrometer. 69

Figure 4-1 A survey spectrum of photoemission of the poly-silicon surface before etching. 73

Figure 4-2 A survey spectrum of photoemission of the poly-silicon surface after etching by 100 eV Cl_2 plasma beam. 75

Figure 4-3 A survey spectrum of photoemission of the poly-silicon surface after etching by 100 eV HBr plasma beam. 75

Figure 4-4 Photoemission of silicon and chlorine from a poly-silicon surface after etching by 100 eV Cl_2 plasma beam. 76

Figure 4-5 Photoemission spectra of Si(2p) and Cl(2p) from a poly-silicon surface after etching by 100 eV Cl_2 plasma beam. 77

Figure 4-6 XPS spectra of Cl (2p) and Br (3d) on poly-silicon after etching in Cl_2+HBr plasmas. 78

Figure 4-7 XPS integrated peak intensities [normalized to Si (*2p*) and corrected for sensitivity differences] after etching in Cl_2+HBr plasma. 78

Figure 4-8 QCM measurement of (a) film thickness and (b) etching rate under different plasma beam bombardment. 79

Figure 4-9 Photoemission spectra of Si(2p) from a poly-silicon surface after etching by 100 eV Cl_2 plasma beam. 81

Figure 4-10 Si(2p) XPS spectrum for poly-silicon after etching by 100 eV Cl_2 plasma beam. 81

Figure 4-11 Si(2p) XPS spectrum for poly-silicon after etching by 100 eV HBr plasma beam. 83

Figure 4-12 The illustration of surface sensitivity enhancement by variation of the electron take-off angle. 84

Figure 4-13 Signals from Si(2p) (underlying Si substrate), Si(2p) (from SiO_2), and O(1s) for a 20 SiO_2 film on a poly-silicon substrate vs. the XPS photoelectron take-off angle before etching. 84

Figure 4-14 Depth profile for a 20 SiO_2 film, computed from the inversion of the angle-resolved data presented in Figure 4-13. 85

Figure 4-15	Signal from Si(2p) and Cl(2p) vs. photoelectron take-off angle after etching by 100 eV Cl_2 plasma beam.	87
Figure 4-16	Depth profile of poly-silicon sample after etching by 100 eV Cl_2 plasma beam.	87
Figure 5-1	Effect of oxygen addition on the etching yield of silicon in Cl_2 discharge.	92
Figure 5-2	Comparison of effect of oxygen addition on silicon etching yield in Cl_2 discharge and HBr discharge at different ion bombardment energy. (a) 150 eV; (b) 50 eV.	93
Figure 5-3	Effect of oxygen addition on etching yield of silicon in Cl_2 discharge and surface composition.	94
Figure 5-4	The relative ion flux as a function of $SiCl_4$ concentration in the feed gas.	95
Figure 5-5	The etching rate as a function of $SiCl_4$ concentration in the feed gas.	95
Figure 5-6	The etching yield as a function of $SiCl_4$ concentration in the feed gas.	96
Figure 5-7	The etching yield as a function of $SiCl_4$ concentration under different substrate temperature.	97
Figure 5-8	The etching yield as a function of substrate temperature for different composition.	97
Figure 5-9	The etching yield as a function of substrate temperature under different ion energy level.	98
Figure 5-10	XPS spectra of Cl(*2p*) and Si(*2p*) on polysilicon after etching with 10% $SiCl_4$ in Cl_2.	99
Figure 5-11	XPS integrated peak intensities [normalized to Si(*2p*) and corrected for sensitivity differences] after etching in Cl_2 plasma beam with $SiCl_4$ addition.	99
Figure 6-1	The angular distribution of neutral and ion species.	113
Figure 6-2	Common artifacts observed during plasma etching.	116
Figure 6-3	Simulation results for etch rate vs. aspect ratio under various top powers and bias powers.	117
Figure 6-4	Simulated profile evolutions for different aspect ratio.	117

Figure 6-5 Illustration of the mechanism of microtrenching forming. 118

Figure 6-6 Two kind of profiles are studied for microtrenching mechanism: (a). Vertical sidewall. (b). Bowed sidewall. 119

Figure 6-7 The number of ions which fell into the interface cells for the first time, not including those scattered from other surfaces. 119

Figure 6-8 The number of ions which fell into and were stick to the interface cell. 120

Figure 6-9 Simulated feature profile evolutions with different neutral-to-ion ratio. 122

Figure 6-10 The etching rate for case shown in Figure 6-9 vs. aspect ratio. ... 122

Figure 6-11 Ion flux at bottom center for case shown in Figure 6-9(a) vs. aspect ratio. 123

Figure 6-12 Surface chlorination for various cases shown in Figure 6-9 at depth A, B and C respectively. 124

Figure 6-13 Schematic figure of feature profile evolution. 124

Figure 6-14 Experimental cross sections of 0.35 μm nested trenches etched with 500W top power and 150W bias power at 80 sccm Cl_2, the pressures are (a) 10 mTorr; (b) 2 mTorr. 125

Figure 6-15 Simulated feature profile evolutions for various ion energy. 126

Figure 6-16 Experimental cross section of 0.35 μm nested trenches etched with 500W top power and (a) 150W; (b) 250W; (c) 350W bias power at 10 mTorr, 80 sccm Cl_2. 126

Figure 6-17 Simulated feature profile evolution for 50eV ions with an angular distribution of 160eV ions. 127

Figure 6-18 Simulated feature profile evolution for different mask angles: (a) 83°; (b) 87°; (c) 90°. 128

Figure 7-1 Process Sequence for the via-first dual damascene integration scheme. 131

Figure 7-2 Scanning electron microscopy photograph of a via-first dual damascene trench etch illustrating oxide fencing around the via hole. 132

Figure 7-3 Angular dependent etching yield of SiO_2 in C_2F_6 and C_4F_8. 135

Figure 7-4 A typical profile evolution created by Monte Carlo simulation for

dual damascene etching process. 136

Figure 7-5 Effect of ion directionality on feature profile evolution by simulation. 137

Figure 7-6 Ion flux distribution along the etching surface for a specific feature profile during trench etch. 138

Figure 7-7 Continued profile evolution from the profile shown in Figure 7-6. . 139

Figure 7-8 Effect of shape of via hole on the profile evolution during the trench etching, simulation compared with experimental. 141

Figure 7-9 The effect of etching selectivity of SiO_2 to BARC on the profile evolution. 142

Figure 7-10 Two angular dependent etching yield curves for the study of effect of etching chemistry on profile evolution. 143

Figure 7-11 The effect of etching chemistry on profile evolution. 143

Figure 7-12 Comparison of simulated feature profile (a) without photoresist etching; (b) with photoresist etching, etching selectivity of SiO_2:PR=3:1. 144

Figure 8-1 Schematic diagram of the 3D simulation domain. 149

Figure 8-2 Sample feature for the comparison of neutral and ion flux calculated by 3D and 2-1/2D simulator, respectively. 150

Figure 8-3 Comparison of flux calculated by 3D simulator and 2-1/2D simulator for the structure shown in Figure 8-2. 151

Figure 8-4 Six-point surface normal computation 152

Figure 8-5 The comparison of feature profile simulated with 3D simulator and 2-1/2D simulator with unit sticking probability and no angular dependence of etching yield. 153

Figure 8-6 The comparison of feature profile simulated with 3D simulator and 2-1/2D simulator with unit scattering probability and angular dependence of etching yield. 153

Figure 8-7 The comparison of feature profile simulated with 3D simulator and 2-1/2D simulator with ion scattering turned on. 154

Figure 8-8 A typical simulated surface after etching (40x40 cells). 156

List of Tables

		Page
Table 1-1	References which contain values for silicon etching yields.	24
Table 3-1	Parameters for silicon etching yields as a function of ion energy, where $Y_{IE} = A(\sqrt{E} - \sqrt{E_{th}})$.	52
Table 3-2	The simplified phenomenological surface kinetics model for ion-enhanced poly-silicon etching with Cl_2 or HBr plasma beam.	58
Table 3-3	Model parameters for ion enhanced etching of poly-silicon by different neutral and ion systems at 100 eV ion energy.	59
Table 5-1	The simplified phenomenological surface kinetics model for Cl^+ ion-enhanced polysilicon etching with Cl.	101
Table 5-2	Model parameters for $SiCl_x$ deposition kinetics.	102
Table 6-1	The simplified phenomenological surface kinetics model for Cl^+ ion enhanced poly-silicon etching with Cl.	115

Chapter 1. Introduction

The objective of this work is to determine the plasma-surface interactions and incorporate the kinetics developed into the current simulation tools in our lab for design, optimization, and control of plasma etching processes. Specifically, the Cl_2/HBr ion enhanced plasma-surface interactions are characterized, as a function of the feed gas composition (relative amount of Cl_2 and HBr), ion energy, neutral-to-ion flux ratio, and ion incident angle. The kinetics measurements are used to formulate surface kinetics models that are incorporated into a profile simulator. Feature profile evolution is simulated for poly-silicon trench etching under various processing conditions.

Technology improvements over the past 40 years have resulted in a doubling of the number of transistors on a chip roughly every two years, a "law" that has become known as "Moore's law".[1] Decreasing components size is often characterized in integrated circuit (IC) technology by the minimum line width. This is usually defined as the smallest lateral feature size that is printed on the wafer surface during the fabrication process. This dimension is plotted in Figure 1-1 over the past 40 years and extrapolated into the future.[2] Devices with $0.13\,\mu m$ of minimum feature and 20 Å of gate oxide thickness are manufactured in 2002.

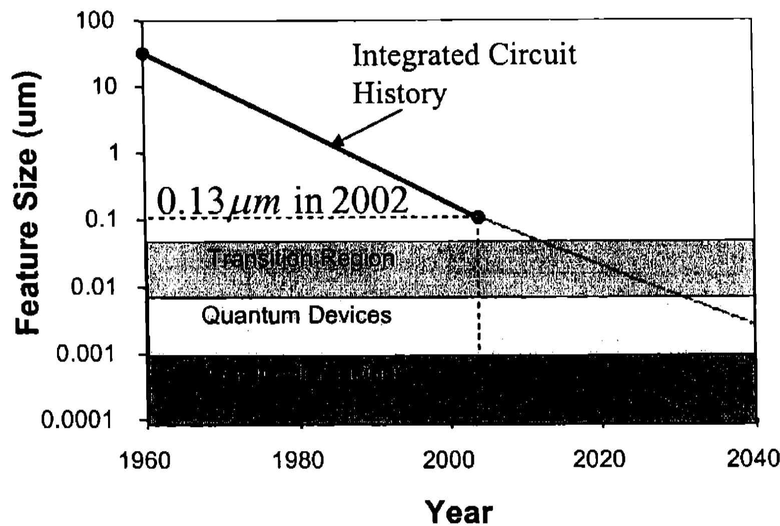

Figure 1-1: Historic trends and future projections for the minimum feature size used in integrated circuits in manufacturing.

The poly-silicon is used to fabricate gate electrodes in metal-oxide-silicon (MOS) electronic device. As the feature size has continued to scale down, the requirement on the poly-silicon etching process becomes more and more stringent. The Cl_2/HBr chemistry has been widely used for the plasma etching of patterned poly-silicon to achieve both the high etching rate and the good feature profile (i.e. the perfect anisotropic etching).[3] The success of poly-silicon etching step requires a thorough understanding of the reaction mechanisms to reduce the time and cost needed to optimize the process.

A realistic plasma beam apparatus is constructed and utilized to generate reactive neutrals and ions with a composition representative of that in a real commercial high density etcher to study the interaction of these species with poly-silicon. The rate coefficients of surface reactions are derived from the experimental measurements to allow development of profile simulators based rigorously on the kinetics measurement. A feature profile simulator using Monte Carlo method is used to simulate the feature profile evolution during poly-silicon gate etching under various processing conditions and the simulation results are compared with the real feature profile obtained by scanning electron microscopy (SEM) measurement.

The objective of this work is to combine the experimental work with simulation work to understand the ion enhanced plasma etching process and predict feature profile evolution. The methodology is illustrated below.

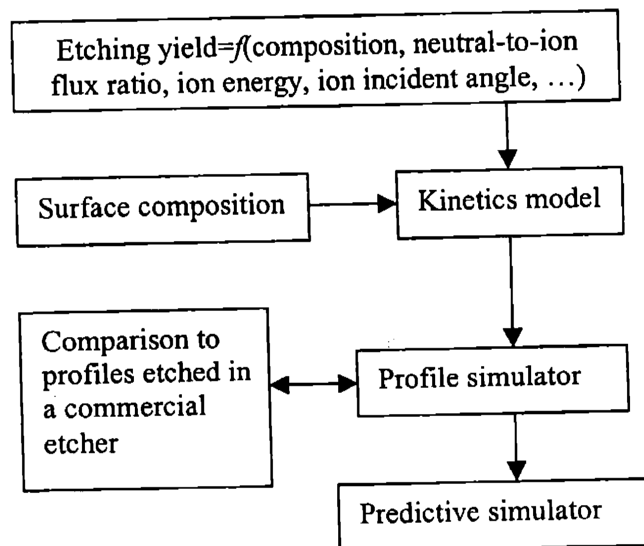

Figure 1-2: Steps used to characterize the etching kinetics and implement profile simulation.

1.1. Fundamentals of plasma etching

Plasma etching has been widely used in semiconductor industry to modify the surface properties of materials. Plasma-based surface processes are indispensable for manufacturing the very large scale integrated circuits (ICs) used by the electronics industry. The fabrications steps (deposit or grow, dope or modify, etch or remove) are repeated again and again in the manufacture of a modern integrated circuit. For microfabrication of an IC, one-third of the tens to hundreds of fabrication steps are typically plasma-based.

Faithful transfer of mask pattern into the underlayer can be accomplished by a plasma etching process that etches anisotropically. Exposing the mask film to a liquid (or vapor phase) etchant will lead to the undercut isotropic profile shown in Figure 1-3, which is produced by equal vertical and horizontal etching rates. The reduction in feature sizes and spacings makes anisotropic etching processes essential. Anisotropy is a critical process parameter in IC manufacture and has been a major force in driving the development of plasma processing technology.

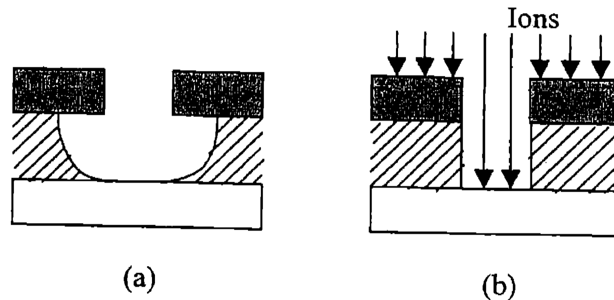

Figure 1-3: Plasma etching in integrated circuit manufacture: (a) example of isotropic etching; (b) illustrating the role of bombarding ions in anisotropic etching.

The selectivity is another critical process parameter for IC manufacture. It is preferred that the film is removed without damage to the mask or the underlying substrate layer (i.e. the infinite selectivity). Whereas wet etches have been developed having essentially infinite selectivity, highly selective plasma etching processes are not easily designed. Selectivity and anisotropy often compete in the design of a plasma etching process. One might imagine simply turning off the plasma after the film has been etched through to avoid the issue of selectivity, but this requires a good endpoint detection system. Even then, variations in film

thickness and etching rate across the area of the wafer imply that the etching cannot be stopped at the right moment everywhere.

A plasma is defined as a partially ionized gas in which the charged species have a sufficient concentration such that they interact significantly through Coulombic interactions. An electric current is passed through the plasma to accelerate free electrons that in turn excite and dissociate molecules to form energetic ions and reactive neutrals. Since electrons move much faster than ions, the surface in contact with the plasma very rapidly build up a negative charge, and thus a negative potential with respect to the plasma. This electric field then repels electrons and accelerates ions, and the extent of the negative potential is such that the flux of ions and electrons are equal (i.e. the formation of a sheath). Ions are accelerated across the plasma sheath with high energy, impinge the surface with high directionality, and enhance the surface reaction.

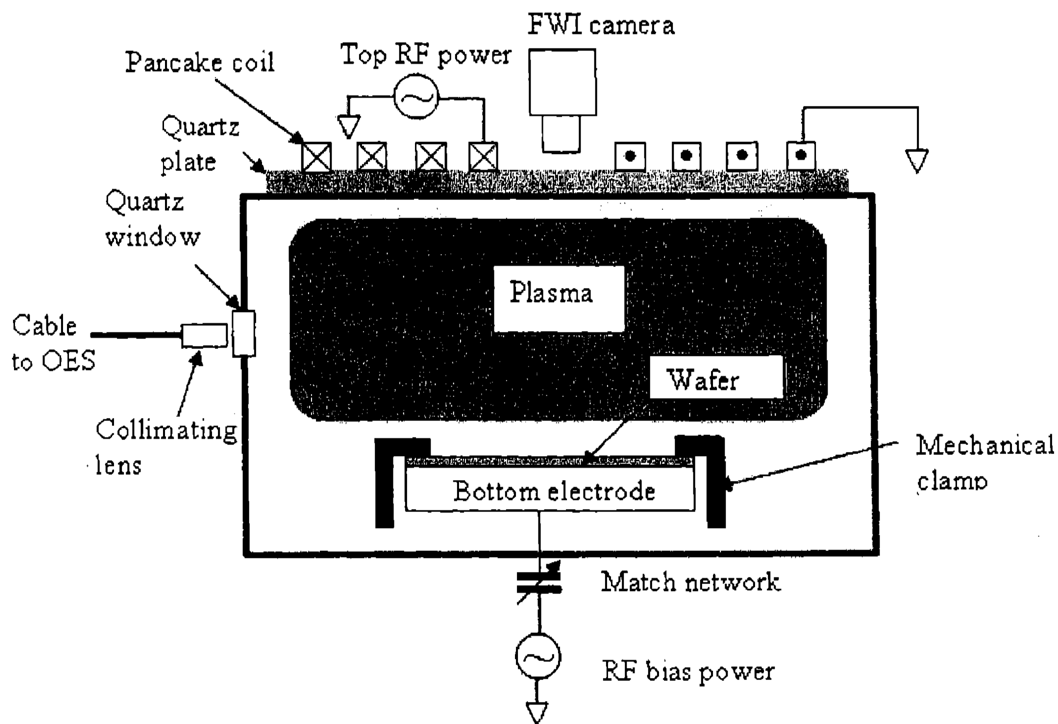

Figure 1-4: Inductively coupled plasma etcher with full wafer interferometry (FWI) and optical emission spectroscopy (OES) diagnostics. The pancake coil is powered by a 13.56 MHz rf power supply to generate the plasma, and the bottom electrode is powered by another rf power supply to control the ion bombardment energy.

Various high density plasma sources such as inductively coupled plasma (ICP) and electron cyclotron resonance (ECR) reactors have been developed for semiconductor microfabrication processes. Figure 1-4 is a schematic diagram of a high density ICP etcher developed in our lab.

Low pressure, high density plasma sources are favored in the integrated circuit manufacturing due to the increased control offered. The lower pressure (10 – 50 mTorr) reduces collisions in the plasma sheath, improving the ion bombardment directionality. Additionally, high density plasma sources allow for greater linewidth and selectivity control by offering the ability to independently control the ion flux and ion energy by varying the power to the plasma source and wafer chunk.[4] Therefore, both directional etching and reasonable selectivity are possible.[5]

1.2. Studies of ion enhanced Cl_2/HBr etching of silicon

In order to accurately simulate the poly-silicon etching process by Cl_2/HBr chemistry, the etching kinetics must be determined. There have been a number of beam studies performed using Cl_2 and F_2 systems that measure the etching yields using separate ion and neutral flux beams to simulate the flux from a plasma.[6-8] Due to the difficulty in creating ion beam sources using reactive gases, often "surrogate" Ar^+ ions are employed to simulate the effect of Cl^+, Cl_2^+, F^+, or other ions.

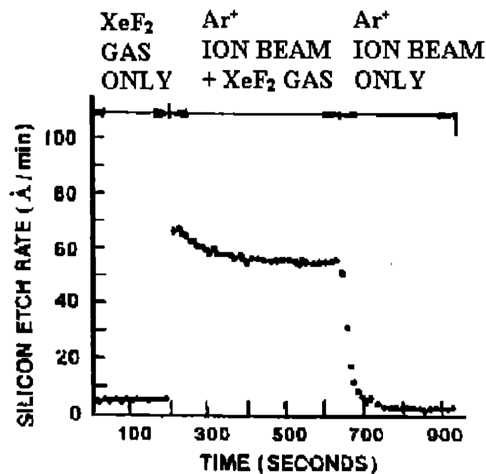

Figure 1-5: Experimental demonstration of ion enhanced plasma etching. (Coburn and Winters, 1979).

The synergistic effect between energetic ions and reactive neutrals has been known for many years, as illustrated by the experimental data in Figure 1-5.[8] In time sequence, this shows first, the equilibrium chemical etching rate of silicon in the XeF_2 etchant gas; next, the tenfold increase in etch rate with the addition of argon ion bombardment of the substrate, simulating plasma assisted etching; and finally, the very low etching rate due to the physical sputtering of silicon by the ion bombardment alone.

1.2.1. Etching studies with plasma beam techniques

To explore the etching of silicon in high density plasma source, we need to identify the role of major ionic and neutral species. Direct beam scattering technique has been developed to generate reactive plasma species in the form of a beam to allow determination of the functional roles of each reactive species. One advantage of the beam scattering technique is that the chemical reactions in the bulk plasma is isolated from the surface reactions and the beams are better characterized in term of the compositions, the energy distribution and the angular distribution. This technique has been widely used in the literature to characterize the ion enhanced plasma etching reactions. An incomplete list of references to other work which have measured silicon etching yields are given in Table 1-1.

Table 1-1: References which contain values for silicon etching yields. All references provide etching yields as a function of ion energy over the range indicated.

Ions	Neutrals	Ion energy (eV)	Ref.
Ar^+	Cl, Cl_2	65 - 300	9
Ar^+	Cl, Cl_2	35 - 100	10
Ar^+	Cl_2	1000	11, 12
Ar^+	Cl_2	200 - 1000	13
Ar^+	Cl_2	90 - 300	14
Ar^+	F	20 - 350	15
Ar^+	F	1000	16
Ar^+	SF_6	500 - 1000	17
Ar^+	XeF_2	1000	18, 19
Ar^+, CF_3^+	XeF_2	500 - 2000	20
Ar^+, Cl^+, CF_x^+	Cl_2	200 – 1200	21
Ar^+, Cl^+, Cl_2^+	Cl_2	40 – 900	22
Ar^+, Cl^+, Cl_2^+	Cl_2	350	23
Ar^+, He^+, Ne^+	XeF_2, Cl_2	1000	24
Ar^+, He^+, Ne^+, Kr^+, F^+, Cl^+, Br^+		100 – 3000	25
Ar^+, Kr^+, Xe^+, Cl_2^+, Cl^+, CCl_x^+	Cl_2	40 - 1000	26

Ar^+, O_2^+, O^+	Cl, Cl_2	500 - 1000	27
Cl^+	Cl	35 - 75	6
Cl^+	Cl, Cl_2	35 - 75	28
Cl^+, Cl_2^+	Cl, Cl_2	50 - 150	29
Cl^+, Cl_2^+, F^+, CF_x^+	Cl, Cl_2, CF_x	200 - 1200	7
F^+, SF_x^+	F, SF_x	100 - 400	30

As far as we know, there is only one study involving bromine.[25] There are no reported etching yields using HBr neutrals or ions, or Cl_2+HBr mixtures, in spite of the fact that common commercial recipe for poly-silicon etching uses a mixture of Cl_2 and HBr. Vitale used a realistic high density plasma beam source to generate ionic and neutral species representative of the composition in commercial etcher so that the difficulty of building multiple beam systems to generate the numerous ions and neutrals is avoided.[31] And the "species-averaged" etching yield data are measured that can be incorporated into a lumped kinetics models. We apply the similar approach in this work to characterize the role of major ionic and neutral species and quantify the etching yields under the parameter space.

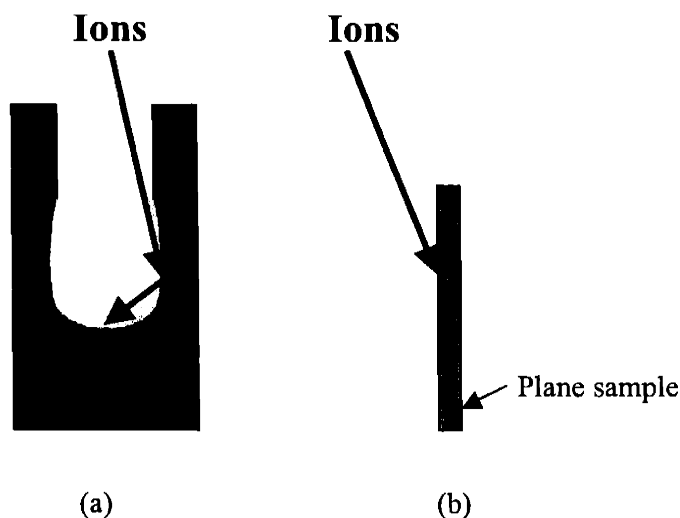

Figure 1-6: Illustration of using scattering beam technique to simulate the effect of off-normal ions striking feature sidewall: (a) off-normal ions striking sidewall of a patterned sample in a real etcher; (b) simulation of the effect by scattering beam technique.

The other advantage of beam scattering technique is that it can help capture the physics difficult, if not impossible, to determine using a real commercial etcher and patterned sample. For example, since the ion directionality is not perfect, feature sidewall will be exposed to bombardment by off-normal ions, as illustrated in Figure 1-6. To accurately

simulate the etching process, the effect of the off-normal ions on the etching, the surface composition, and the surface roughness has to be investigated. Due to the extreme small feature size (on the order of 0.1 μm), it is difficult to probe the feature sidewall using any analytical tool. However, by adjusting the ion incident angle on a flat sample using the scattering beam technique, the effect of off-normal ions striking sidewall can be simulated. The etching rate can be easily measured either *in-situ* or *ex-situ*, and the surface composition and roughness can also be analyzed by traditional surface analysis technique.

1.2.2. Etching studies in high density plasma reactors

In addition to beam experiments, researchers have also performed numerous studies using patterned samples in high density plasma sources where ions and neutral fluxes are less well characterized. These studies are more relevant to industrial application, and the observed phenomena can be used to validate the etching kinetics developed using scattering beam technique and calibrate the feature profile simulator.

Cheng *et. al.* used XPS and real-time, laser-induced thermal desorption – laser–induced fluorescence (LD-LIF) to determine the coverage of Br and Cl on Si (100) surfaces that are etched by mixed HBr/Cl_2 plasmas in a helical resonator plasma reactor.[32] LD-LIF was detected from $SiCl_{(g)}$ and $SiBr_{(g)}$ products with intensities that are a semiquantitative measure of instantaneous Cl and Br coverages. Saturated coverages during etching in Cl_2 and HBr plasmas are 1.0×10^{15} Cl/cm^2 and 6.0×10^{14} Br/cm^2, respectively.

Layadi *et. al.* investigated the interaction of a Cl_2 plasma with a Si(100) surface by angle resolved XPS.[33] They found that the amount of chlorine incorporated into the near-surface region of Si increases with ion energy, from 1.8×10^{15} Cl/cm^2 at 40 eV to 3.5×10^{15} Cl/cm^2 at 280 eV. From an inversion of the observed take-off angle dependence of the relative Cl and Si XPS signals, depth profiles were derived for the near-surface region. Cl content falls off in a graded fashion, over a depth of about 25 Å and 13 Å for mean ion energies of 280 eV and 40 eV, respectively.

Lane *et. al.* studied the effect of source power, bias power, chamber pressure, flow rate, and feed gas composition on profile evolution measured by scanning electron

microscopy (SEM) during poly-silicon etching with an oxide hardmask in an inductively coupled plasma system.[34] Microtrench formation was found to be a strong function of the plasma condition. A correlation between sidewall shape and microtrench development was observed. The large data set as plasma parameters are varied is valuable for validating feature profile simulations.

1.2.3. Common etching artifacts

For most etching processes, it is desirable to create a perfectly anisotropic feature profiles and uniform etching in features with different sizes and across the wafer. However, it is difficult to achieve these two goals simultaneously, and etching artifacts are often observed. Mahorowala's Ph.D. thesis summarized commonly observed etching artifacts.[35] Figure 1-7 shows the commonly observed artifacts during plasma etching, and each of the artifact is briefly described below.

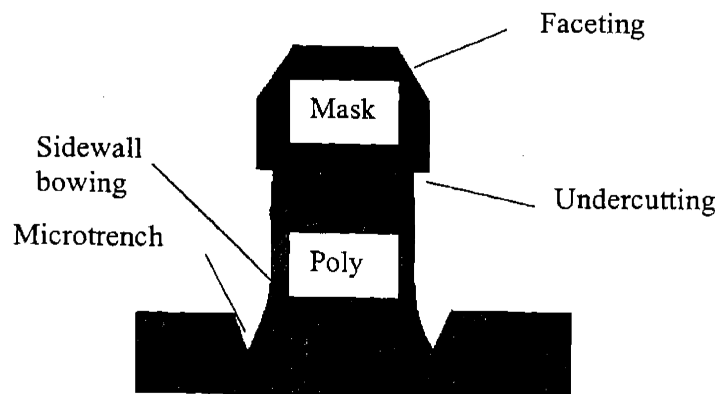

Figure 1-7: Commonly observed etching artifacts during poly-silicon gate etching process. The etching artifacts shown include: mask faceting, sidewall bowing, microtrenching, undercutting. Other etching artifacts not shown can include: notching, surface roughness, etc.

ARDE

Aspect ratio dependent etching or ARDE refers to the phenomenon that etching rate depends on the aspect ratio of the feature. Often observed is the reactive ion etching lag or RIE lag, in which smaller features etch slower than larger features.[36] Various factors such as neutral species transport, ion shadowing, neutral shadowing, feature charging and deposition of passivants can lead to RIE lag. Sometimes reverse RIE lag, in which smaller features etch

faster than larger features, can be observed. This has been attributed to the fact that depositing species is more likely to deposit onto the sidewall in a deep feature, resulting in relatively less deposition on the feature bottom.

Faceting

When physical sputtering is the dominant method of material removal, rectangular features do not retain their original profiles; they develop facets.[37] Sputtering rates are dependent on the ion incident angle and for most materials peak at an angle of about 60° off-normal. Faceting usually starts at feature corners that always have some rounding, and therefore present a variety of incident angles to the incoming ions. A facet develops for the plane that has the highest sputtering yield.

Sidewall bowing

Bowing or barreling refers to the curvature of the sidewalls. Bowing can be caused by a variety of factors, *e.g.* non-directional ions, smaller etching yields for off-normal ions and sidewall deposition.[38,39] Sidewall bowing affects the critical dimension (CD) of the feature and can cause microtrenching at the feature bottom.

Microtrenching

Microtrenching, sometimes called arches or dovetails, is the enhanced erosion around the foot of an etched sidewall.[38-41] Typically, it is caused by the increased ion flux of ions at the trenches due to reflection from tapered/bowed sidewalls or possibly bending of ion trajectories because of charging effects. Microtrenching is undesirable during the poly-silicon etching step because the thin gate oxide might get sputtered/etched at the microtrench locations causing the MOS transistor failure.

Undercutting

Undercutting refers to the lateral etching into a layer and can be considered as extreme sidewall bowing. Typically, undercutting occurs at the interface of two materials when one material is resistant to the etching species, *e.g.* immediately below an etch-resistant

mask. The undercutting has been attributed to ion scattering off the neighboring hardmask, or the etching enhanced by the tension between two materials.[42]

Surface roughening or sidewall roughening

Surface roughness is the average surface irregularity, *i.e.* microscopic pillars of the materials being etched. Figure 1-8 shows two types of feature sidewall roughness during oxide etching: isotropic and anisotropic.[43] Post-development roughness is typically isotropic; an atomic force microscopy (AFM) image shows agglomerates of different sizes. After etching, the sidewall roughness might have a preferred direction or in other words it might be anisotropic, *e.g.* striations on the sidewall. Isotropic and anisotropic sidewall roughness characteristics are expected to impact the substrate in different fashions.

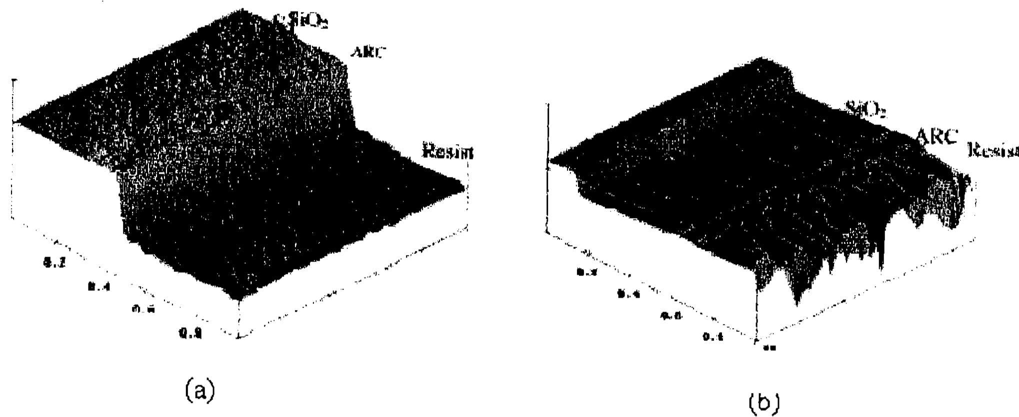

Figure 1-8: Example of two types of surface roughness: (a) isotropic roughness post-development; (b) anisotropic roughness after etching.

Notching

Notching is the lateral etching at the foot of sidewall and is commonly observed during overetching (additional etching step to remove unetched material left due to non-uniformities in the etching process) of poly-silicon over an insulating material, *e.g.* oxide. Notches are formed at the interface of the conducting and insulating materials. Interface stresses and ion trajectory distortion combined are believed to cause this artifact.[44]

1.2.4. Studies of oxygen effect and loading effect

As the gate oxide thickness shrinks to ~20 Å, high etching selectivity of silicon-to-oxide is needed to remove silicon layer without damaging the underlying thin oxide layer. To achieve the high etching selectivity, O_2 has been added into the feed gas. Tuda *et. al.* studied the profile evolution during poly-silicon gate etching with low pressure, high density electron cyclotron resonance $Cl_2/HBr/O_2$ plasma.[3] Bell *et. al.* used XPS to study the chemical constituents present on the surfaces after poly-silicon features etched in a low pressure, high density plasma, helicon source using a $HBr/Cl_2/O_2$ gas mixture.[45] The O_2 gas flow rate was tuned to obtain anisotropic etching profiles by forming a SiO_2 like layer on the sidewalls of the features and maximizing the poly-silicon/gate oxide selectivity. XPS analyses have shown that the passivation layer formed on the poly-silicon sidewalls during etching is a chlorine rich silicon oxide film.

Due to the high etching rate in a low-pressure, high-density inductively coupled plasma etching process, the etching products can build up to appreciable concentrations and correspondingly the reactant is depleted, and result in the so-called loading effect. In addition to the depletion of reactants, which decreases the etchant species surface coverage, etching products can be fragmented upon collision with energetic electrons, with subsequent deposition on the substrate and chamber walls.[46,47] Therefore, high pumping speed is needed to sweep the etching products out of the chamber. The etching product can deposit on the substrate surface, both in the form of ions and neutrals, and modify surface conditions, affecting the etching uniformity, and other etching properties such as RIE lag. The deposition on the feature sidewall can also affect the feature profile.

In this work, we use the plasma beam to study both the oxygen effect and loading effect by adding O_2 and $SiCl_4$ in the feed gas respectively. The etching yields at different O_2 and Si addition are measured to quantify their respective effects, and the surface compositions after etching are also analyzed to help us understand the role of O and Si adsorption onto the surface.

1.3. Feature profile evolution simulation

It is important to be able to simulate the plasma etching processes because the large number of independent processing parameters makes purely empirical studies tedious and time consuming. Furthermore, empirical studies do not provide a basis for understanding the etching rates, etching profiles, selectivity, and process latitudes that are observed in plasma etching processes.

To date, simulation work has given invaluable insight into the surface profile evolution during ion-enhanced plasma etching, using various techniques such as string algorithm[48], characteristics method[49], shock-tracing method[50], and direct simulation Monte Carlo[51] (DSMC) method, *etc*. These methods fall into three general categories:

String methods

The surface is represented by a string of points (nodes) connected by straight line segments. The positions of the nodes are updated by determining front information about the normals and curvature; the surface normal being approximated by the bisector of the inwardly pointing normals to the two adjacent segments. The point velocity is taken as the average of the two segment etching rates. It is difficult to include all the physics and chemistry that determine the reactive particles' fluxes on the surface. Additional, composition dependent properties of the surface cannot be taken into account while advancing the surface.

Level set methods

Level set methods are robust, fast and accurate when tracking complicated interface motions.[52] They can handle topological merging and breaking naturally. They approximate the equations of motion of the underlying propagating surface, which resemble Hamilton-Jacobi equations with parabolic right-hand sides. The moving front is viewed as a particular level set of a higher dimensional function. However, it is still difficult to include all the physics and chemistry involved in the practical etching problem. Besides, this method is a deterministic method, which makes it impossible to simulate the stochastic behavior during the etching process, such as the surface roughness.

Cell-based methods

The computational domain is divided into an array of cells that contain various volume fractions and different materials. The cell boundaries are used to reconstruct the surface. It is relatively easier to include all the physics and chemistry during the etching process, and handle surface composition dependence of properties using these methods. These methods can simulate more complicated materials, such as porous material, by incorporating empty holes in the computational domain at random.[53] These methods can be stochastic, therefore can be used to study the surface roughness. However, simulations based on these methods require more memory and are slower.

For these methods, dominant reaction mechanisms incorporated in these simulators include ion induced etching and ion reflection. Commonly observed etching peculiarities in plasma etching processes such as bowing, tapering, undercutting and microtrenching are predicted as different physical or chemical mechanisms are incorporated. But there is little side-by-side comparison between simulated results and observed feature profiles. In this work, we use Monte Carlo method associated with the kinetics model from beam studies to simulate feature profile evolution of poly-silicon trench etching under different processing conditions and relate etching artifacts observed in the simulation to neutral and ion flux distribution, ion angular dependent etching yield, and surface coverage.

Due to the generality of the feature profile simulator, it can also be used to simulate other etching/deposition process during the integrated circuit fabrication process, such as the dual damascene process. Increasingly complex devices that have three-dimensional (3D) structure require improved dimensionality in profile simulators to capture the most important features. To correctly capture the surface roughness also requires 3D simulation. In this thesis, we also aim to do some preliminary work of construction of a 3D simulator and validating it by running some test cases and comparing results with those from the current 2-1/2D simulator.

1.4. References

1. Gordon Moore was one of the founders of Intel and first pointed out this "law" around 1970.

2. James D. Plummer, Michael Deal, Peter B. Griffin, Silicon VLSI Technology, (Prentice Hall, 2000).

3. M. Tuda, K. Shintani, and H. Ootera, *J. Vac. Sci. Technol. A* **19**, 711 (2001).

4. Lieberman, M. A., and R. A. Gottscho. Physics of Thin Films: Advances in Research and Development. Ed. J. Vossen. New York: Academic Press, 1993.

5. J. W. Coburn, *Appl. Phys. A.: Solids Surf.* A **49**, 451 (1994).

6. J. P. Chang, A. P. Mahorowala, and H. H. Sawin, *J. Vac. Sci. Technol. A* **16**, 217 (1998).

7. T. M. Mayer, R. A. Barker, and L. J. Whitman, *J. Vac. Sci. Technol.* **18**, 349 (1981).

8. J. W. Coburn and H. F. Winters, *J. Appl. Phys.* **50**, 3189 (1979).

9. J. A. Levinson, E. S. G. Shaqfeh, M. Balooch, and A. V. Hamza, *J. Vac. Sci. Technol. B* **18**, 172 (2000).

10. J. P. Chang, J. C. Arnold, G. C. Zau, H.-S. Shin, and H. H. Sawin, *J. Vac. Sci. Technol. A* **15**, 1853 (1997).

11. J. W. Coburn, *J. Vac. Sci. Technol. B* **12**, 1384 (1994).

12. N. A. Takasaki, E. Ikawa, and Y. Kurogi, *J. Vac. Sci. Technol. B* **4**, 806 (1986).

13. R. S. Goodman, N. Materer, and S. R. Leone, *J. Vac. Sci. Technol. A* **17**, 3340 (1999).

14. J. A. Levinson, E. S. G. Shaqfeq, M. Balooch, and A. V. Hamza, *J. Vac. Sci. Technol. A* **15**, 1902 (1997).

15. D. C. Gray, I. Tepermeister, and H. H. Sawin, *J. Vac. Sci. Technol. B* **11**, 1243 (1993).

16. C. B. Mullins and J. W. Coburn, *J. Appl. Phys.* **76**, 7562 (1994).

17. K. Affolter, *J. Vac. Sci. Technol. B* **7**, 19 (1989).

18. M. J. M. Vugts, L. J. F. Hermans, and H. C. W. Beijerinck, *J. Vac. Sci. Technol. A* **14**, 2138 (1996).

19. H. F. Winters and J. W. Coburn, *J. Vac. Sci. Technol. B* **3**, 1376 (1985).

20. Y.-Y. Tu, T. J. Chuang, and H. F. Winters, *Phys. Rev. B* **23**, 823 (1981).

21. T. M. Mayer and R. A. Barker, *J. Vac. Sci. Technol.* **21**, 757 (1982).

22. M. Balooch, M. Moalem, W. E. Wang, and A. V. Hamza, *J. Vac. Sci. Technol. A* **14**, 229 (1996).

23. H. Okano and Y. Horiike, *Jpn. J. Appl. Phys., Part 1* **20**, 2429 (1981).

24. U. Gerlach-Meyer, J. W. Coburn, and E. Kay, *Surf. Sci.* **103**, 177 (1981).

25. S. Tachi and S. Ohudaira, *J. Vac. Sci. Technol. B* **4**, 459 (1986).

26. C. Steinbruchel, *Appl. Phys. Lett.* **55**, 1960 (1989).

27. G. P. Kota, J. W. Coburn, and D. B. Graves, *J. Vac. Sci. Technol. A* **16**, 2215 (1998).

28. J. P. Chang and H. H. Sawin, *J. Vac. Sci. Technol. A* **15**, 610 (1997).

29. C. C. Cheng, K. V. Guinn, V. M. Donnelly, and I. P. Herman, *J. Vac. Sci. Technol. A* **12**, 2630 (1994).

30. T. Chevolleau, P. Y. Tessier, C. Cardinaud, and G. Turban, *J. Vac. Sci. Technol. A* **15**, 2661 (1997).

31. S. A. Vitale, H. Chae, and H. H. Sawin, *J. Vac. Sci. Technol. A* **19**, 2197 (2001).

32. C. C. Cheng, K. V. Guinn, I. P. Herman, and V. M. Donnelly, *J. Vac. Sci. Technol. A* **13**, 1970 (1995).

33. N. Layadi, V. M. Donnelly, and J. T. C. Lee, *J. Appl. Phys.* **81**, 6738 (1997).

34. J. M. Lane, F. P. Klemens, K. H. A. Bogart, M. V. Malyshev, and J. T. C. Lee, *J. Vac. Sci. Technol. A* **18**, 188 (2000).

35. A. P. Mahorowala, Ph.D. thesis, Massachusetts Institute of Technology, 1999.

36. R. A. Gottscho, C. W. Jurgensen, and D. J. Vitkavage, *J. Vac. Sci. Technol. B* **10**, 2133 (1992).

37. B. Chapman, Glow Discharge Processes, John Wiley & Sons, New York (1980).

38. G. S. Hwang, C. M. Anderson, M. J. Gordon, T. A. Moore, T. K. Minton, and K. P. Giapis, *Phys. Rev. Lett.* **77**, 3049 (1996).

39. S. V. Nguyen, D. Dobuzinsky, S. R. Stiffler, and G. Chrisman, *J. Electrochem. Soc.* **138**, 1112 (1991).

40. A. C. Westerheim, A. H. Labun, J. H. Dubash, J. C. Arnold, H. H. Sawin, and V. Yu-Wang, *J. Vac. Sci. Technol. A* **13**, 853 (1995).

41. R. J. Hoekstra, M. J. Jushner, V. Sukharev, and P. Schoenborn, *J. Vac. Sci. Technol. B* **16**, 2102 (1998).

42. S. Ohki, M. Oda, H. Akiya, and T. Shibata, *J. Vac. Sci. Technol. B* **5**, 1611 (1987).

43. A. P. Mahorowala, D. L. Goldfarb, K. Temple, et. al., *Prodeedings of SPIE* **5039**, 213 (2003).

44. J. P. Chang and H. H. Sawin, *J. Vac. Sci. Technol. B* **19**, 1870 (2001).

45. F. H. Bell and O. Joubert, *J. Vac. Sci. Technol. B* **15**, 88 (1997).

46. K. Tsujimoto, T. Kumihashi, and S. Tachi, *Appl. Phys. Lett.* **63**, 1915 (1993).

47. D. C. Gray, V. Homindra, and H. H. Sawin, *J. Vac. Sci. Technol. A* **12**, 354 (1994).

48. J. I. F.Ulacia and J. P. McVittie, *J. Appl. Phys.* **65**, 1484 (1989).

49. E. S. G. Shaqfeh and C. W. Jurgensen, *J. Appl. Phys.* **66**, 4664 (1989).

50. S. Hamaguchi and M. Dalvie, *J. Vac. Sci. Technol. A* **12**, 2745 (1994).

51. R. N. Tait, S. K. Dew, T. Smy, and M. J. Brett, *J. Vac. Sci. Technol. A* **12**, 1085 (1994).

52. D. Adalsteinsson, J. A. Sethian, *J. Comp. Phys.* **120**, 128 (1995).

53. A. Sankaran and M. J. Kushner, *Appl. Phys. Lett.* **82**, 1824 (2003).

Chapter 2. Experimental Apparatus and Diagnostics

The experiments for this thesis work were performed mainly in a homemade realistic plasma beam chamber. In order to accurately simulate a high-density Cl_2/HBr plasma, a realistic plasma works as the beam source to create neutrals and ions representative of those in a high density plasma reactor. Normal poly-silicon samples are cut from 4 inch wafer and are used to study etching rate dependence and surface composition. A quartz crystal microbalance (QCM) is also installed in the chamber to facilitate fast measurement and accurate temperature control. Various diagnostic tools, including ellipsometer, X-ray photoelectron spectroscopy, ion energy analyzer and mass spectrometer, are used.

2.1. Integrated Processing System

An integrated processing system was fabricated to increase the material processing capability, and the plasma beam apparatus is connected to a 34 feet long, vacuum transfers tube as shown in Figure 2-1.

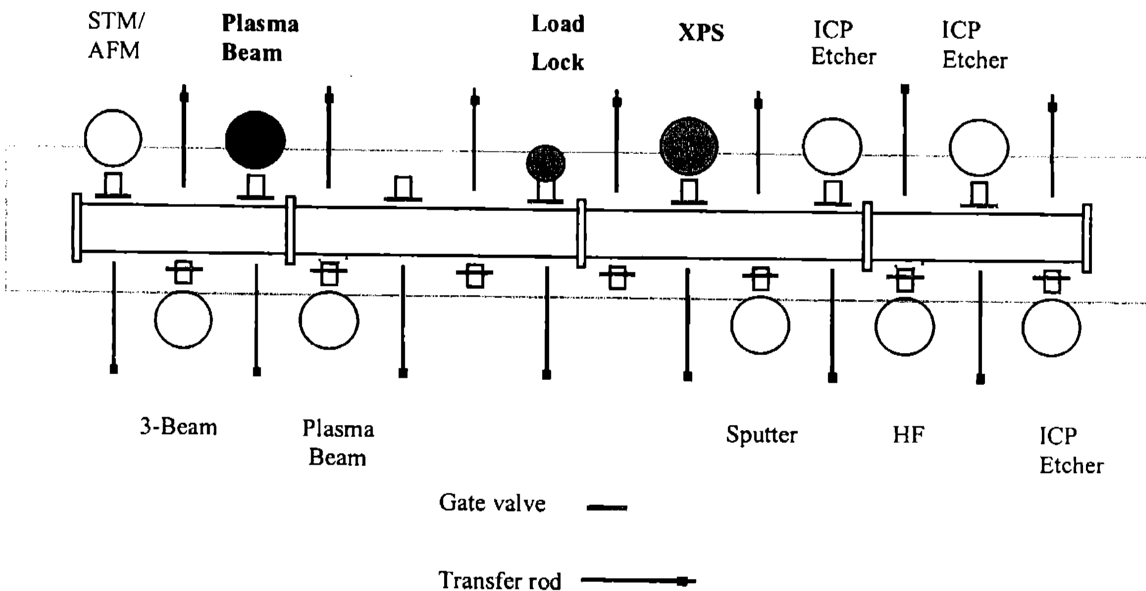

Figure 2-1: Schematic diagram of the integrated vacuum transfer system. This system allows *in situ* vacuum transfer of a sample between various process chambers to achieve integrated material processing, which is required as the process criteria becomes more stringent. An

analysis chamber equipped with X-ray photoelectron spectroscopy allows *in situ* surface analysis after processes.

The vacuum transfer tube facilitates *in situ* sample transfer, and is evacuated by two 4000 l/s cryogenic pumps (CTI Cryogenics Cryo-torr 8), with a base pressure of 4×10^{-9} Torr. A load-lock chamber is available on the transfer system for the introduction of thin film samples into the vacuum transfer tube and thereby the plasma beam chamber. An analytical chamber equipped with an X-ray photoelectron spectrometer is also available on the transfer system for post-etching surface analysis. In this setup, samples can be rotated in the analytical chamber to allow angular resolved XPS (AR-XPS) analysis, as detailed in Section 4.3.

2.2. Plasma beam apparatus

To isolate the gas phase reactions from the surface reactions, beam study has been widely used in the literature. Well-controlled neutrals and ion beams are extracted from beam source into the main chamber, where they interact with the sample surface. With this technique, the effect of major ionic and neutral species can be identified.

2.2.1. Realistic plasma beam source

Due to the difficulty of building multiple beam systems capable of generating the numerous ionic and neutral species present in real plasmas, a realistic high density plasma was employed as the beam source. The plasma beam apparatus consists of an 8 inch diameter stainless steel reaction vessel evacuated by a 4000 l/s cryogenic pump (CTI Cryogenics Cryo-torr 8). The chamber pressure is maintained at 10^{-5} Torr under typical operations.

The cross-sectional view of this beam source is illustrated in detail in Figure 2-2. The inductively coupled plasma source consists of a stainless steel cylinder (4 inch in diameter and 6 inch in length), a dielectric window, a three turn copper coil powered at 13.56 MHz (up to 650 W) via a match box. Although the beam source was designed to be inductively coupled plasma source, it is mainly capacitively coupled due to the small window to deposit the power.

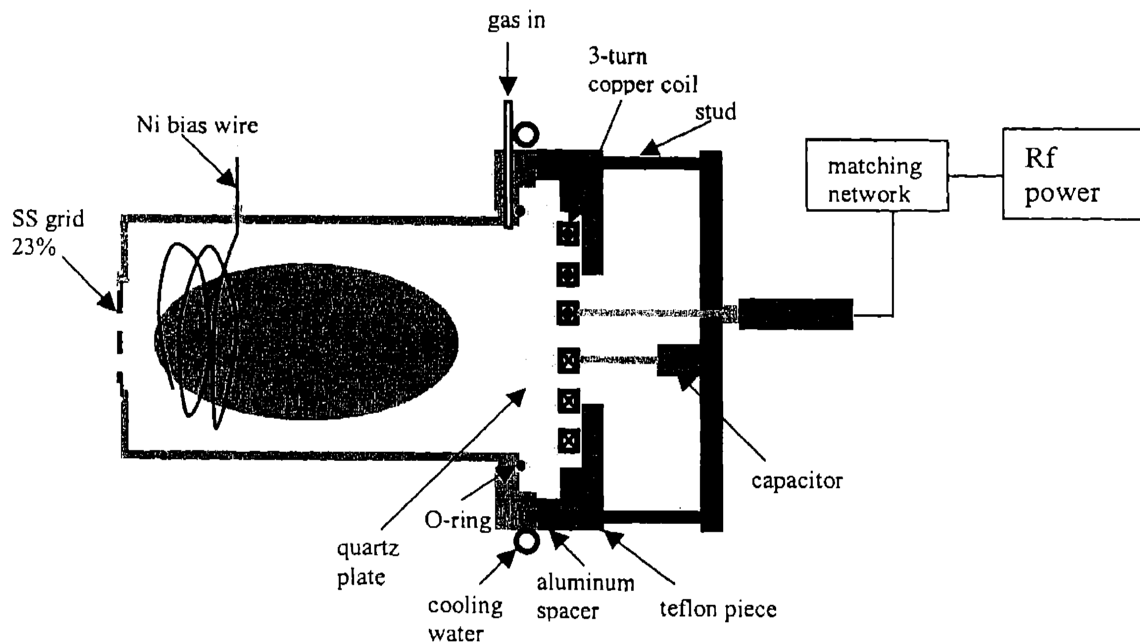

Figure 2-2: Realistic plasma beam source. The inductively coupled plasma source consists of a stainless steel cylinder, a dielectric window, a three turn copper coil powered at 13.56 MHz (up to 650 W) via a match box. The plasma can be raised to a DC potential above ground to accelerate the ions to the sample. Neutrals and ions representative of a real plasma reactor are extracted from the beam source into the main chamber to study the etching kientics.

The plasma is raised to a DC potential above ground to accelerate the ions to the sample. The biasing is performed in a manner similar to that used for the ECR source, detailed in Chang's Ph.D. thesis.[1] A 0.050" Ni wire runs from a BNC feedthrough to the plasma source position. Since the inner surface of the beam cylinder is covered with quartz liner, the plasma will adopt a potential of 15 to 25 volts above that of the wire, thus the plasma potential above ground can be controlled. The ions are then accelerated through the front extraction grid, which is a Buckbee-Mears #512 stainless steel grid, 23% opening, 0.005" thick, with 0.006" electroformed holes. An electron-emitting steel filament is used in front of the beam source to reduce the ion space charge and to prevent the non-conductive samples from charging. We actually observed that due to the relatively low ion flux from the beam source, even if we do not turn on the neutralization filament, the ion broading is minimal. So in our case, the main role of the filament is to prevent the charging on the sample. If we use poly-silicon sample, which is conductive, the surface charging is also negligible. The etching rate measurement with the filament on and off shows little difference. But for insulating material, for example, silicon oxide or OSG, the surface charging can have significant effect on the etching rate.

The ion flux measured at the sample position is fairly uniform, with less than 10% variation across a 1 cm × 1 cm silicon die, as shown in Figure 2-3. The time dependence of ion flux is shown in Figure 2-4. The ion flux is fairly constant within short period of time (1 hour or so), and the long term variation is probably due to the temperature drift of the plasma beam source when the wall is heated up.

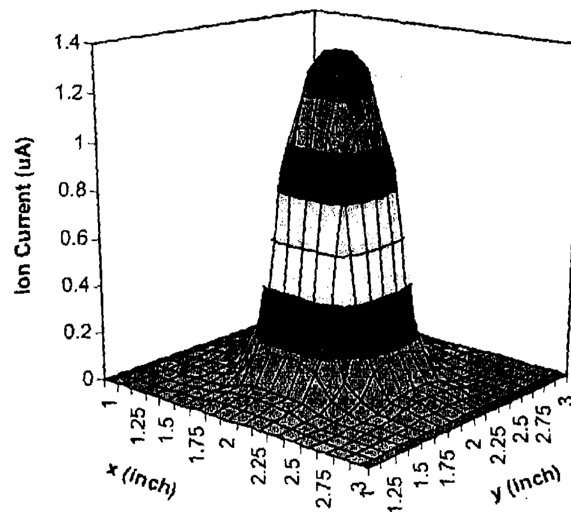

Figure 2-3: Measured ion flux profile with respect to the center of the sample (the center of the sample is located at x=2 inch, y=2 inch). The ion flux was fairly uniform over the entire sample (~ 1 cm x 1 cm). The size of the extraction hole is 0.5 inch in diameter.

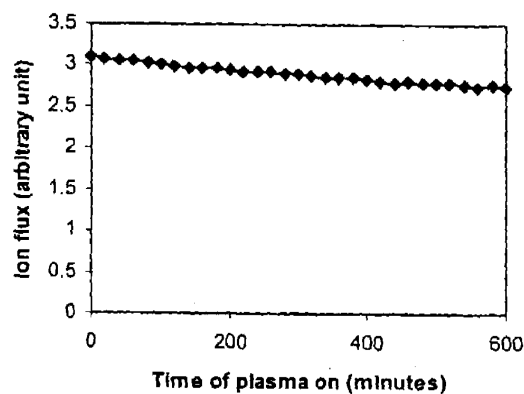

Figure 2-4: Measured ion flux drift versus the time of plasma on. The ion flux is fairly constant within 1 hour, and the long term drift is probably due to the temperature change of plasma beam source when it is heated by the plasma.

2.2.2. Plasma beam apparatus

To decouple the gas phase chemistry from the surface chemistry, a vacuum beam system can be used. In these systems, the sample surface under vacuum (10^{-5} Torr) is exposed to relatively well-characterized and controlled beams of species. The plasma beam/QCM is shown in Figure 2-5. The beam apparatus used in this study consists of an 8 inch diameter stainless steel reaction vessel evacuated by a 4000 l/s cryogenic pump (CTI Cryogenics Cryo-torr 8). Ions and neutrals are extracted from the plasma source through the grounded extraction grid, and then transported into the main chamber.

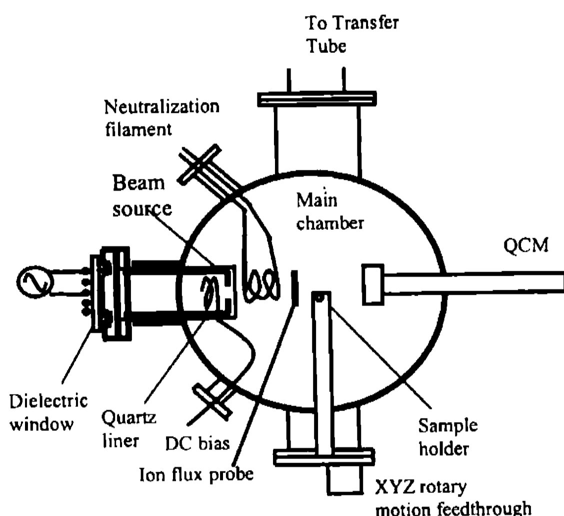

Figure 2-5: Schematic diagram of the experimental system. A 4 inch high-density inductively coupled plasma side-chamber is working as a reactive beam source. Normal poly-silicon sample cut from 4 inch wafer can be mounted onto the sample holder to study the etching rate dependence and surface composition during etching. The sample holder can be rotated to change the ion incident angle to study the angular dependence of etching yield. QCM is also used to facilitate fast measurement and accurate temperature control. The ion flux is measured by a ion flux probe simultaneously.

A quartz crystal microbalance (QCM) is mounted on the main chamber, facing the plasma source. The QCM sensor crystals are coated with 5000 Å of amorphous Si deposited by PECVD. The QCM sensor is water cooled, which allows sensitive measurement of the etching yields under various conditions.

A sample holder is mounted on the main chamber to allow the use of normal poly-silicon sample in the surface composition analysis after etching. The 1 cm × 1 cm sample, cut from 4 inch poly-silicon wafers, was stripped in aqueous hydrofluoric acid for 1 minute to

remove the native oxide layer, rinsed with de-ionized water, and dried in N_2 gas, and then transferred into the main chamber through a load-lock and 10^{-9} Torr sample transfer tube. The main chamber is also connected through the transfer tube to an analytical chamber where X-ray photoelectron spectroscopy (XPS) of the films can be taken after etching.

2.3. Quartz crystal microbalance (QCM)

Surface kinetics was studied by measuring etching and deposition rate of various materials in the QCM sample located in the main chamber. The main chamber is pumped by a 4000 l/s cryogenic pump (CTI Cryogenics Cryo-torr 8) and the base pressure of 10^{-8} Torr is maintained. With the gas flow rate of 1 sccm, 10^{-5}-10^{-4} Torr of pressure was maintained. Kinetic parameters of ion energy, neutral to ion flux ratio, and ion impingement angle are changed. Ion-to-neutral flux ratio varied by changing the distance between plasma and QCM and the distance can be varied from 1-3 inch.

Poly-silicon etching rate on the QCM sample was acquired under different parameter combinations. AT-cut gold covered 6 MHz quartz crystals are used in this research. The exposed portion of the quartz crystal is 0.32 inch in diameter. A brief description of the operation principle of the QCM is given in Chae's Ph.D. thesis.[2] But for the completeness of this thesis, the main mechanism of QCM operation is cited below.

A piezoelectric crystal changes shape when a voltage is applied across it. The extent of the deformation is proportional to the applied voltage. Certain resonant conditions exist in the crystal when it is properly cut and shaped, and a suitable exciting voltage is applied. When material is added or removed from an exposed face of the crystal, the crystal's resonant frequency changes. Increased mass loading decreases the resonant frequency, while material removal increases the resonant frequency. As a result, changes in mass can be monitored via changes in the oscillation frequency.

$$\frac{m_f}{m_q} = \frac{\rho_f t_f}{\rho_q t_q} = \left(\frac{f_q - f_c}{f_q}\right) \quad (2\text{-}1)$$

The area mass density of the coated crystal, m_f, is proportional to the change in the oscillation frequency of the coated, f_c, from the uncoated crystal, f_q. The area mass

densities, m_f and m_q (uncoated quartz) can be expressed as the product of their density, ρ, and thickness, t, to yield the following expression for the thickness of the deposited film:

$$t_f = \frac{(f_q - f_c)N_q\rho_q}{f_q^2\rho_f} \qquad (2\text{-}2)$$

where, N_q ($= f_q t_q$ =166.1 kHz cm) is the frequency constant for an AT-cut quartz crystal.

2.4. Ellipsometer

Ellipsometry is a very sensitive surface and thin film measurement technique that uses polarized light.[3] Ellipsometry measures the change in polarization state of light reflected from the surface of a sample. Fundamentally, ellipsometry refers just to the measurement of the polarization state of a light beam. However, ellipsometric measurements are usually performed in order to describe an "optical system" that modifies the polarization state of a beam of light. For thin film sample analysis, the "optical system" is simply the reflection of light from the sample. The measured values are expressed as psi (Ψ) and delta (Δ).

Ellipsometry can be used to determine thin film thickness, thin film optical constants, and in many cases both thickness and optical constants of the same film. Ellipsometry works best for film characterization when the film is not too much smaller or larger than the wavelength of the light used for the measurement. It is relatively difficult to use a probe of 500 nm (or so) wavelength to characterize a 0.5 nm or 10000 nm thick film, whereas films from 5 nm to 1000 nm are much simpler to characterize in general.

Ellipsometry measures polarization states, which are affected by the physical sample parameters we are interested in (layer thickness, etc.) such that by measuring these optical quantities (Ψ and Δ) we can infer the values of the physical parameters we are actually interested in. Having obtained optical measurements that are a function of some physical parameters we are interested in, we must now construct a model from which we can accurately predict what we should measure from a sample of known properties. This model should contain some known parameters, such as the wavelength of the incident light, the incident beam polarization state, and the angle of incidence. The model should also contain

some unknown physical parameters, such as layer thickness and optical constants. We can then vary the unknown physical parameters and calculate data until we find a set of the variable parameters which yields calculated data very closely matching our measured optical data. It is our hope that these parameters then accurately represent the true physical structure of the sample under study.

The film thickness was evaluated using a Woollam Co. VASE® variable angle spectroscopic ellipsometer equipped with WVASE32™ data analysis software. The ellipsometer consisted of a light source, a monochromator, collimating optics, a polarizer, a sample holder, a rotating analyzer, and a detector. Simultaneously, the system acquired a spectrum ranging from 2600 Å to 7200 Å with 20 Å interval. The ellipsometer measurements were taken using three different angles of incidence: 65°, 70°, and 75°. The spectroscopic ellipsometry (SE) data were fitted with a four-layer model (20 Å SiO_2 + 5000 Å p-si + 1000 Å SiO_2 + 1 mm Si), and these numbers are just initial guess that will be adjusted to yield the best fit. Parametric semiconductor layer is used to model the p-si layer, and for the other three layers, standard models are directly lifted from the database. Shown in Figure 2-6 are the SE data and model fits for a typical poly-silicon sample. It's evident that the model fits the experimental data quite well, and the thickness of poly-silicon layer can be monitored by this method accurately.

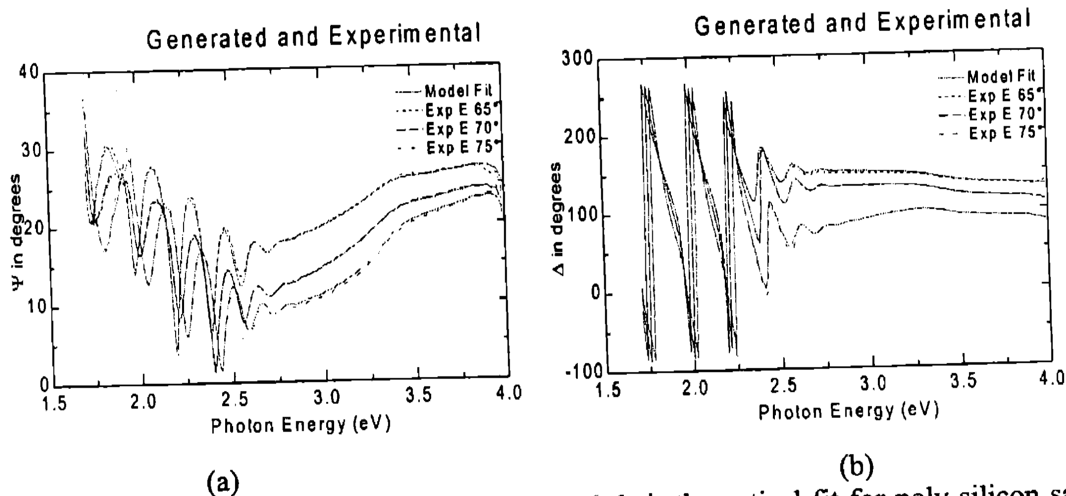

(a) (b)

Figure 2-6: Experimental ellipsometric data and their theoretical fit for poly-silicon sample. (a) Psi, (b) Delta. The good agreement between experimental data and theoretic fit indicates that the selected model can represent the real surface quite well and measurement of film thickness with this technique is accurate.

2.5. Gridded ion energy analyzer

The gridded ion analyzer used in this work was constructed by Chang and Gibson.[4] A schematic diagram of the ion energy analyzer is shown in Figure 2-7.

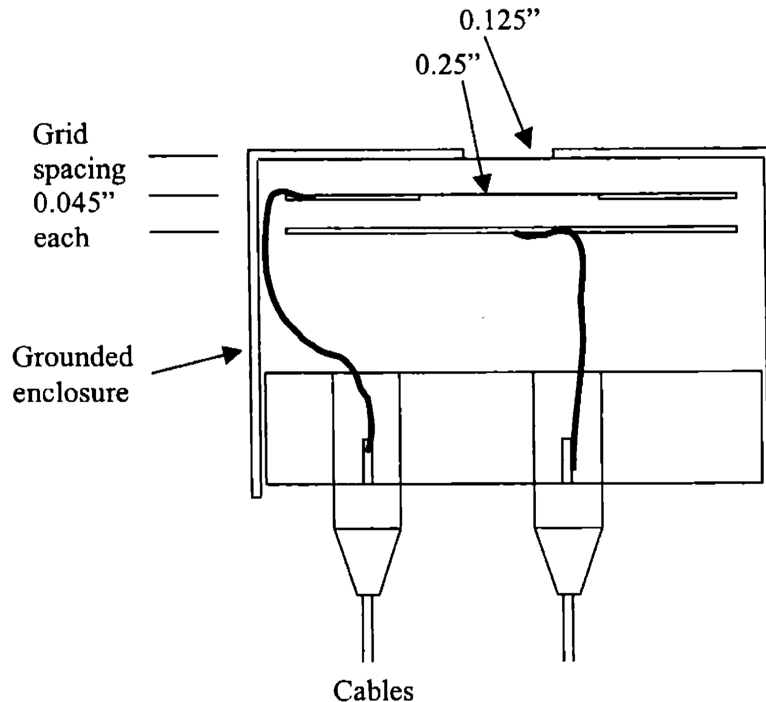

Figure 2-7: Schematic diagram of the gridded ion energy analyzer. The analyzer consists of a stainless steel can with a 0.125" orifice at the center of the front plate, one stainless steel disk with an orifice at the center (repeller), a stainless steel disk (collector), and a 0.2" thick stainless steel plate with two built-in microdot connectors and one mounting screw. The two orifices were covered with stainless meshes, alumina spacers were used to separate the stainless disks and the can, and Teflon screws were used to assemble the analyzer in place.

A stainless steel can with a 0.125" orifice at the center of the front plate is used as a ground shield. A stainless steel disk with a 0.25" orifice at the center is used as electron repeller, and a stainless steel disk as ion collector. A 0.2" thick stainless steel plate with two built-in microdot connectors and one mounting screw serves as the enclosure of the analyzer and provides electrical connections to the analyzer. The two orifices were covered with stainless meshes (0.003" holes, 0.002" thick, #228 Buckbee-Mears), alumina spacers were used to separate the stainless disks and the can, and Teflon screws were used to assemble the analyzer in place. It is worth noting that the inter-grid spacing was chosen to be on the order

of 0.045", which is smaller than the mean free path of the ions, to avoid the broadening of the IEDF due to collisions and minimize the effect of space charge corruption.

Ions enter the grounded orifice and stainless-steel grid that was used to minimize charging of insulating surfaces in the ion beam path. The electron repeller disk covered with fine stainless steel mesh was electrically connected to the a power supply and was biased to -100 eV to repel electrons as well as return secondary electrons created at the collector. The collector disk is electrically connected to a floating picoammeter (Keithley 485) and is biased positively to obtain proper IEDFs. As the biasing voltage increases, only ions with sufficient energy to overcome the potential hill will impinge upon the collector. Therefore, the collected current is the integral of the distribution function for ions,

$$I(V_c) = \int_{eV_c}^{\infty} f(E)dE \qquad (2\text{-}3)$$

Therefore, the ion energy distribution function is proportional to the derivative of the I-V curve measured from the ion energy analyzer

$$f(E) = -\frac{1}{\int_0^{\infty} f(E)dE}\frac{dI}{dV_c} \qquad (2\text{-}4)$$

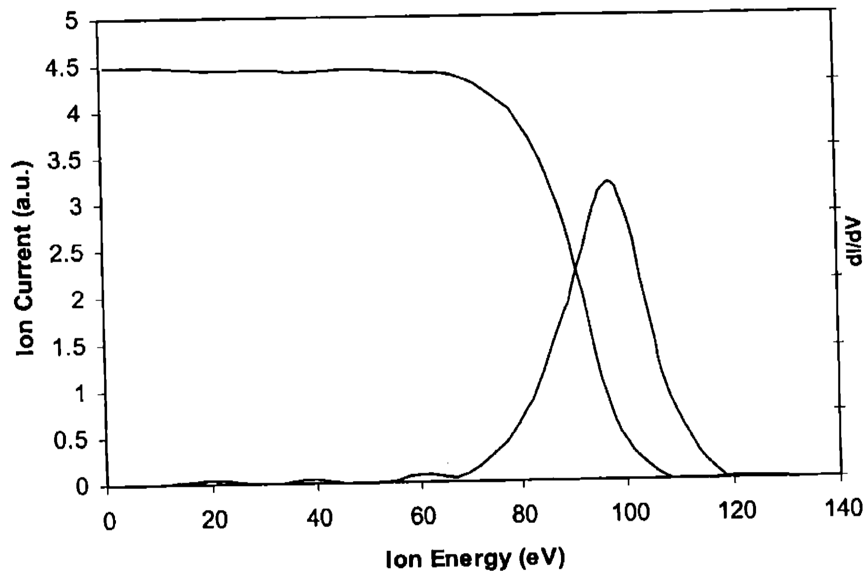

Figure 2-8: Characteristic ion energy distribution function measured by the gridded ion energy analyzer. The left axis represents the ion current and the right axis is the derivative of the ion current to ion energy and represents the energy distribution. The ion beam energy is the sum of the applied bias voltage, 70 eV, and plasma self-bias which is typically 20 – 30 eV. The full width at half maximum of the energy distribution is approximately 20 eV that is due to the ionization and potential variation within the plasma.

A typical current versus voltage measurement and its ion energy distribution function are shown in Figure 2-8. The ion current measured is on the order of microamps, and can be characterized by $j = \frac{I}{\pi r^2 t^n}$, where I is the collected ion current, r is the radius of the orifice, t is the transmission of the mesh, and n is the number of the mesh. The result resolution is on the order of ± 1eV, and the ion energy distribution is sharp and free of noise.

2.6. Mass spectrometer

Quadruple mass spectrometer (QMS, model: UTI 100C) was used for the ion and neutral composition analysis and can be installed in the mass spectrometer housing, which is mounted on the port facing the plasma beam source.[5] The mass spectrometer housing is evacuated by a differential turbo pump and maintained at 10^{-7} Torr.

Mass spectrometer consists of three major components of ionizer, mass filter, and detector. Gas molecules extracted from plasma by differential pumping are bombarded by electrons from the filaments within the ionizer and become positively charged ions that are then injected into the filter section. Energy of -50.0 eV is applied to electrons in this work and filament current was maintained to about 1.9 mA. A combined radio-frequency and electrostatic field is formed by two pairs of metal rods in the filter section. A charged substance with a specific mass-to-charge ratio has a dynamically stable trajectory within the field formed by the voltages on the rods. All other substances are filtered out. By continuously varying the applied voltage, a range of substances can be sequentially stabilized, and these traverse the length of the filter assembly. The species traversing the filter are detected by an electron multiplier that amplifies the single charge of the ion into a current. The output current of the multiplier is referenced against the scan voltage, thereby producing a spectrum of peaks. The spectrum produced shows ion current as a function of the quotient mass/charge in a series of peaks corresponding to different ions. The amplitude represents the quantity of each type of ion. Discrete peaks occur because the charged substances have discrete masses and discrete charges. Generally the term mass spectrum refers to a spectrum produced by positive ions.

To measure the ion spectral of the plasma beam, the filament has to be turned off and the ionizer grids grouned. Therefore, neutrals from the plasma beam would not convert to ions upon collisions with energetic electrons and interfere the measurement. Figure 2-9 shows the ion spectral of Ar plasma beam with the plasma off and on, respectively. Clearly, the mass spectrometer has a high sensitivity of picking up the signal.

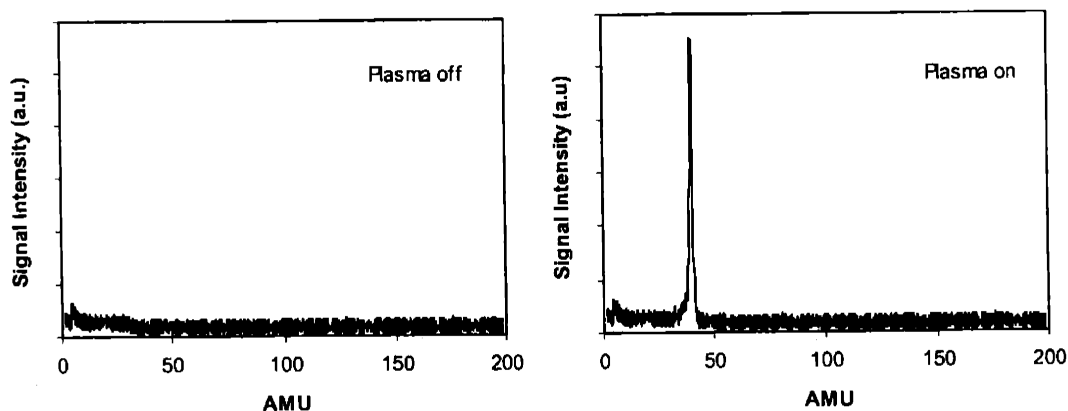

Figure 2-9: Argon ion beam characterization measured by a mass spectrometer. The mass spectrometer shows a high sensitivity of picking up the signal.

2.7. X-ray photoelectron spectroscopy

A surface analysis chamber is available for XPS analysis of the sample surface after etching in the plasma beam chamber. A schematic diagram of the analytical chamber is shown in Figure 2-10. It illustrates the setup of the X-ray gun, electron energy analyzer, and the sample rotation mechanism that facilitates the angular-resolved XPS (AR-XPS) analysis. A non-monochromatic Al X-ray source and a VG 100AX electron energy analyzer were used to measure the photoelectrons emitted from the sample surface. The pass energy was typically set at 50 eV.

The angle between the X-ray gun and the electron energy analyzer is fixed at ~67°, while the angle between the sample and the analyzer can be adjusted by tilting the sample around its supporting arm. The take-off angle is defined as the angle between the electron analyzer and the sample surface. Since the escape depth of photoelectrons is constant, the effective sampling depth, z, is a function of the take-off angle; i.e. $z = \lambda^{*}\sin\theta$. The electron energy analyzer probes deeper into the surface as the take-off angle increases and the

sensitivity of surface species is enhanced relative to the bulk materials as the take-off angle decreases.

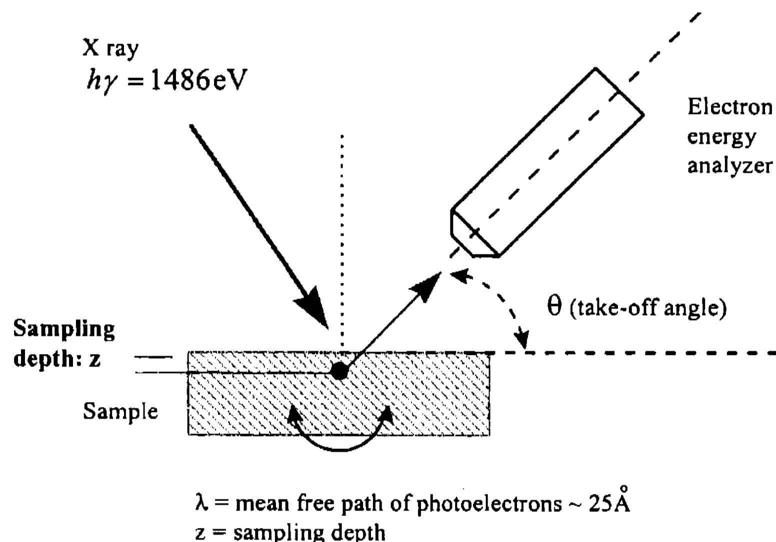

Figure 2-10: Schematic diagram of the setup of the XPS system. An non-monochromatic X-ray source and a VG 100AX electron energy analyzer were used to measure the photoelectrons emitted from the sample surface. The angle between the X-ray gun and the electron energy analyzer is fixed at ~67°, while the take-off angle, angle between the sample and the analyzer, can be adjusted by rotating the sample around its supporting arm. The sensitivity of surface species is enhanced relative to the bulk materials as the take-off angle decreases.

2.8. References

1. J. P. Chang, Ph.D. thesis, Massachusetts Institute of Technology, 1999.

2. H. Chae, Ph.D. thesis, Massachusetts Institute of Technology, 2000.

3. J. A. Woollam Co., Inc., *Guide to using WVASE32*, 1996.

4. G. Gibson, Ph.D. thesis, Massachusetts Institute of Technology, 1995.

5. *UTI Model 100C Precision Mass Analyzer manual*, 1983.

Chapter 3. Beam Study of Poly-silicon Etching in Cl_2/HBr

In this chapter, neutral and ionic beams created by the realistic inductively coupled plasma are used to character the ion-enhanced Cl_2/HBr plasma etching of poly-silicon. The etching yield of poly-silicon is characterized as a function of ion energy, gas composition, neutral-to-ion flux ratio and ion incident angle. A simple kinetic model is used to incorporate the major etching dependencies. The parameters needed to describe the model are either measured experimentally or determined by fitting the model to the available kinetic data.

3.1. Ion-enhanced etching yields versus ion energy

As proposed by Gray *et. al.*, the silicon etching rate (ER) includes three parts: thermal etching by neutrals, physical sputtering by ions, and ion enhanced etching.[1]

$$ER = k_0 \Gamma \exp\left(\frac{-E_a}{kT}\right) + Y_P(1-\Theta)\Gamma_+ + Y_{IE}\Theta\Gamma_+ \tag{3-1}$$

where k_0 and E_a are rate parameters for spontaneous chemical etching, Γ is the neutral flux, Y_P is the physical sputtering yield, Θ is the halogenation fraction of the surface layer by neutrals, Γ_+ is the ion flux, and Y_{IE} is the ion enhanced etching yield at saturated halogenation. It is the goal of the present work to determine Y_{IE}.

It is well known that the spontaneous etching of undoped or p-doped poly-silicon with Ar, Cl_2, and HBr is negligible, but the etching yield is greatly enhanced by ion bombardment.[2,3] So the first term in Equation (3-1) can be dropped. In the present work, the low ion energies and high flux ratios provide halogenation fractions close to 100%, and thus physical sputtering by ions is less important and the calculation of Y_{IE} is simplified as

$$Y_{IE} = \frac{ER}{\Gamma_+} \tag{3-2}$$

Silicon etching yields in Ar plasmas as a function of ion energy, measured with QCM, are shown in Figure 3-1. The error bars shown, based on replicated measurements of all the data points, are 95% confidence intervals for the mean. The sputter yields from an Ar plasma

increase linearly with the square root of ion energy. This agrees with the universal etching yield energy dependence model proposed by Steinbruchel:[4]

$$Y_{IE} = A(\sqrt{E} - \sqrt{E_{th}}) \tag{3-3}$$

where A is a scaling factor and E_{th} is the threshold energy. The A factor and threshold energy from a best fit of Equation (3-3) to our data, along with precious results from literature, are given in Table 3-1. Our results compare very well with precious data, implicating that the ion fluxes and silicon etching rates measured with the plasma beam/QCM are reliable.

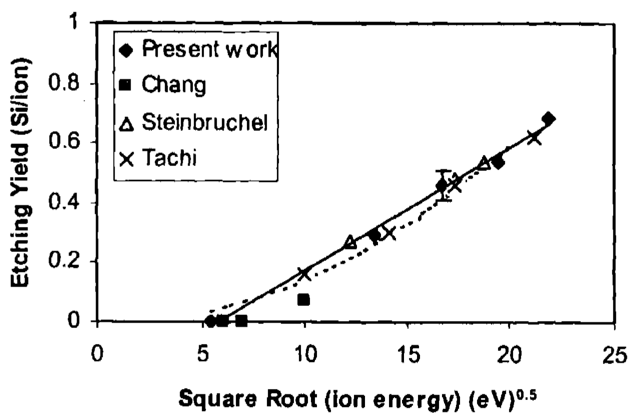

Figure 3-1. Etching yield of poly-silicon in Ar plasma as a function of incidence ion energy compared to literature data: Chang's data are from Ref. 5, Steinbruchel's data are from Ref. 4, and Tachi's data are from Ref. 6. The solid line is square root fit to our data, and the dashed line is first order fit.

Table 3-1. Parameters for silicon etching yields as a function of ion energy, where $Y_{IE} = A(\sqrt{E} - \sqrt{E_{th}})$.

Beam	Source	Ion energy range (eV)	A	E_{th} (eV)
Ar^+	Steinbruchel (Ref. 4)	100-1000	0.037	31
Ar^+	Present work	0-300	0.042	36
Cl^+/Cl	Chang (Ref. 5)	35-100	0.57	10
Cl_2^+/Cl_2	Balooch (Ref. 7)	40-900	0.23	25
Cl_2 plasma	Vitale (Ref. 8)	50-400	0.275	9
Cl_2 plasma	Present work	50-400	0.353	12
HBr plasma	Vitale (Ref. 8)	50-400	0.351	10
HBr plasma	Present work	50-400	0.299	10

To measure the ion-enhanced etching yield for reactive ions, we need to make sure that we are operating under the saturation regime. When the neutral-to-ion flux ratio is relatively low, the surface reaction can be limited by the neutral flux, therefore, the apparent etching yield calculated by dividing the etching rate by ion flux also depends on the neutral flux.[9] When the neutral-to-ion flux ratio is high, *i.e.* in the saturation regime, the surface is saturated with adsorbent reactive species, and the surface reaction is limited by the ion flux. Since the etching rate does not depend on the neutral flux, the apparent etching yield is constant and close to the true Y_{IE}.

Under typical operating conditions (1-5 mTorr, 2 sccm total flow, 300 W power), the neutral-to-ion flux ratio at the main chamber is greater than 300, which is in the surface saturation regime.[8] For all the work described here, the etching yields reported are believed to be in the surface saturation regime in which the etching rate exhibits little dependence on the neutral flux. The ion flux to the main chamber is measured directly with an ion flux detector. The total neutral flux to the main chamber, Γ_{total}, is equal to the line-of-sight beam flux from the plasma Γ_{los}, plus the background flux from the main chamber Γ_{bg}. The background flux is estimated by its thermal kinetic flux:

$$\Gamma_{bg} = \frac{P}{\sqrt{2\pi m_{eff} k T_g}} \tag{3-4}$$

where P is the pressure in the main chamber, m_{eff} is an effective average neutral mass, and T_g is the gas temperature in the main chamber (300K). To obtain the line-of-sight beam flux to the sample, it is necessary to correct the flux for the neutral beam spreading between the orifice and the sample:[10]

$$T_{los} = \alpha \left(\frac{R}{R+L} \right)^2 \Gamma_{plasma} \tag{3-5}$$

where α is the neutral flux at the extraction grid estimated simply by the gas flow rate, R is the radius of the extraction orifice (0.25 inch) and L is the distance to the sample (1-4 inch). The error in the neutral flux may be as much as a factor of 2, though the ion flux measurement is believed to be accurate to within 20%.

To further make sure that we are operating under saturation regime, we can change the neutral-to-ion flux ratio and measure the dependence of etching yield on the neutral-to-

ion flux ratio. By changing the distance between beam source and sample, the neutral-to-ion flux ratio can be adjusted. The normalized ion flux for Cl_2 plasma is shown in Figure 3-2 as a function of distance from beam source. The ion flux decreases almost linearly as distance L due to beam broadening. The neutral flux, estimated from Equation (3-4) and (3-5), also decreases as distance L, as shown in Figure 3-2. The neutral flux drops much sharply with distance, resulting in the neutral to ion flux also drops with distance.

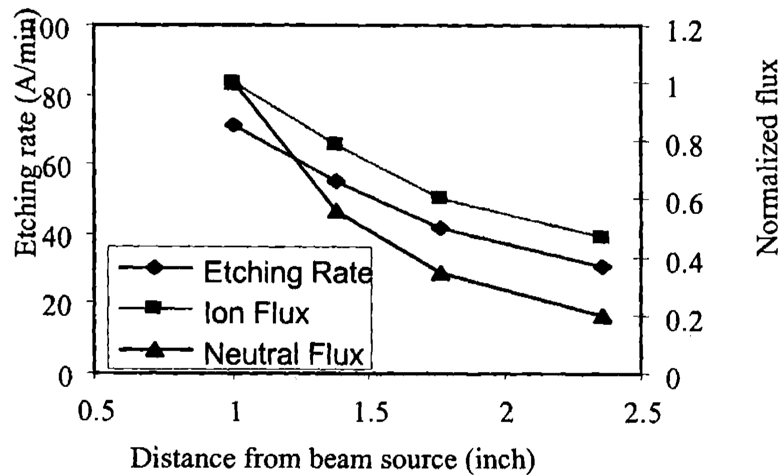

Figure 3-2: The ion/neutral flux and etching rate as a function of distance from beam source. The ion flux decreases almost linearly as distance L due to beam broadening. The neutral flux also decreases as distance L. The neutral flux drops much sharply with distance, resulting in the neutral to ion flux also drops with distance. The etching rate also decreases with distance due to the decreased ion flux.

The etching rate also decreases with distance due to the decreased ion flux, as shown in Figure 3-2. But the etching yield should not differ much if the etching process is in the neutral saturation regime, as in a real commercial etcher under certain processing conditions. The plot of etching yield as a function of the neutral-to-ion flux ratio is shown in Figure 3-3. The relatively flat curve is a confirmation that the etching process under our experimental conditions is in the neutral saturation regime.

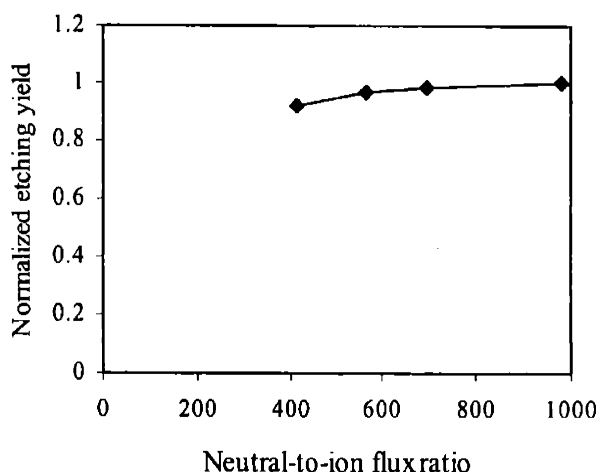

Figure 3-3: The etching yield as a function of the neutral-to-ion flux ratio. The relatively flat curve indicates that we are operating under the neutral saturation regime.

Silicon etching yields with Cl_2 plasma beam are shown in Figure 3-4, along with etching yield using Cl^+ and Cl beams, and Cl_2^+ and Cl_2 beams.[7] In the present work, the plasma beam contains a mixture of Cl^+ and Cl_2^+ ions and neutrals. Both Cl^+ and Cl_2^+ have been reported as important ionic species contributing to etching in a high density chlorine plasma reactor. In a realistic plasma beam, both Cl^+ and Cl_2^+ exist, as demonstrated by mass spectrometer measurement in Section 3.5. Therefore, the plasma beam data lie between the Cl^+/Cl and Cl_2^+/Cl_2 data, as would be expected. The threshold energy for ion enhanced etching is about 12 eV, significantly lower than the threshold energy for ion sputtering with Ar, 30 eV. Since reactive ions in the presence of reactive neutrals lead to the formation of volatile products, the average surface binding energy is reduced and so is the threshold energy.

Silicon etching yields with HBr plasma beams are shown in Figure 3-5. The threshold energy for ion enhanced etching in HBr is approximately 10 eV, which is similar to that for Cl_2 plasmas. Vitale observed that the etching yields in HBr plasmas are significantly higher than those in Br_2 plasmas and the threshold energy is lower than that in Br_2 plasmas, 44 eV.[8] These are probably due to the hydrogen content of the plasma enhancing the silicon etching in the presence of ion bombardment.

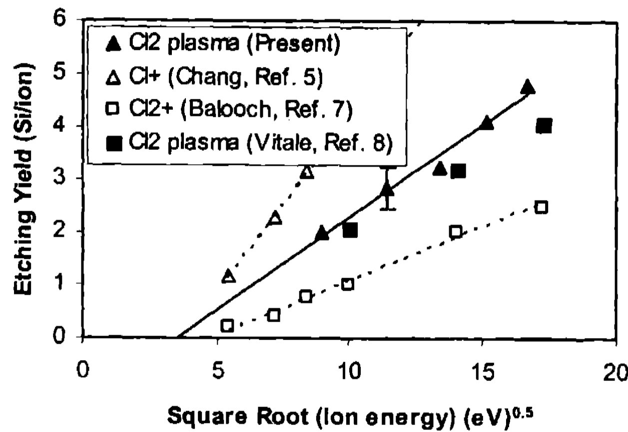

Figure 3-4: Etching yield of poly-silicon in chlorine plasma beam (solid triangles) compared to literature data: Cl^+/Cl data are from Ref. 5, Cl_2^+/Cl_2 data are from Ref. 7, and Cl_2 plasma data are from Ref. 8. In a realistic plasma beam, both Cl^+ and Cl_2^+ exist. Therefore, the plasma beam data lie between the Cl^+/Cl and Cl_2^+/Cl_2 data.

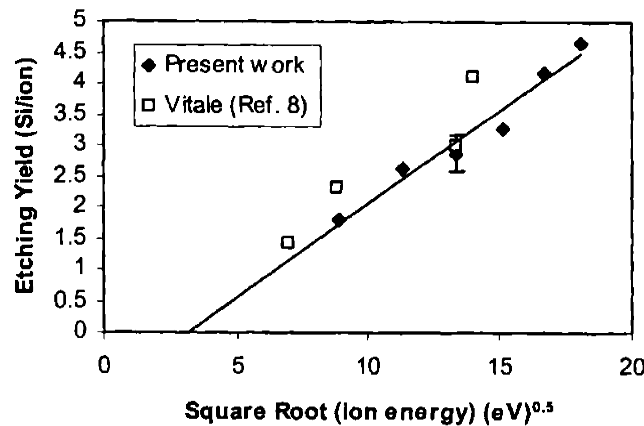

Figure 3-5: Etching yield of poly-silicon in HBr plasma beam. Vitale's data are from Ref. 8. The threshold energy for ion enhanced etching in HBr is approximately 10 eV, similar to that for Cl_2 plasmas, and lower than that for Br_2 plasmas.

3.2. Ion enhanced etching yields versus neutral-to-ion flux ratio

For ion enhanced chemical etching, the etching yield is typically a strong function of neutral-to-ion flux ratio. But as shown in Section 3.1, we are operating in the saturation regime under typical conditions. Although we can change the neutral-to-ion flux ratio to some extent by changing the distance between the plasma source and the sample, the neutral-

to-ion flux ratio is always above 100, therefore the etching yield is not very sensitive to the change of neutral-to-ion flux ratio.

To further lower the neutral-to-ion flux ratio such that we can operate in neutral flux limited regime, we introduce argon into the feed gas. Since the reactive gas is diluted by argon, but the ion flux is relative constant, the neutral-to-ion flux can be further decreased below 100. The etching yields versus neutral-to-ion flux ratio for poly-silicon etching by Cl_2 and HBr plasma beam are shown in Figure 3-6. We can clearly identify the neutral flux limited regime and saturation regime.

With the phenomenological model proposed by Chang, we can derive the sticking coefficient of reactive neutrals.[11] For the completeness of this thesis, we briefly review the model below.

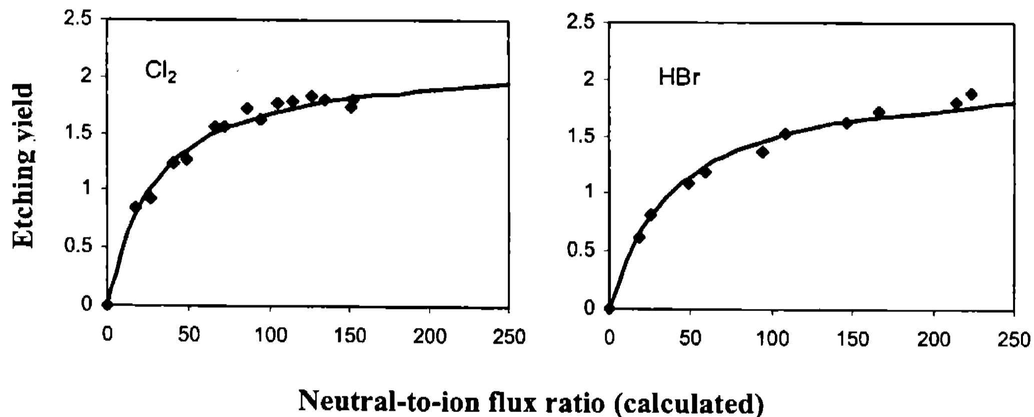

Figure 3-6: The etching yield versus neutral-to-ion flux ratio of poly-silicon etching by 100 eV Cl_2 and HBr plasma beam, respectively. The solid diamonds are experimental results, and the lines are model predictions.

Physisorption, chemisorption, desorption and ion induced desorption of chlorine or bromine atoms are reduced into an overall adsorption reaction, with an assigned surface halogenation coefficient (or sticking coefficient), s. The major product is assumed to be SiX_4, and X represent Cl or Br. The reactions considered in the model is summarized in Table 3-2. The sorption probability of ions with normal incident angle is assumed to be 1.

Table 3-2. The simplified phenomenological surface kinetics model for ion-enhanced poly-silicon etching with Cl_2 or HBr plasma beam.

Simplified kinetics model	Mechanism
$X_{(g)} + * \xrightarrow{s} X_{(s)}$	Sorption of atomic halogen
$X^+_{(g)} + * \longrightarrow X_{(s)}$	Sorption of ionic halogen
$Si_{(s)} + 4X_{(s)} \xrightarrow{\beta X^+} SiX_{4(g)} + 4*$	Ion-enhanced etching

The ion enhanced etching rate is assumed to be proportional to the product of surface halogenation and the ion flux:

$$ER = \beta\theta I^+ \tag{3-6}$$

Therefore, the ion enhanced etching yield, *Y*, can be expressed in the following form:

$$Y = \beta\theta \tag{3-7}$$

The parameter β represents the etching yield when the surface is saturated and θ represents the extent of surface halogentation, which can be expressed in the following form by performing a site balance:

$$\theta = \frac{sR+1}{sR+1+4\beta} \tag{3-8}$$

The parameter R is the neutral-to-ion flux ratio, calculated as explained in Section 3.1. Substituting θ in Equation (3-7) and rearranging the equation yields the following equations:

$$\frac{1}{Y} = \frac{1}{\beta} + \frac{4}{sR+1} \tag{3-9}$$

At higher flux ratios where $sR >> 1$, Equation (3-9) can be approximated as:

$$\frac{1}{Y} = \frac{1}{\beta} + \frac{4}{s} \cdot \frac{1}{R} \tag{3-10}$$

Therefore, we can calculate β and s from the intercept and slope by a linear regression of $\frac{1}{Y}$ versus $\frac{1}{R}$. The model predictions to the experimental data are shown as lines in Figure 3-6. The fitted β are 2.2 and 2.1 for Cl_2 and HBr plasma beam, respectively. And the fitted s are 0.28 and 0.2 for Cl_2 and HBr plasma beam, respectively. Since the ions in the Cl_2 plasma beam are mixture of Ar^+, Cl^+, Cl_2^+, and the neutrals are mixture of Cl, Cl_2, the fitted value should be weighted average of the values for each pure species. Table 3-3 shows the fitted values for some pure species by Chang, *et. al.* Considering our calculated neutral-

to-flux ratio can have an error rate of a factor of two, our results are quite close to theirs. It is worth noting that the sticking coefficient s for HBr system is lower than Cl_2 system, probably due to the relative larger size of bromine atom or relatively lower chemical reactivity.

Table 3-3. Model parameters for ion enhanced etching of poly-silicon by different neutral and ion systems at 100 eV ion energy.

System	β	s
Cl^+, Cl (Ref. 5)	3.61	0.45
Ar^+, Cl (Ref. 11)	3.59	0.30
Ar^+, Cl_2 (Ref. 11)	0.07	0.83

3.3. Ion-enhanced etching yields versus gas composition

To achieve more anisotropic etching and higher selectivity and maintain fast etching rate at the same time, a mixture of Cl_2 and HBr gases is widely used in commercial poly-silicon etching recipes. So it is necessary to develop an understanding of the chemistry in these systems.

The ion fluxes in Cl_2+HBr plasmas are shown in Figure 3-7. The ion flux decreases by more than 40% from a pure Cl_2 plasma to a pure HBr plasma. The decrease in the flux is probably due to a decrease in the ion density, as suggested by Vitale.[8]

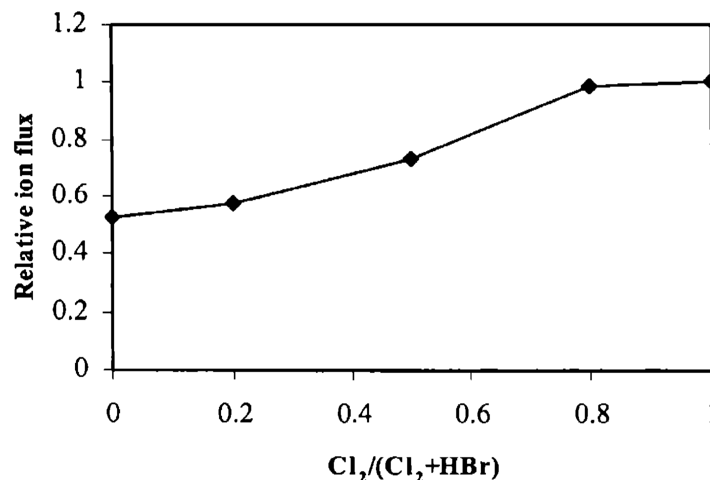

Figure 3-7: Ion flux as a function of feed gas composition. The ion flux decreases by more than 40% from a pure Cl_2 plasma to a pure HBr plasma.

Etching yields in mixed Cl_2+HBr plasma at two ion energy levels are shown in Figure 3-8. The etching yield in pure Cl_2 is slightly higher than HBr, with a maximum near 50% HBr, probably due to synergistic effect between Cl_2 and HBr. Vitale observed that similar trend of etching yield of silicon in dependence of gas composition in their experiments, except that their etching yield in pure HBr plasma is slightly higher than in pure Cl_2 plasma.[8] This could be because the ion and neutral composition in their plasma is different from ours. It has been observed that the HBr plasmas have lower ion flux than Cl_2 plasmas in our system, which might result in a lower poly-silicon etching rate, typical in commercial etchers.[12,13] Cheng *et. al.* observed that the Cl coverage after etching in a pure Cl_2 plasma is 1.6 times higher than the Br coverage measured after etching in a pure HBr plasma, and they proposed that the HBr plasma etches Si more slowly than do Cl_2 plasmas mainly because less halogen is present on the surface at saturated coverage and the ion enhanced rate of formation of volatile products such as $SiBr_2$ is lower.[14,15] As explained in Section 4.2.2, this is unlikely the reason.

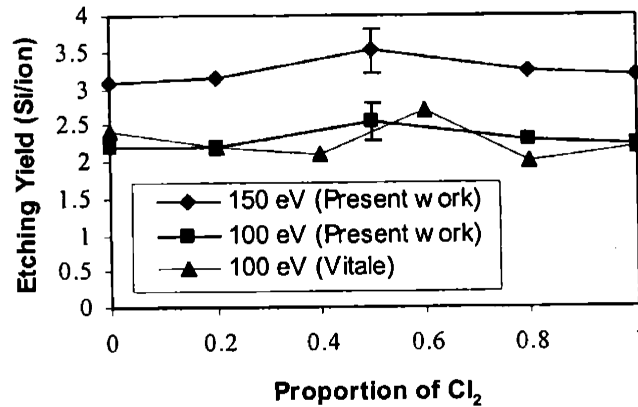

Figure 3-8: Etching yield of poly-silicon as a function of Cl_2 in Cl_2+HBr at different ion energies. Vitale's data are from Ref. 12. Pure Cl_2 and pure HBr plasmas have similar etching yields.

3.4. Angular dependence of ion-enhanced etching yields

In a real plasma etcher, the ions are not perfectly directional. The ion off-normal angle can be approximated with a Gaussian distribution with certain standard deviation or full-width at half-maximum (FWHM). The FWHM of ion angular distribution can be controlled by plasma conditions, including pressure, plasma density, bias power, etc.

Due to the ion angular distribution, the ions can strike the feature surface with different incident angle. The feature sidewall can be bombarded by off-normal ions at grazing angle. Ions scattered from one surface can strike the other surface at arbitrary angle. To account for the effect of ions striking surface at different incident angle, the angular dependence of etching yield is characterized.

3.4.1. Angular dependent etching yield measurement

To account for the ion flux varying with the ion incident angle, the etching yield (EY) is calculated as in Equation (3-11)[16]

$$EY(\theta) = \frac{ER(\theta)}{\Gamma_i \cos\theta} \tag{3-11}$$

where Γ_i is the ion flux in the direction normal to the extraction grid and θ is the ion incident angle with respect to the normal of the sample surface. In reality, since our sample holder is not perfectly aligned with the plasma beam source, the distance between the sample and the plasma beam source changes when we rotate the sample holder to change the ion incident angle. In this case, the ion flux seen by the sample should not be simply discounted with $\cos\theta$. Instead we measure the ion fluxes at different ion incident angles directly. We can see slight deviation of ion fluxes measured at different ion incident angles from those discounted with $\cos\theta$. This slight deviation is especially important at large off-normal angle when the etching rate is relatively small.

The silicon etching yields as a function of ion impingement angle depends on the mechanism of etching. For Ar^+ ion sputtering, the angular dependence follows the typical physical sputtering yield curve, with a maximum near 50° corresponding to the angle for maximum momentum transfer.[8] With reactive gases, the ion enhanced chemical etching does not show the same behavior as a function of angle.[5,16-18] The etching yield is constant or slowly decreases from normally incident angle (0°) to 50°-60° off-normal. The etching yield then falls off rapidly above 60° off-normal. As suggested by Chang, a possible reaction mechanism attributing to the observed angular dependence is that reactive atoms are implanted into the substrate more readily with normally incident ions.[5] The normally incident ions consequently create mixing of the absorbed incident ions into the lattice whereby

enhancing the etching yield. Therefore, the chemical reactivity of chlorine atoms, together with the ion induced chlorination, may compensate for the less efficient momentum transfer to the surface atoms at near normal incident angle. In addition, the processes leading to the product formation by chemical sputtering are associated with the number of bonds breaking within the surface layers, rather than momentum transfer to the surface atoms that is needed for physical sputtering. The number of bonds broken by the ion impingement within the surface layers is not expected to vary significantly except at large off-normal angles where ion scattering occurs without losing much energy to the surface.

The angular dependence of poly-silicon etching yield with pure Cl_2 and HBr is shown in Figure 3-9. Both of them show a similar trend for reactive ion etching, although there is significant difference between them. For pure Cl_2, the etching yield almost remains constant until the off-normal ion incident angle is increased to 45°, while for HBr, the etching yield starts dropping even with small off-normal angle.[19] Mayer and Chang measured the angular dependence of etching yield with Cl_2 and Vitale measured that with HBr using different apparatus, and our experimental measurements agree well with their results.[5,8,16]

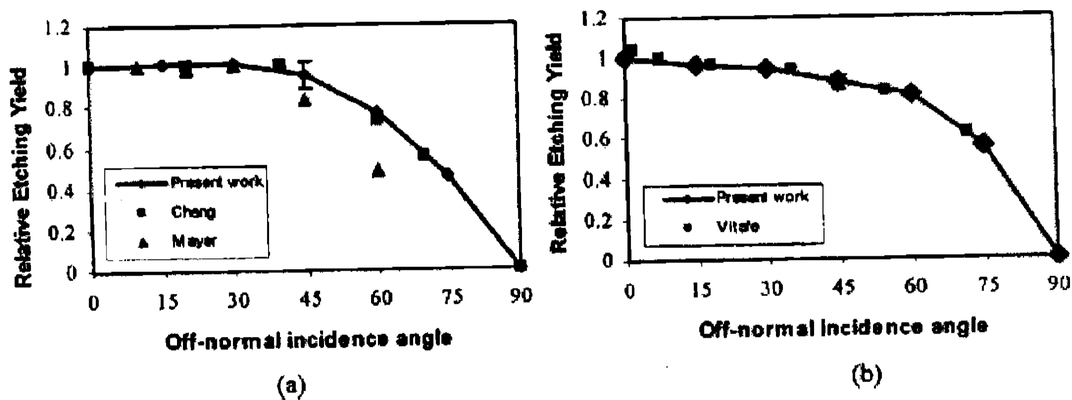

Figure 3-9: Etching yield of poly-silicon as a function of ion impingement angle. Ion energy=150 eV, and saturated surface coverage. (a) In Cl_2 plasma, Chang's data from Ref. 9 and Mayer's data from Ref. 10 and (b) in HBr plasma, Vitale's data from Ref. 8.

For the mixture of Cl_2 and HBr of different composition, the angular dependence of etching yield shows a similar trend to pure HBr, as shown in Figure 3-10. It was well known that the shape of angular dependence curve is highly related to the process of ion enhanced bond breaking, volatile product formation, and product desorption. Therefore, the similarity

of angular dependence of etching yield curve between pure HBr and the Cl_2+HBr mixture might be due to the existence of the Br atom.

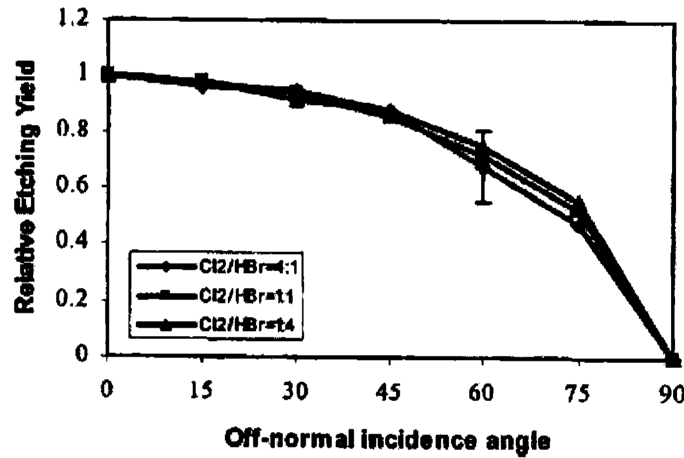

Figure 3-10: Etching yield of poly-silicon as a function of ion impingement angle in Cl_2+HBr plasma. Ion energy=150 eV, and saturated surface coverage.

3.4.2. Effect of angular dependent etching yield on profile evolution

To investigate the effect of the angular dependent etching yield on feature profile evolution, we used a 2- $\frac{1}{2}$ dimensional Monte Carlo technique associated with surface kinetics and cell removal algorithm to simulate the profile evolution. The detail about the simulation will be explained in Chapter 6.

Profile evolution of SiO_2 masked trench etching is simulated with the Monte Carlo method for different functionalities to investigate the influence of angular dependent etching yield on the profile evolution. The mask is 0.35 μm wide and 0.5 μm high, and the spacing is 0.35 μm wide. To simplify, an infinite selectivity is assumed, *i.e.*, no etching occurs on the SiO_2 mask. The ion energy is 100 eV and all the ions are assumed to have a Gaussian angular distribution with full-width at half-maximum (FWHM) of 5°, which are typical of a commercial high density plasma etcher.

To start with, profile evolutions for $\alpha = 1$ and $\alpha = 0.9$ are shown in Figure 3-11. For $\alpha = 1$, all the ions striking a surface cell would be adsorbed and result in subsequent etching. But for $\alpha = 0.9$, an incident ion has a 90% chance to stick onto the surface cell and a 10%

chance to be scattered back into the gas phase. The difference in the ion adsorption behavior contributes to the difference in the profile evolutions. If each incident ion sticks onto the surface cell and results in etching, the local etching rate would be completely dependent on the ion flux onto the cell. Due to the ion shadowing by the mask, the ion flux is at the maximum around the center of the bottom surface. Therefore, the etching rate increases gradually from the corner of the bottom surface to the center. As the etching process continues, this effect was aggravated and an obvious bowed bottom can be observed. At the same time, a bowed sidewall is also captured by the simulation due to the off-normal ions striking the sidewall. The sidewall etching may be greater than actually observed, since the off-normal ions striking the sidewall at grazing angle tend to be scattered instead of etching the surface, while in the simulation they have the same etching yield as ions striking the surface at a normal angle, resulting in an exaggerated etching on the sidewall. For $\alpha = 0.9$, every ion has a 10% chance to be scattered from the surface cell, and the ion flux in the feature is different from that if $\alpha = 1$, since the scattering would result in the redistribution of ions onto the feature surfaces. As suggested by Figure 3-11, the ion scattering tends to square the feature bottom.

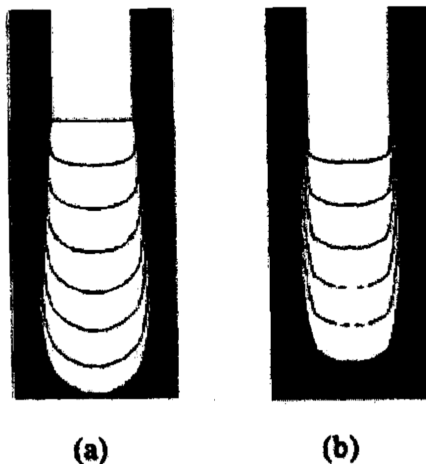

Figure 3-11: Feature profile evolution by Monte Carlo simulation, assuming 100 eV ion energy, neutral-to-ion flux ratio=20:1, and ion angular distribution with FWHM of 5°: (a) $\alpha = 1$ and (b) $\alpha = 0.9$.

For a more realistic plasma etching process, the scattering probability of an ion often depends on, among other factors, surface composition and the incident angle. For example, the etching yield of poly-silicon in a Cl^{+} ion beam is constant from normally incident ions (0°)

to 45° off-normal and then falls off rapidly to 0 at 90° off-normal. For HBr ion beam etching, the etching yield starts dropping slowly from a normal incident angle (0°) to 50°-60° off-normal. The etching yield then falls off rapidly above 60° off normal. As will be shown, the difference of the angular dependence of scattering probability between Cl_2 and HBr has a significant influence on the profile evolution.

To illustrate their effect on the profile evolutions, simulation results with various angular dependence of etching yields are shown in Figure 3-12(a), and corresponding angular dependences of the etching yield are shown in Figure 3-12(b). As the incident angle is between 0° and 45°, $EY_{Si}(\theta)$ decreases most rapidly in case 1, and decreases most slowly in case 3; above 45°, there is not much difference among these three cases, and as the incident angle reaches θ=90°, all of $EY_{Si}(\theta)$ fall down to zero. We assume that the drop of etching yield below 45° off-normal is due to low-angle scattering, while the drop over 60° off normal can be attributed to high-angle scattering. It was well known that high-angle scattering, *i.e.*, the scattering of ions from the sidewall, focuses the ions around the foot of the sidewall and induces microtrenching, but the role of low-angle scattering on profile evolution has not be addressed before.

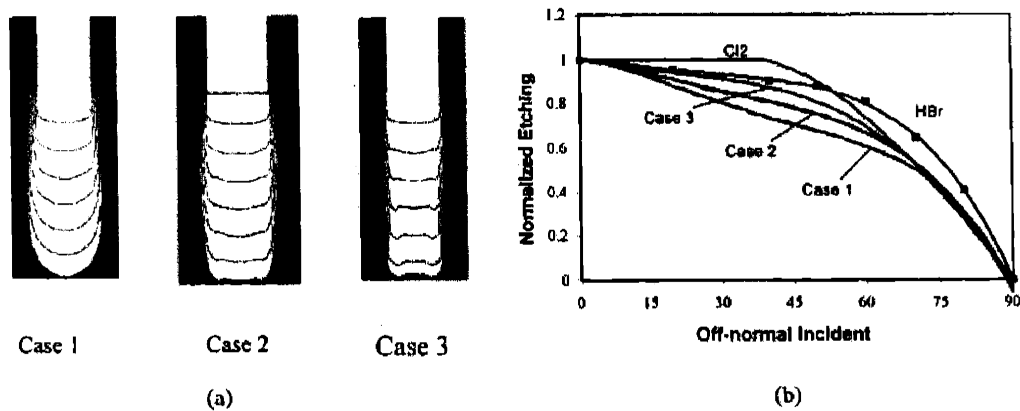

Figure 3-12: Feature profile evolution by Monte Carlo simulation, assuming 100 eV ion energy, neutral-to-ion flux ratio=20:1, and ion angular distribution with FWHM of 5°: (a) simulated profiles and (b) corresponding angular dependence of etching yield.

As can be seen in Figure 3-12, the simulated etching profiles are strongly influence by the angular dependence of $EY_{Si}(\theta)$. In case 1, we see significant sidewall broadening and bottom downward bowing, as compared to case 2 and 3, due to the low-angle scattering. The ions striking the bowed bottom surface are reflected onto the neighboring sidewall and result

in sidewall broadening. In the simulation, we did not take into account the fact that the silicon oxide sputtered from the mask by energetic ions may deposit onto the sidewall and thus prevent or reduce the undercutting below the mask. In addition, an infinite etching selectivity over the oxide mask is assumed. As a result, all the ions striking the mask are scattered into the feature, which to some extent may exaggerate the sidewall etching. Therefore, the pronounced undercutting in case 1 might be the artifact of the lack of deposition mechanism and simplified assumption in the simulation. But qualitatively, the trend that there is less and less lateral etching on sidewall from case 1 to case 3 is correct. The scattering of ions from the bowed bottom surface contributes to the slower etching rate around the corner of the bottom surface, aggravating the bowing of the bottom. While the low-angle scattering tends to create downward bowing of the bottom surface, the high-angle scattering from the sidewall tends to increase the etching rate around the corner of the bottom surface and create an upward bowed bottom. A combination of these two might be able to keep the sidewall straight and limit the microtrenching that resulted from the focusing of ions by a tapered sidewall, as shown in Figure 3-12 for case 2 and 3. It should also be noted that around the center of bottom surface, there is a transition from slightly downward bowing in case 2 to slightly upward bowing in case 3 and slight microtrenching can still be observed in both case 2 and 3.

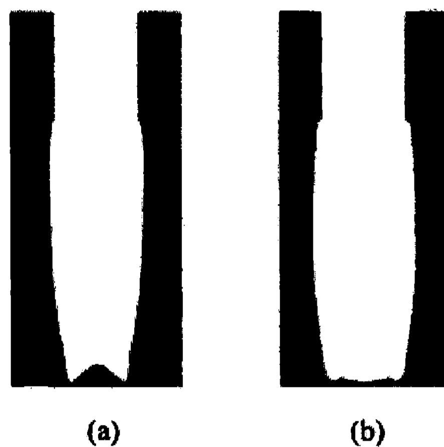

Figure 3-13: Feature profile evolution by simulation, assuming 100 eV ion energy, neutral-to-ion flux ratio=20:1, and ion angular distribution with FWHM of 5°: (a) etching in Cl_2 plasma and (b) etching in HBr plasma.

Compared with these cases, pure HBr has similar angular dependence of etching yield as case 3, indicating a similar relative amount of low-angle and high-angle scattering. However, for Cl_2, there is no low-angle scattering at all. Therefore, as the general trend

suggests, we would expect the profile evolution for pure HBr similar to case 3, but more significant microtrenching and tapered sidewall in the simulated feature for Cl_2 plasma etching. Figure 3-13 shows the profile evolution simulated for Cl_2 and HBr etching, which confirms our expectation and is also in agreement with a typical observed profile in commercial etcher with Cl_2 and HBr recipes, as shown in Figure 3-14.[20] So this result is further confirmation that the measured Cl_2 and HBr angular dependence of etching yield is correct and the profile evolution simulation captures the features in a real etching process.

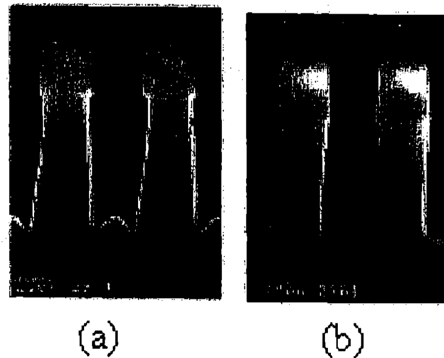

Figure 3-14: Cross sections of nominally 0.35 μm nested trenches etched with 250 W source power, 150 W bias power, 10 mTorr chamber pressure, 80 sccm flow rate in: (a) Cl_2; (b) HBr.

3.5. Mass spectrometer measurement of beam composition

To further understand the etching kinetics, it is necessary to know what species are coming from the plasma to the wafer. The ion flux in Cl_2+HBr plasmas can be characterized by mass spectrometer.

The UTI Precision mass spectrometer is capable of making both qualitative identification and quantitative measurements of gases in a vacuum system.[21] To accurately measure the concentration of each species, peak intensities for ionization efficiency (a combination of ionization cross-section and ionization potential), multiplier gain, and quadrupole transmission for each species have to be considered. Measurement after taking these factors into account generally yield calculated results which are within a factor of two of the truth.

Since we are only trying to measure the ion spectrum, the ionization efficiency doesn't need to be considered. The multiplier gain (G) under some conditions is considered to

be a function of the ion mass (AMU), and have an $m^{-1/2}$ dependence approximately. The transmission (T) of any ion through the quadrupole filter is dependent on the m/e or AMU approximately. The transmission of the standard UTI Model 100C can be considered nearly 100% from AMU 1-40, then falls off at approximately one decade per 150 AMU. The corrected total current is:

$$I^+ = \sum_j \frac{I^+_{j,m}}{G_j T_j} \tag{3-12}$$

where $I^+_{j,m}$ is the directly measured current for species j, which can be calculated by the integration of the peak. G_j and T_j are the multiplier gain and transmission efficiency for species j respectively.

The ion flux spectra for pure Cl_2 and HBr plasma beam is shown in Figure 3-15. The spectra in Figure 3-15 has not been corrected for the transmission or detection efficiency of the mass spectrometer. After the correction for the detection sensitivity and transmission efficiency, the ion species fluxes were calculated. For pure Cl_2 plasma, the vast majority of the ions are Cl_2^+ (53%), the remainder being Cl^+(47%). Note that the Cl^+ concentration in our system is much higher than Vitale's (30%).[8] This is probably because Vitale's chamber wall is stainless steel, which has a high Cl recombination coefficient compared to quartz crystal liner used in our plasma source. HBr plasmas consist of a mixture of Br^+, HBr^+ and Br_2^+. There is possibly H^+ or H_2^+ ion flux as well, but our mass spectrometer cannot detect them. Similar to Vitale, we also detected Br_2^+. The Br_2^+ is likely formed from electron impact ionization of Br_2 formed in the plasma, or by ion-neutral reactions, or some other pathways as well.

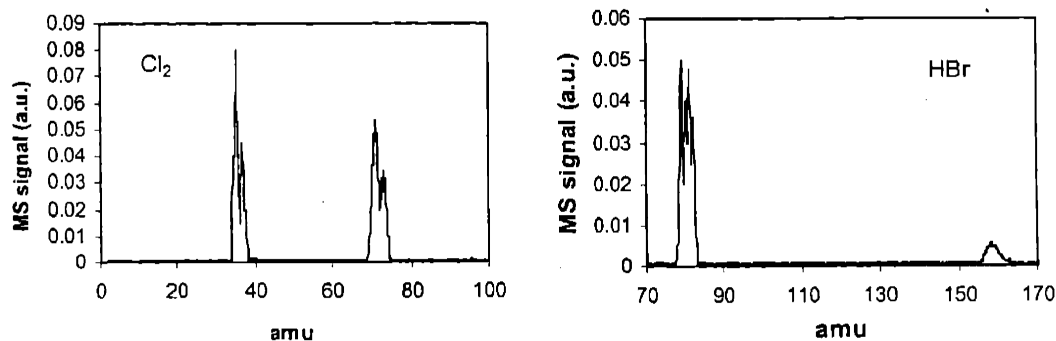

Figure 3-15: Mass spectra of ion flux from plasma beam source with pure Cl_2 and HBr plasmas. The signals have not been corrected for the detection or transmission efficiency of the mass spectrometer.

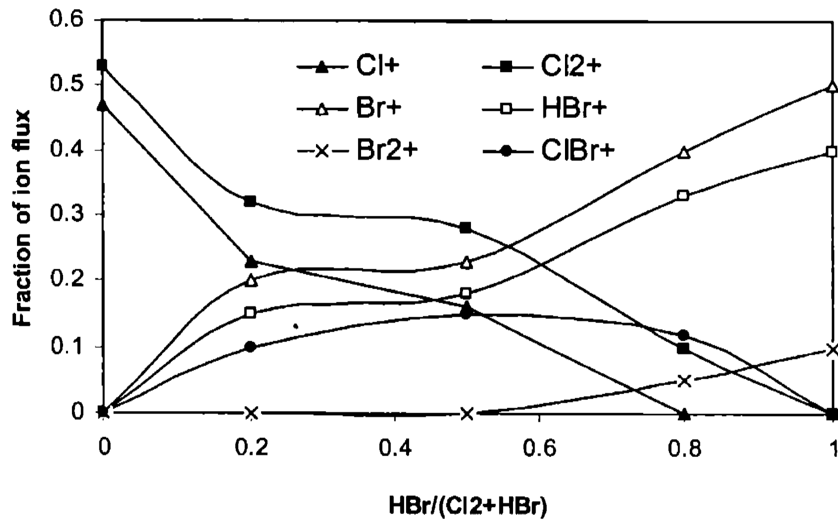

Figure 3-16: Ion flux composition of mixed Cl_2+HBr plasma measured by mass spectrometer.

For the mixed Cl_2+HBr plasma, the ion composition as a function of percent HBr is shown in Figure 3-16. In addition to Cl^+, Cl_2^+, Br^+, HBr^+, Br_2^+ observed in pure Cl_2 and HBr plasma, $ClBr^+$ also accounts for a significant amount.

3.6. Conclusions

The etching yield by the HBr plasma beam is slightly lower than the Cl_2 plasma beam, and a maximum etching yield at 50% HBr was observed. The angular dependence of etching yield by both Cl_2 and HBr strongly suggests the mechanism of ion enhanced chemical etching. With Cl_2 plasma beam, the etching yield almost keeps constant until the off-normal ion incident angle increased to 45°, while with the HBr plasma beam, the etching yield starts dropping even with small off-normal angle. The etching yield by Cl_2+HBr plasma at different composition exhibits a similar trend as pure HBr. The difference of angular dependent etching yield between Cl_2 and HBr might contribute to the difference of feature profile evolution in these two chemistries, *i.e.*, more anisotropic etching in HBr plasma, as suggested by Monte Carlo feature profile evolution simulation.

3.7. References

1. D. C. Gray, I. Tepermeister, and H. H. Sawin, *J. Vac. Sci. Technol. B* **11**, 1243 (1993).

2. M.-C. Chuang and J. W. Coburn, *J. Vac. Sci. Technol. A* **8**, 1969 (1990).

3. J. W. Coburn, *J. Vac. Sci. Technol. A* **12**, 617 (1994).

4. C. Steinbruchel, *Appl. Phys. Lett.* **55**, 1960 (1989).

5. J. P. Chang, A. P. Mahorowala, and H. H. Sawin, *J. Vac. Sci. Technol. A* **16**, 217 (1998).

6. S. Tachi, K. Miyake, and T. Tokuyama, *Jpn. J. Appl. Phys., Suppl.* **21**, 141 (1983).

7. M. Balooch, M. Moalem, W. E. Wang, and A. V. Hamza, *J. Vac. Sci. Technol. A* **14**, 229 (1996).

8. S. A. Vitale, H. Chae, and H. H. Sawin, *J. Vac. Sci. Technol. A* **19**, 2197 (2001).

9. R. A. Barker, T. M. Mayer, and W. C. Pearson, *J. Vac. Sci. Technol. B* **1**, 37 (1983).

10. J. W. Coburn and E. Kay, *J. Vac. Sci. Technol.* **8**, 738 (1971).

11. J. P. Chang, J. C. Arnold, G. C. Zau, H.-S. Shin, and H. H. Sawin, *J. Vac. Sci. Technol. A* **15**, 1853 (1997).

12. J.-H. Lee, G.-Y Yeom, J.-W. Lee, and J.-Y. Lee, *J. Vac. Sci. Technol. A* **15**, 573 (1997).

13. D. X. Ma, T.-A. Lin, and C.-H. Chen, *J. Vac. Sci. Technol. A* **10**, 1217 (1992).

14. C. C. Cheng, K. V. Guinn, V. M. Donnelly, and I. P. Herman, *J. Vac. Sci. Technol. A* **12**, 2630 (1994).

15. C. C. Cheng, K. V. Guinn, I. P. Herman, and V. M. Donnelly, *J. Vac. Sci. Technol. A* **13**, 1970 (1995).

16. T. M. Mayer, R. A. Barker, and L. J. Whitman, *J. Vac. Sci. Technol.* **18**, 349 (1981).

17. H. Okano and Y. Horiike, *Jpn. J. Appl. Phys.* **20**, 2429 (1981).

18. B.-O. Cho, S.-W. Hwang, G.-R. Lee, and S. H. Moon, *J. Vac. Sci. Technol. A* **18**, 2791 (2000).

19. J. A. Levinson, E. S. G. Shaqfeh, M. Balooch, and A. V. Hamza, *J. Vac. Sci. Technol. A* **15**, 1902 (1997).

20. J. M. Lane, F. P. Klemens, K. H. A. Bogart, M. V. Malyshev, and J. T. C. Lee, *J. Vac. Sci. Technol. A* **18**, 188 (2000).

21. UTI Model 100C Precision Mass Analyzer manual (1983).

Chapter 4. XPS analysis of surface

In this chapter, X-ray photoelectron spectroscopy (XPS) of poly-silicon surface before and after etching is taken to facilitate the understanding of surface reaction. The amount of halogen on the surface after etching was quantified by integrating the area of Cl (*2p*) or Br (*3d*) peak. Angle resolved measurement was applied to extract the depth profile.

4.1. XPS analysis of poly-silicon surface before etching

A survey spectrum of the photoemission of the poly-silicon surface before etching is shown in Figure 4-1. Oxygen, fluorine and carbon are detected at significant levels. The oxygen emission mainly comes from a native oxide layer (silicon oxide formed due to exposure to air). The carbon and fluorine emission might come from surface contamination. The silicon emission intensity is attenuated due to the presence of the native oxide layer. The removal of the native oxide layer is performed by stripping the poly-silicon sample in aqueous hydrofluoric acid for 1 minute, rinsing with de-ionized water, and then drying in N_2 gas.[1]

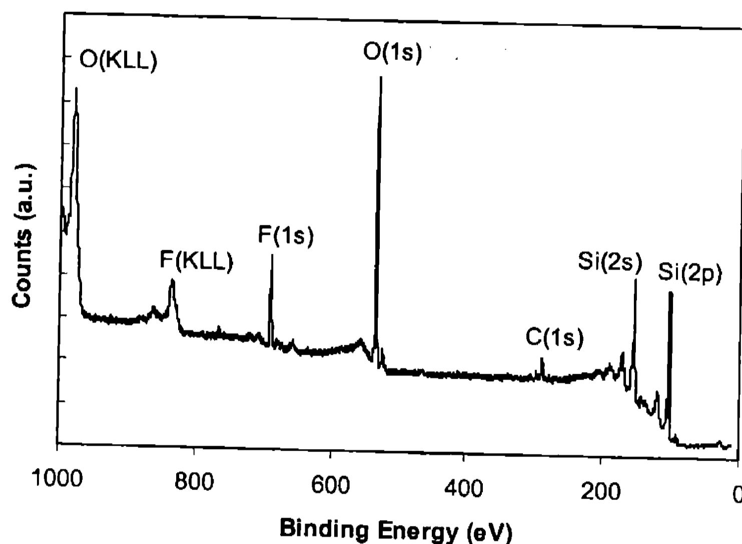

Figure 4-1: A survey spectrum of photoemission of the poly-silicon surface before etching. Native oxide and an appreciable amount of carbon and fluorine contamination are observed. The take-off angle is at 30°.

4.2. XPS analysis of poly-silicon surface after etching

Both the low resolution and high resolution spectrum of photoemission of the poly-silicon surface after etching by Cl_2 and HBr plasma beam are taken. The high resolution spectrum are used to quantify the relative amount of halogen on the surface after etching.

4.2.1. Low resolution surface analysis

After etching and transfer of the sample under high vacuum to the analysis chamber, XPS analysis was performed on poly-silicon. Cheng *et. al.* found that the halogenation coverage did not change appreciably after the plasma was extinguished and the gas was pumped away.[2] Consequently, surface analysis carried out after etching and then transferred to the analysis chamber under vacuum is representative of the surface during etching.

A survey spectrum of the photoemission of the poly-silicon surface after etching by 100 eV Cl_2 and HBr plasma beam are shown in Figure 4-2 and 4-3 respectively. The surface is terminated with halogen (Cl or Br) without any other measurable contamination (C or O). We also expect hydrogen present on the surface, but it cannot be identified by XPS. The spectra consist of core-level photoelectron emission peaks of Si(*2p*) and Si(*2s*) at 99 and 150 eV, Cl(*2p*) and Cl(*2s*) at 198.5 and 269.5 eV, and Br(*3s*), Br(*3p*) and Br(*3d*) at 256, 189($3p_1$), 182($3p_3$) and 70 eV respectively.

A typical low resolution spectrum recorded between binding energy 300 and 50 eV is shown in Figure 4-4. The silicon plasmon loss peaks, as indicated by arrows in Figure 4-4, are associated with the resonant inelastic scattering of photoelectrons in bulk silicon. Plasmon peak can be greatly reduced by surface contamination and have been used for diagnosing surface cleanliness.[3]

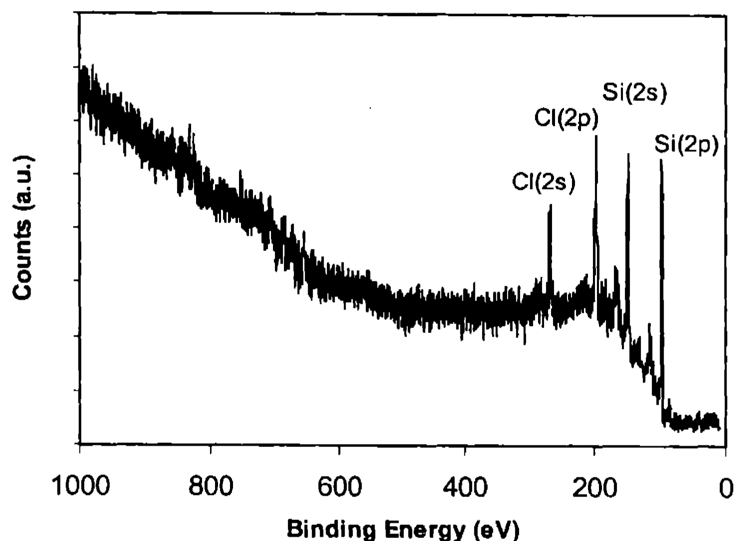

Figure 4-2: A survey spectrum of photoemission of the poly-silicon surface after etching by 100 eV Cl_2 plasma beam. The surface is highly terminated with Cl without measurable surface contamination (C or O). The take-off angle is 30°.

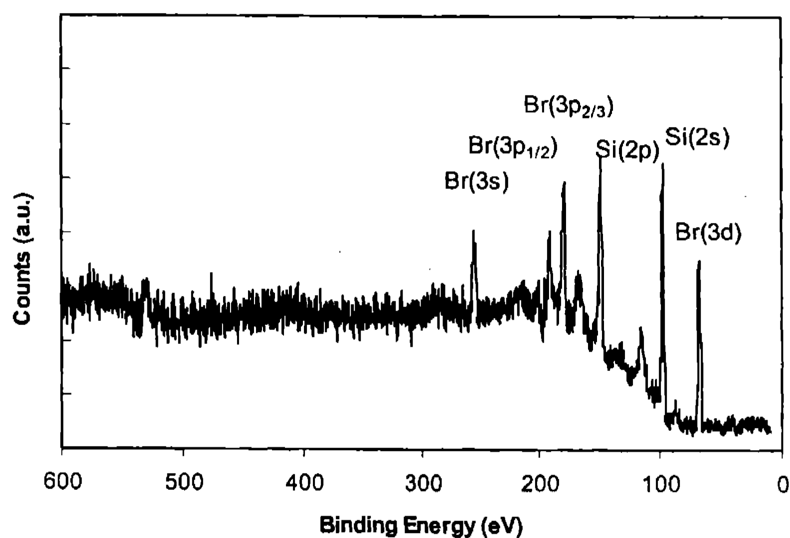

Figure 4-3: A survey spectrum of photoemission of the poly-silicon surface after etching by 100 eV HBr plasma beam. The surface is highly terminated with Br without measurable surface contamination (C or O). H is also expected to be adsorbed onto the surface, which cannot be identified by XPS. The take-off angle is 30°.

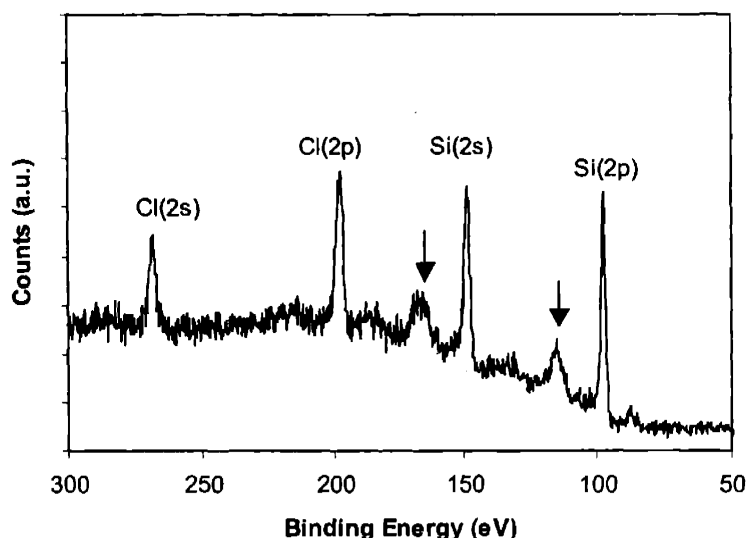

Figure 4-4: Photoemission of silicon and chlorine from a poly-silicon surface after etching by 100 eV Cl_2 plasma beam. Plasmon loss peaks of Si(*2p*) and Si(*2s*) are observed, as indicated by the arrows. The take-off angle is at 30°.

4.2.2. High resolution surface analysis

A higher resolution of silicon and chlorine photoemission spectra taken after etching at 30° take-off angle are shown in Figure 4-5. The relative chlorine to silicon signal was determined by the following equation:

$$C_i = \frac{n_i}{\sum_i n_i} = \frac{I_i / s_i}{\sum_i (I_i / s_i)} \qquad (4\text{-}1)$$

The integrated intensity of the Cl(*2p*) and Si(*2p*) peaks are normalized with their atomic sensitivity factors, $s_{Cl(2p)} = 0.48$, $s_{Si(2p)} = 0.17$, respectively.

The Cl(*2p*) and Br(*3d*) XPS spectra are shown in Figure 4-6 for poly-silicon surface after etching with different HBr:Cl_2 ratios. Both Br and Cl are adsorbed on poly-silicon after etching in HBr+Cl_2 plasmas, and the XPS signal increases with increasing proportion of the respective halogen in the feed gas. Hydrogen is also expected to be adsorbed on the surface that, however, cannot be identified by XPS. Small Br(*3d*) and Cl(*2p*) signals in pure Cl_2 and HBr plasmas, respectively, are due to residual HBr and Cl_2 desorbing from the walls of the chamber.

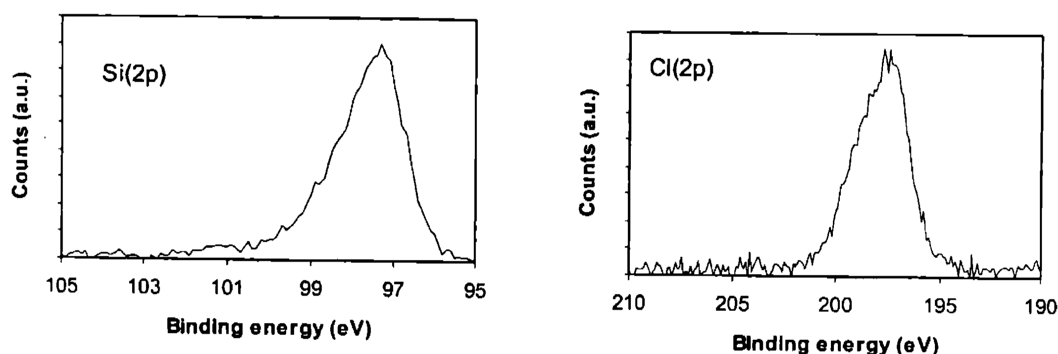

Figure 4-5: Photoemission spectra of Si(*2p*) and Cl(*2p*) from a poly-silicon surface after etching by 100 eV Cl_2 plasma beam. The take-off angle is at 30°.

The integrated XPS peak intensities for Cl(2*p*), Br(3*d*), and Cl(2*p*)+Br(3*d*) relative to Si(2*p*) are shown in Figure 4-7 All the intensities are divided by XPS atomic sensitivity factors to correct the kinetic energy dependence of the spectrometer detection efficiency. Relative coverage of Cl can be compared to that of Br with the XPS intensities. The Br coverage increases monotonically with the proportion of HBr in feed gas. The Cl coverage after etching with pure Cl_2 plasma beam is about 1.4 times higher than the Br coverage after etching with pure HBr plasma beam. Cheng *et. al.* observed a coverage difference of a factor of 1.6.[4] As suggested by the authors, the lower Br coverage is likely due to site blocking by coadsorbed H and adjacent adsorption site blocking by the larger Br atom (atomic radii of Cl and Br are 0.97 and 1.12 Å, respectively).

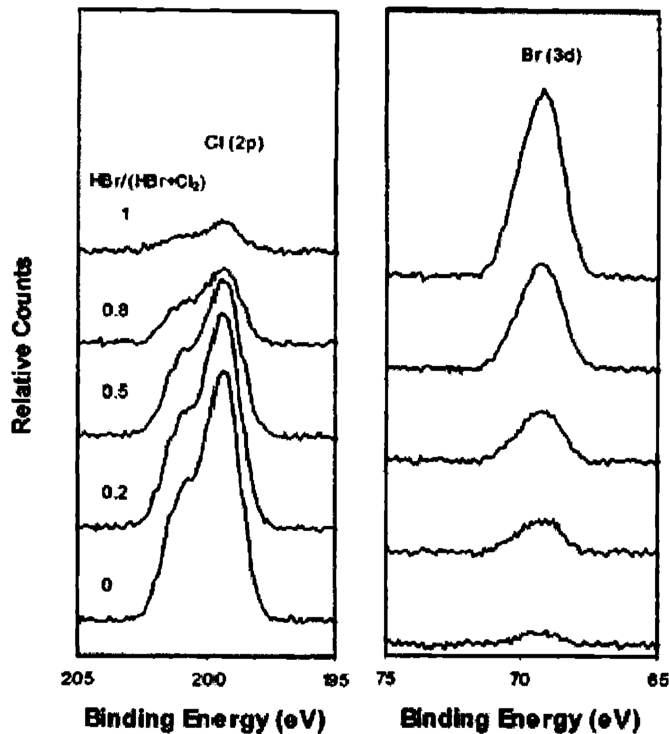

Figure 4-6: XPS spectra of Cl (*2p*) and Br (*3d*) on poly-silicon after etching in Cl_2+HBr plasmas. The top four spectra have their intensities offset for clarity. The XPS signal increases with increasing proportion of the respective halogen in the feed gas. Small Br(3*d*) and Cl(2*p*) signals in pure Cl_2 and HBr plasmas, respectively, are due to residual HBr and Cl_2 desorbing from the walls of the chamber.

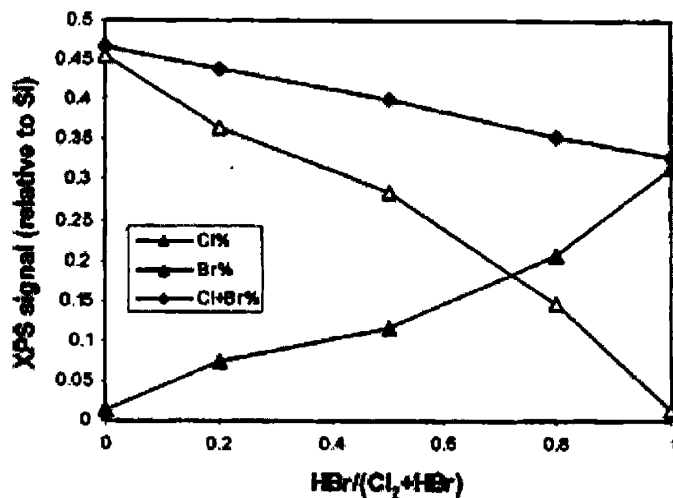

Figure 4-7. XPS integrated peak intensities [normalized to Si (*2p*) and corrected for sensitivity differences] after etching in Cl_2+HBr plasma. The Cl coverage after etching with pure Cl_2 plasma beam is about 1.4 times higher than the Br coverage after etching with pure HBr plasma beam. The lower Br coverage is likely due to site blocking by coadsorbed H and adjacent adsorption site blocking by the larger Br atom.

Cheng *et. al.* also proposed that the slower etching rate with HBr plasma beam is due to less halogen present on the surface at saturated coverage and, hence, lower ion enhanced rate of formation of volatile products such as $SiBr_2$.[4] This was tested in the following way:

(1) clean the QCM crystal surface by 300 eV Ar^+ bombardment;

(2) turn on Cl_2 plasma beam and etch the QCM crystal;

(3) turn off Cl_2 plasma beam and pump away the gas;

(4) turn on Ar plasma beam and clean the QCM crystal surface;

(5) turn on HBr plasma beam and etch the QCM crystal;

(6) turn off HBr plasma beam and pump away the gas; and

(7) turn on Ar plasma beam and clean the QCM crystal surface.

In this way, the effect of halogenation layer on top of silicon substrate on ion enhanced etching rate can be investigated. The film thickness during these steps is monitored and the etching rates are calculated as a function of time, as shown in Figure 4-8. It should be noted that there is actually some time gap between two adjacent steps to eliminate the influence of preceding step.

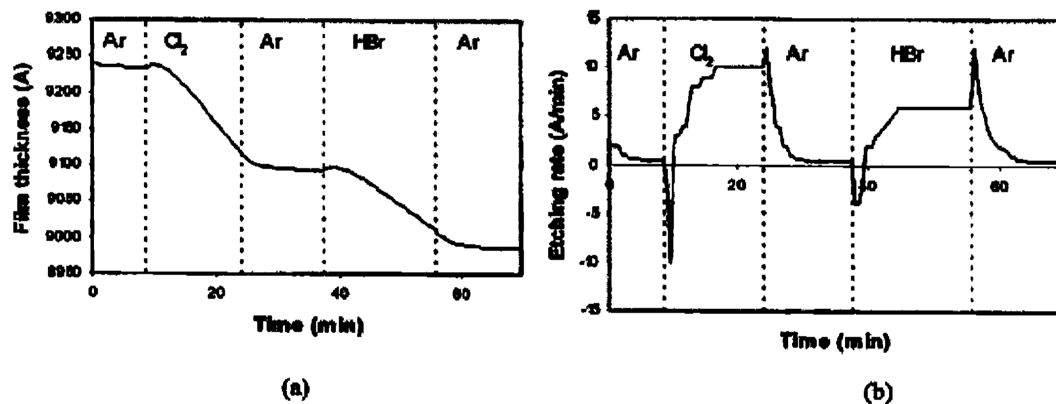

Figure 4-8. QCM measurement of (a) film thickness and (b) etching rate under different plasma beam bombardment.

When we turn on the Cl_2 plasma, the film thickness slightly increases initially, and then starts decreasing. This is probably because on a clean surface, Cl^+ tends to be incorporated into silicon lattice, and Cl neutrals are also adsorbed onto the surface, resulting in net deposition. As the surface is saturated with Cl, the etching rate increases and gradually reaches a steady state. We then turn off the Cl_2 plasma, and pump away the gas. The top

halogenation layer is stable, so we would expect that the surface conditions are similar to those during etching. The Ar plasma is turned on, and a much higher initial etching rate than Ar^+ sputtering rate of clean silicon surface is observed. The enhanced Ar^+ sputtering rate is almost the same as Cl_2 plasma beam etching rate due to the existence of the halogenation layer on top of the silicon substrate. The etching rate then drops as the surface is depleted of Cl. After the removal of about 15-25 Å of the top layer, the etching rate reaches the Ar^+ sputtering rate of the clean silicon surface, indicating the thickness of halogenation layer is on the order of 15-25 Å.

After the surface is cleaned with Ar^+ bombardment, the HBr plasma is turned on. Similarly to Cl_2, the film thickness increases at first, and then net etching dominates. The steady state etching rate by HBr plasma beam is about 40% lower than Cl_2. we then turn off the HBr plasma, pump away the gas, and turn on the Ar plasma. Surprisingly, the etching rate is almost the same as when the surface is saturated with Cl, although the Br coverage is 1.4 times lower than the saturated Cl coverage. One possible reason for this is that the surface is also covered with H, which is not identified by XPS but can still contribute to the formation of volatile products such as SiH_xBr_y; thus the ion enhanced etching. Therefore, the slower etching rates with HBr plasmas are mainly due to the lower ion flux, rather than the lower halogenation coverage.

This is consistent with the results of Vitale who observed that the etching yields in HBr plasmas are significantly higher than those in Br_2 plasmas and suggested that small hydrogen atoms can squeeze in between large bromine atoms on the silicon surface to occupy sites that are sterically hindered to bromine and can penetrate into the lattice and break the silicon backbonds which are difficult for Br atoms to reach, thus enhancing the silicon etching.[5]

4.2.3. Deconvolution of Si(2p) spectral

High resolution Si(2*p*) spectrum was recorded to determine the nature of the $SiCl_x$ layer. Figure 4-9 shows a spectrum recorded after etching. A broad tail appears, extending from 100 eV to 104 eV, and is attributed to SiCl, $SiCl_2$, and $SiCl_3$. Figure 4-10 is an expanded, processed version of the Si(2*p*) regions of Figure 4-9. First, a nonlinear (Shirley-shaped) background was subtracted from the initial XPS spectrum. The $2p_{1/2}$ component was then

removed as described elsewhere, assuming a spin-orbit splitting of 0.61 eV and an intensity ratio ($2p_{3/2}/2p_{1/2}$) of 1.92. The fit (solid line) to the data (solid circles) includes four peaks with Gaussian shapes. In addition to Si(bulk) at 99.4 eV, three features ascribed to SiCl, $SiCl_2$, and $SiCl_3$ were identified at 100.2, 101.2, and 102.3 eV, respectively. These binding energies are in good agreement with those reported by Durban *et. al.* in synchrotron photoemission studies of the chlorination of Si(111) with Cl_2.[6]

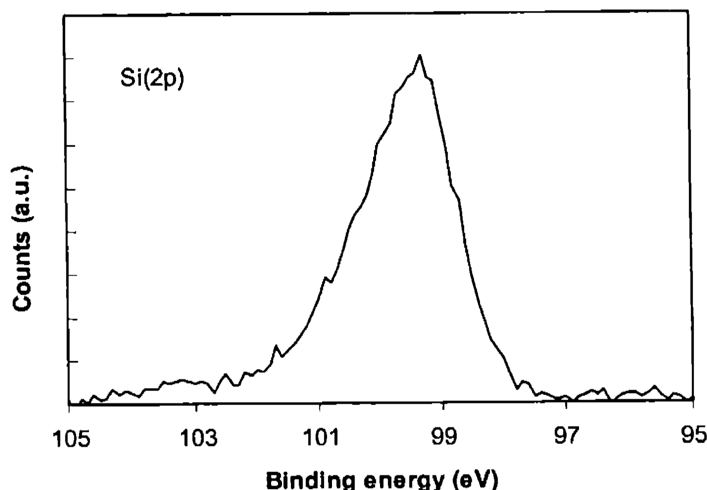

Figure 4-9: Photoemission spectra of Si(*2p*) from a poly-silicon surface after etching by 100 eV Cl_2 plasma beam. Take-off angle is at 30°.

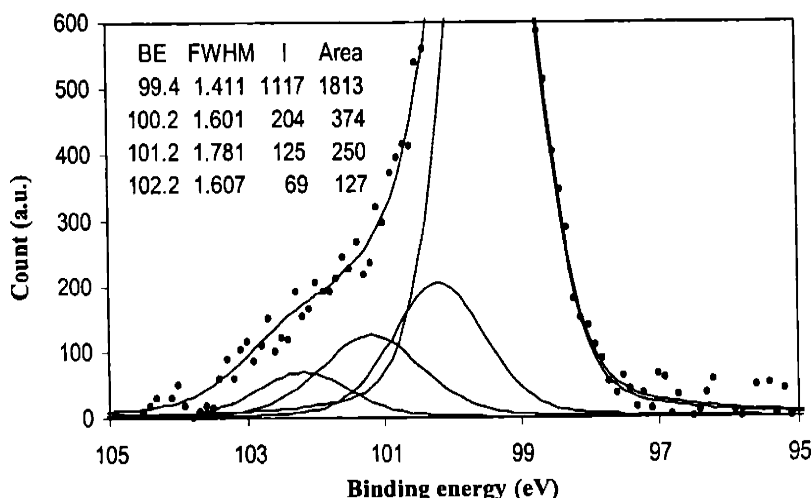

Figure 4-10: Si(*2p*) XPS spectrum for poly-silicon after etching by 100 eV Cl_2 plasma beam. The $2p_{1/2}$ component has been removed, assuming a spin-orbit splitting of 0.61 eV and a $\frac{1}{2}:\frac{3}{2}$ intensity ratio of 0.52:1. The take-off angle is 30°. The fit (solid line) includes four peaks. No parameters were constrained during the iterative fitting procedure. The peak intensities (I),

full-width at half-maximum (FWHM), peak binding energy (BE), and integrated peak intensities (AREA) for the four peaks are given in the table contained in the figure. The relative areas for $SiCl$:$SiCl_2$:$SiCl_3$ are 1.00:0.67:0.34.

We fit four peaks to the observed spectrum. The peak binding energies for Si(bulk), SiCl, $SiCl_2$, and $SiCl_3$ were constrained to the above values in the first few iterations of the fitting procedure. Then all the parameters (binding energies, widths, and peak-center intensities) were allowed to vary during subsequent iterations. The nonlinear least-squares fit yielded binding energy shifts (relative to bulk Si) of 0.8, 1.0, and 1.0 eV for the respective Si chlorides, in excellent agreement with the results of Whitman *et. al.*[7] The area ratios of these three peaks were 1.00:0.67:0.34, meaning that 70% of the chlorine on the surface is in the form of the di- and trichlorides. Because the peaks are not resolved, there is considerable uncertainty in the peak widths and thus relative proportions of $SiCl_{2(ads)}$ and $SiCl_{3(ads)}$. However, the sum of $SiCl_{2(ads)}$+$SiCl_{3(ads)}$ peak area relative to SiCl is much more precise and so the conclusion that during exposure to the plasma beam most of the adsorbed Cl is present as higher silicon chlorides remains unchanged.

The relative chlorine to silicon signal can also be determined by the following equation:

$$C_i = \frac{Area_{SiCl} + 2Area_{SiCl_2} + 3Area_{SiCl_3}}{Area_{Si} + Area_{SiCl} + Area_{SiCl_2} + Area_{SiCl_3}} \qquad (4\text{-}2)$$

Using this method, we calculate the Cl:Si is 0.49, quite close to the value derived by integrating the areas below Cl(*2p*) and Si(*2p*) peaks independently, 0.45. Therefore, the Cl:Si on the surface is verified by the agreement of results from these two methods.

The Si(*2p*) spectral of poly-silicon after etching by 100 eV HBr plasma beam is processed similarly, as shown in Figure 4-11. We also fit four peaks to the observed spectrum, corresponding to Si(bulk), SiBr, $SiBr_2$ and $SiBr_3$. The binding energy shifts are 0.7, 1.6, and 2.5 eV respectively. The area ratios of these three peaks were 1.00:0.53:0.23, also suggesting that more than 60% of the bromine on the surface is in the form of the di- and tribromide. The Br:Si calculated using Equation (4-2) is 0.31, also very close to the value derived by integrating the areas below Br(*3d*) and Si(*2p*) peaks independently. Both the results of binding energy shifts and area ratios agree well with the results of Cheng *et. al.*[8]

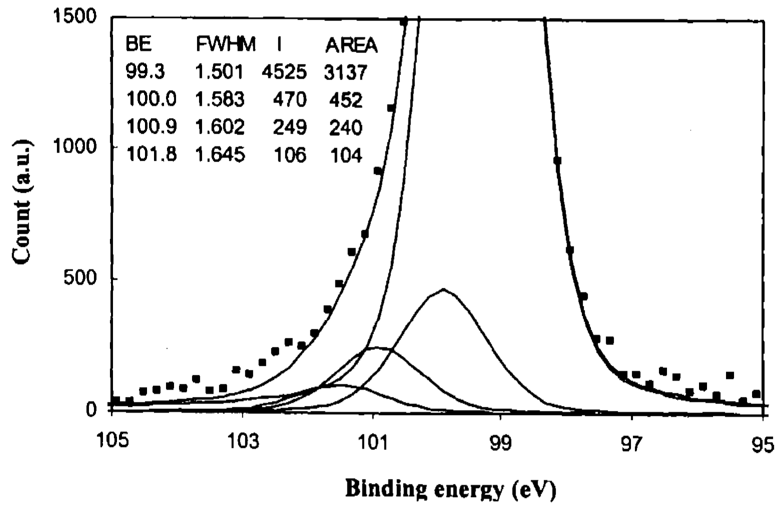

Figure 4-11: Si(*2p*) XPS spectrum for poly-silicon after etching by 100 eV HBr plasma beam. The take-off angle is 30°. The fit (solid line) includes four peaks. No parameters were constrained during the iterative fitting procedure. The relative areas for SiBr:$SiBr_2$:$SiBr_3$ are 1.00:0.53:0.23.

4.3. Depth profile analysis

The concentration of species derived from integration of specific peak is weighted average of the concentration in the top layer of the thickness comparable to the mean free path of the photoelectron. At low take-off angle, the species on the top surface will be weighted more, therefore enhancing the surface sensitivity.

The reason for this effect is simply demonstrated by reference to Figure 4-12. If λ is the attenuation length (AL) of the emerging electron, then 95% of the signal intensity is derived from a distance 3λ within the solid. However, the vertical depth sampled is clearly given by

$$d = 3\lambda \sin\alpha \tag{4-3}$$

and this is at maximum when $\alpha = 90^{o}$. In the case of a substrate (s) with a uniform thin overlayer (o), the angular variation of intensities is given by

$$I_s^d = I_s e^{-d/\lambda \sin\alpha} \tag{4-4}$$

$$I_o^d = I_o (1 - e^{-d/\lambda \sin\alpha}) \tag{4-5}$$

Under real situation, the concentration in the overlayer is not uniform, instead has a distribution as the depth increases. The angular dependent signal intensities depend on the

distribution. Therefore, it is possible to derive the concentration distribution from the measured angular dependent signal intensities.

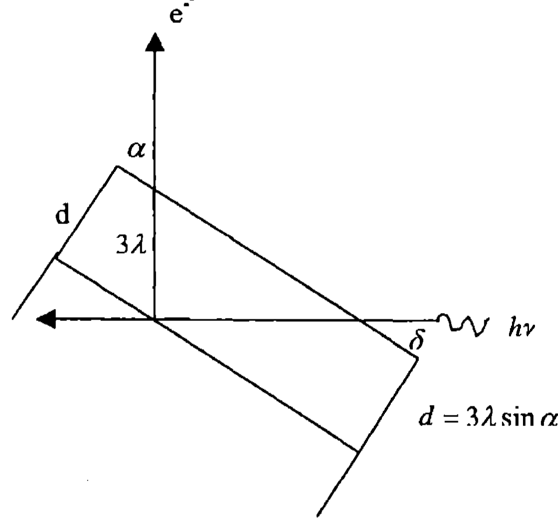

Figure 4-12: The illustration of surface sensitivity enhancement by variation of the electron take-off angle.

4.3.1. Depth profile inversion method

XPS spectra were recorded for poly-silicon films before exposure to plasma beam. As expected, the Si(*2p*) regions consists of two peaks: SiO_2 (104.0 eV) and Si (99.5 eV) from the underlying substrate. A typical depth profile obtained from an inversion of the integrated Si (*2p*) and O (*1s*, 533.4 eV) intensities in Figure 4-13 is shown in Figure 4-14.

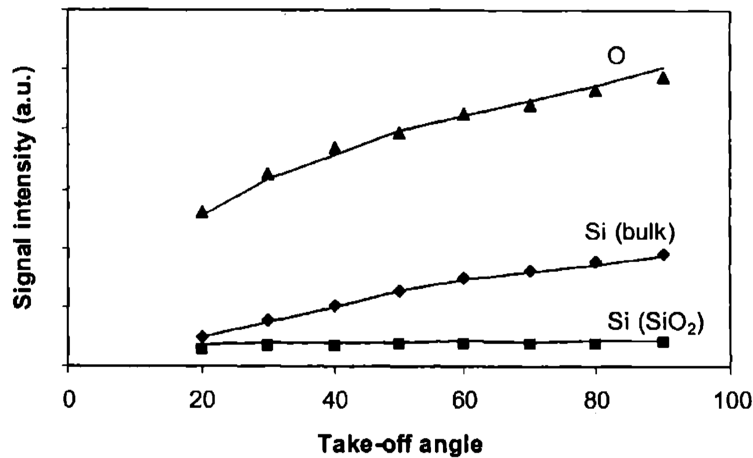

Figure 4-13: Signals from Si(*2p*) (underlying Si substrate), Si(*2p*) (from SiO_2), and O(*1s*) for a 20 Å SiO_2 film on a poly-silicon substrate versus the XPS photoelectron take-off angle before etching. The points are experimental data, and the curves are fits, based on the model described.

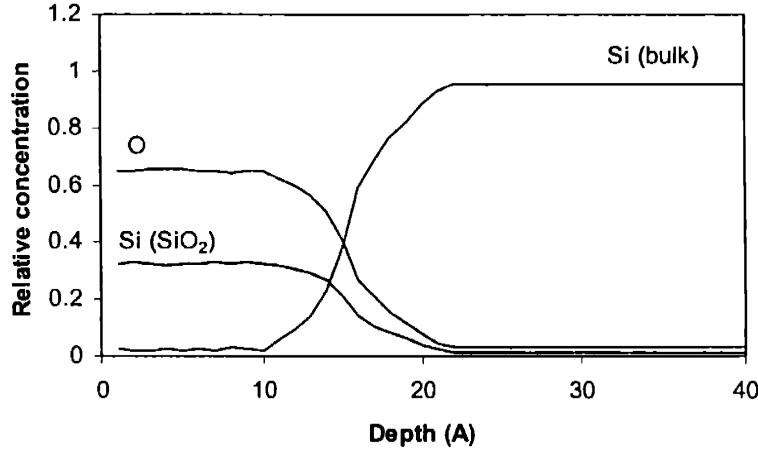

Figure 4-14: Depth profile for a 20 Å SiO_2 film, computed from the inversion of the angle-resolved data presented in Figure 4-13.

The inversion process involves minimizing the quantity Q:[9]

$$Q = \frac{\chi^2}{2} \tag{4-6}$$

where χ^2 is defined as:

$$\chi^2 = \sum_{j,k} \frac{[I(j,\theta_k)^{calc} - I(j,\theta_k)^{obs}]^2}{\sigma(j,\theta_k)^2} \tag{4-7}$$

$I(j,\theta_k)^{calc}$ and $I(j,\theta_k)^{obs}$ are, respectively, the calculated and observed total XPS intensity for species j at take-off angle θ_k, $\sigma(j,\theta_k)^2$ is the variance.

The XPS signal from slab i for species j is:

$$\begin{aligned} s(i,j,\theta_k) &= a(j,\theta_k)c(i,j)\exp(-dz/\lambda_{1,j}\sin\theta_k)\times\exp(-dz/\lambda_{2,j}\sin\theta_k)\cdots \\ &\times\exp(-dz/\lambda_{i-1,j}\sin\theta_k)\times\exp(-dz/2\lambda_{i,j}\sin\theta_k) \end{aligned} \tag{4-8}$$

where $a(j,\theta_k)$ is a proportionality constant for species j at a take-off angle θ_k, $c(i,j)$ is the concentration of species j in slab i, and dz is a thickness of the slabs (set equal to 1 Å). The atom densities of SiO_2 and Si are 6.92×10^{22} and 5.00×10^{22} cm^{-3}, respectively. We used electron attenuation lengths of 38 Å in SiO_2 and 22 Å in Si at the kinetic energy of bulk Si(*2p*) photoelectrons.[10-12] The electron attenuation length, $\lambda_{i,j}$, for slab i was assumed to be proportional to the fraction of the Si and SiO_2 in the layer, and to depend on the kinetic energy of photoelectrons from species j by the empirical relationship:[13-16]

$$\lambda_{i,j} = \lambda_{i,1}\left(\frac{E_{x-ray} - E_{b,j}}{E_{x-ray} - E_{b,1}}\right)^{0.7} \qquad (4\text{-}9)$$

where $E_{b,j}$ and $E_{b,1}$ are the binding energies of species j and the Si substrate [Si(*2p*)], respectively.

The proportionality constant, $a(j,\theta_k)$, is the product of three terms: the XPS sensitivity factor, the transmission of the energy analyzer, and the take-off angle-dependent fraction of electrons emanating from the sample surface that are collected by the input lens. The XPS sensitivity factors are 0.817, 2.84, 2.285, and 1.0 for Si(*2p*), Br(*3d*), Cl(*2p*), and C(*1s*), respectively. The second term is reported by the manufacturer to be independent of energy at the low resolution used and the relatively small range of electron energies encountered (1388-955 eV). The third factor is a function of the take-off angle dependent, elliptical geometric projection of the circular X-ray beam on the sample, and the overlap between this beam and the area of the sample "seen" by the electron collection lens. Rather than calculate this proportionality constant, we simply fit it.

4.3.2. Depth profile for poly-silicon sample before etching

The thickness of the SiO_2 film determined from the angle-resolved inversion method was 20 Å, in good agreement with that measured by ellipsometer. An apparent broadening of the SiO_2/Si interface over 5 Å reflects the resolution of this depth profiling method. The O:Si ratio for the 20 Å film, integrated throughout the film was 2:1, in reasonable agreement with the expected film stoichiometry of 2:1.

4.3.3. Depth profile for poly-silicon sample after etching by Cl_2 plasma beam

Angle-resolved XPS intensities for a poly-silicon sample after exposure to 100 eV Cl_2 plasma beam are shown in Figure 4-15. The fraction of Cl signal in the film (solid triangles and line) falls off by 34% between θ=20° and 90°, indicating that Cl is more concentrated near the surface. The depth profile derived from the data in Figure 4-15 is presented in Figure 4-16. Cl is found to peak at the surface, fall by one half at 10 Å and decay to near-zero concentration by 25 Å.

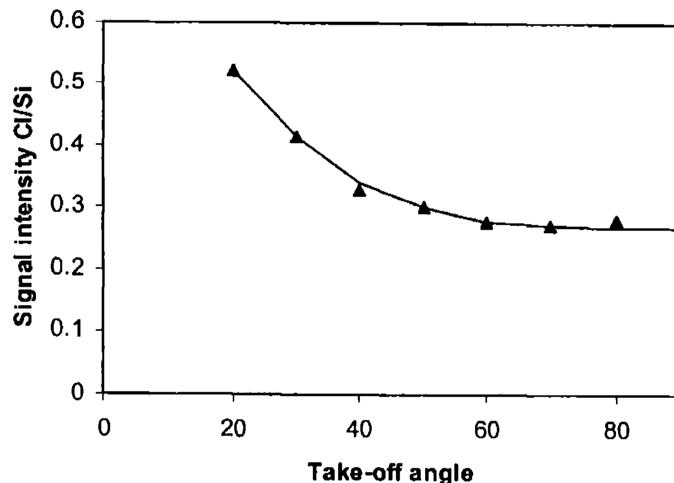

Figure 4-15: Signal from Si(2p) and Cl(2p) versus photoelectron take-off angle after etching by 100 eV Cl_2 plasma beam.

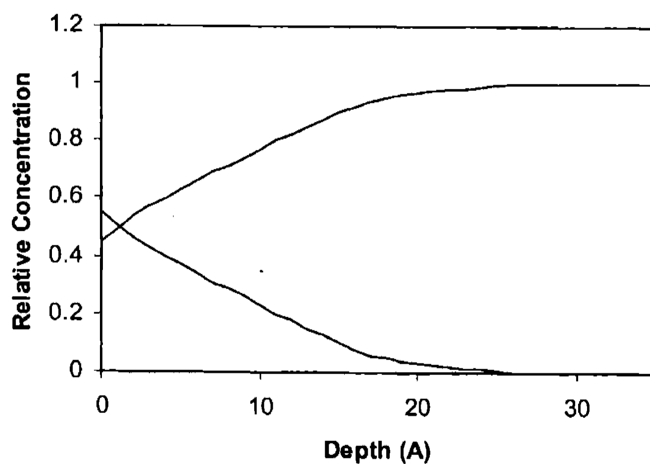

Figure 4-16: Depth profile of poly-silicon sample after etching by 100 eV Cl_2 plasma beam. Cl is found to peak at the surface, fall by one half at 10 Å and decay to near-zero concentration by 25 Å.

4.4. Conclusions

The XPS peak for Cl(2p), Br(3d), and Si(2p) are integrated to quantify the relative concentration of different species on the sample surface after exposure to the plasma beam. The Cl coverage after etching with pure Cl_2 plasma beam is about 1.4 times higher than the Br coverage after etching with pure HBr plasma beam. The lower Br coverage is likely due to site blocking by coadsorbed H and adjacent adsorption site blocking by the larger Br atom.

The Si(*2p*) was deconvoluted to differentiate Si(bulk), SiCl, $SiCl_2$ and $SiCl_3$. About 70% of the chlorine bromine adsorbed onto the surface is in the form of di- and tri-chloride. Similar results are observed for bromine. Inversion method was used to extract the depth profile from the angular resolved XPS measurement. The halogenation layer is about 15 – 25 Å thick, and the concentration of halogen decays exponentially as depth increases.

4.5. Reference

1. I. Bello, W. H. Chang, and W. M. Lau, *J. Appl. Phys.* **75**, 3092 (1994).

2. C. C. Cheng, K. V. Guinn, V. M. Donnelly, and I. P. Herman, *J. Vac. Sci. Technol. A* **12**, 2630 (1994).

3. D. Briggs and M. P. Seah, *Practical Surface Analysis*, New York, John Wiley & Sons (1983).

4. C. C. Cheng, K. V. Guinn, I. P. Herman, and V. M. Donnelly, *J. Vac. Sci. Technol. A* **13**, 1970 (1995).

5. S. A. Vitale, H. Chae, and H. H. Sawin, *J. Vac. Sci. Technol. A* **19**, 2197 (2001).

6. T. D. Durbin, W. C. Simpson, V. Chakarian, D. K. Shuh, P. R. Varekamp, C. W. Lo, and J. A. Yarmoff, *Surf. Sci.* **316**, 257 (1994).

7. L. J. Whitman, S. A. Joyce, J. A. Yarmoff, F. R. McFeely, and L. J. Terminello, *Surf. Sci.* **232**, 297 (1990).

8. C. C. Cheng, K. V. Guinn, and V. M. Donnelly, *J. Vac. Sci. Technol. B* **14**, 85 (1996).

9. G. C. Smith and A. K. Livesey, *Surf. Interface Anal.* **19**, 175 (1992).

10. F. H. Bell and O. Joubert, *J. Vac. Sci. Technol. B* **14**, 3473 (1996).

11. N. Layadi, V. M. Donnelly, and J. T. C. Lee, *J. Appl. Phys.* **81**, 6738 (1997).

12. M. P. Seah and W. A. Dench, *Surf. Interface Anal.* **1**, 2 (1979).

13. S. Tanuma, C. J. Powell, and D. R. Penn, *Surf. Interface Anal.* **17**, 927 (1991).

14. H. Ebel, M. F. Ebel, R. Svagera, and A. Hoffmann, *Surf. Interface Anal.* **18**, 821 (1992).

15. C. D. Wagner, L. E. Davis, and W. M. Riggs, *Surf. Interface Anal.* **2**, 55 (1980).

16. D. F. Mitchell, K. B. Clark, J. A. Bardwell, W. N. Lennard, G. R. Massoumi, and I. V. Mitchell, *Surf. Interface Anal.* **21**, 44 (1994).

Chapter 5. Beam study of oxygen effect and loading effect

During the poly-silicon etching process, oxygen is often added to Cl_2/HBr discharge to improve selectivity with respect to SiO_2 or to reduce undercutting of the mask. The slowing of the SiO_2 etch rate is accompanied by a proportionately smaller reduction in the silicon etch rate.[1] This is due to formation of a steady-state coverage of a silicon oxide layer that is competitively being deposited and etched. Oxidation competes with chlorination. The goals of this work are to understand the etching kinetics with the addition of oxygen, and to measure the parameters needed for profile evolution models.

Due to the high etching rate in a low-pressure, high-density inductively coupled plasma etching process, the etching products can build up to appreciable concentrations and correspondingly the reactant is depleted.[2] In addition to the depletion of reactants, which decreases the etchant species surface coverage, etching products can be fragmented upon collision with energetic electrons, with subsequent deposition on the substrate and chamber walls.[3,4] Therefore, high pumping speed is needed to sweep the etching products out of the chamber.

The etching product can deposit on the substrate surface, both in the form of ions and neutrals, and modify surface conditions, affecting the etching uniformity, and other etching properties such as RIE lag.[5] The deposition on the feature sidewall can also affect the feature profile.

In the poly-silicon etching with Cl_2, volatile etching products such as $SiCl_4$ do not appreciably react with surfaces, but they can build up an appreciable concentration (~10%) which is inversely proportional to the gas flow rate.[2] Electron impact dissociation of $SiCl_4$ produces Si-containing species such as $SiCl_2$, which has a higher sticking probability than that of $SiCl_4$, and can deposit readily on silicon surfaces. Less volatile etching byproducts such as $SiCl_2$ would leave the surface upon ion bombardment and redeposit on the sidewall of the feature where less ion bombardment occurs.

5.1. Oxygen effect on poly-silicon etching rate

O_2 is added to Cl_2 feed gas to study the effect of adding oxygen in a real commercial inductively coupled plasma etcher.

5.1.1. The influence of oxygen addition on poly-silicon etching with Cl_2

The etching yields under various oxygen concentration in the feed gas are shown in Figure 5-1. The etching yield is measured at two different ion bombardment energy levels, 50 eV and 150 eV, and with substrate temperature of 30°C.

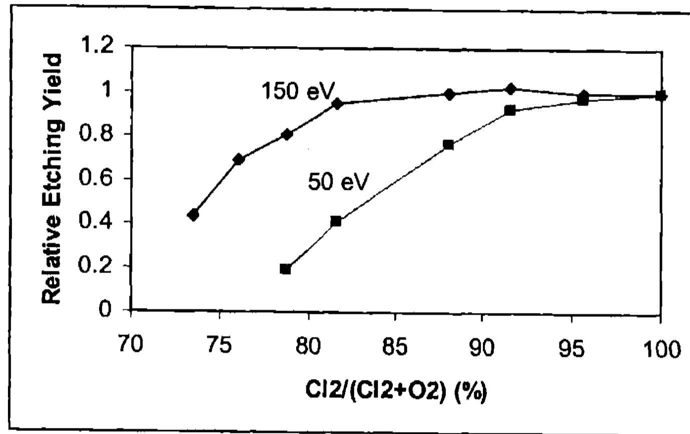

Figure 5-1: Effect of oxygen addition on the etching yield of silicon in Cl_2 discharge. When the concentration of O_2 in the feed gas is less than 5%, the effect of oxygen addition is indistinguishable. The etching yield exhibits a rapid falloff above ~20% added O_2. At lower ion bombardment energy level, the effect is more significant than at higher level.

When the concentration of O_2 in the feed gas is less than 5%, the effect of oxygen addition is indistinguishable. This suggests that when the fraction of oxygen on the surface is small, oxygen can be removed in the form of $SiOCl_x$, since $SiOCl_x$ is still a volatile product and therefore, the etching yield is not affected. The etching yield exhibits a rapid falloff above ~20% added O_2, suggesting that formation of SiO_x on the surface begins to dominate and hence stop the etching process above 30% O_2. Cheng *et. al.* also observed the insignificant effect of oxygen addition on silicon etching rate below 5% and the abrupt falloff of etching rate over 20% O_2 addition using an ECR source.[1]

It can be seen that at lower ion bombardment energy level, the effect is more significant than at higher level. It's probably because at higher energy level, comparatively more Si-O can be broken and therefore deposited oxygen can be readily removed from the surface, which in turn reduced the effect of oxygen on the etching yield.

5.1.2. The influence of oxygen addition on poly-silicon etching with HBr

The effect of oxygen addition on HBr etching of poly-silicon is shown in Figure 5-2. The effect on HBr etching has similar pattern as that on Cl_2 etching except that it's more significant on HBr etching. At 5% oxygen addition, the etching yield reduced by 10% in HBr at 50 eV, as compared with 5% in Cl_2. This is probably because that oxygen has advantage of adsorption onto the surface compared with bromine due to its smaller size.

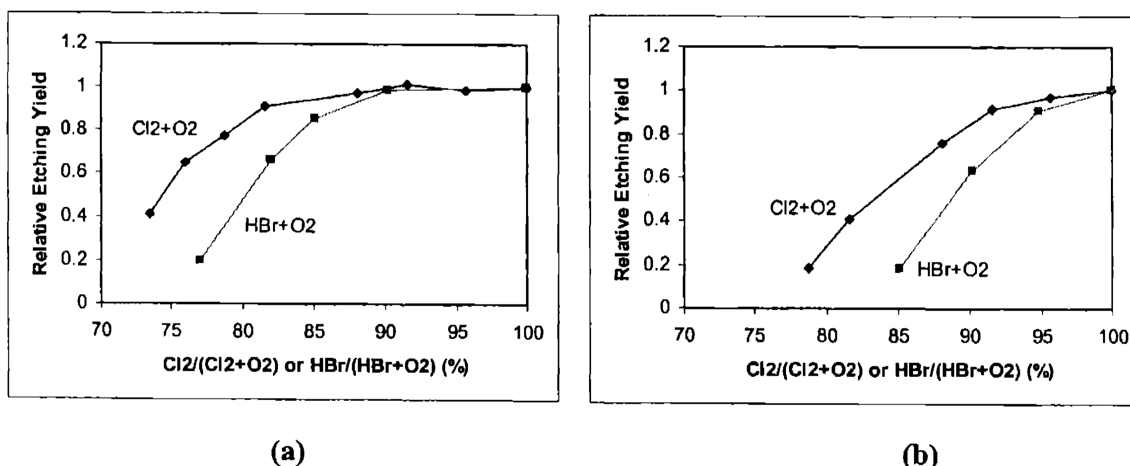

Figure 5-2: Comparison of effect of oxygen addition on silicon etching yield in Cl_2 discharge and HBr discharge at different ion bombardment energy. (a) 150 eV; (b) 50 eV. The effect on HBr etching has similar pattern as that on Cl_2 etching except that it's more significant on HBr etching.

5.1.3. Surface analysis after etching with oxygen addition

After etching and transfer of the sample under high vacuum to the analysis chamber, X-ray photoelectron spectroscopy was taken on poly-silicon sample. The area below Si(*2p*) and O(*1s*) peak is integrated, the ratio of O/Si is calculated, as shown in Figure 5-3.

It seems that both oxygen coverage and etching yield exhibit a rapid change at ~20% oxygen addition. This suggests that formation of SiO_xCl_y species on the surface is important

in suppressing etching of Si when the oxygen fraction has accumulated to certain level, and that the surface need not be converted completely to SiO_2 to reach an etch stop.

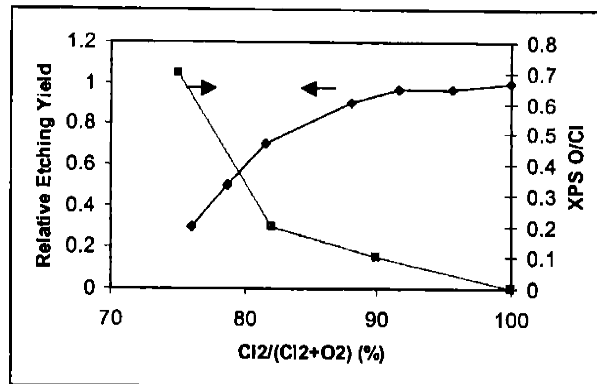

Figure 5-3: Effect of oxygen addition on etching yield of silicon in Cl_2 discharge and surface composition. Ion bombardment energy =100 eV.

From Figure 5-3, we can see that the etching rate has a different sensitivity to the oxygen addition with different surface composition. When the surface is chlorine rich, for example, poly-silicon with exposure to Cl_2 plasma, the etching rate is not sensitive to small amount of oxygen addition. When the surface is oxygen rich, for example, silicon oxide with exposure to Cl_2 plasma, the etching rate is more sensitive to oxygen addition. This explains that in a real commercial etcher, by adding small amount of oxygen (typically 5 – 10%), the poly-silicon etching rate does not change much, but the silicon oxide etching rate decreases significantly, therefore the etching selectivity can be achieved.

5.2. Loading effect on the etching rate

$SiCl_4$ is added to Cl_2 to mimic the effect of etching product buildup in a commercially available inductively coupled plasma etcher.

5.2.1. The influence of $SiCl_4$ addition on etching yield

The ion flux under different compositions is shown in Figure 5-4, and the etching rate is shown in Figure 5-5. The etching yield, defined as number of silicon atoms removed per incoming ion, is shown in Figure 5-6. All data presented were taken with ion energy of 100 eV and substrate temperature under 30°C. With the increase of $SiCl_4$ in the feed gas, the ion

flux gradually decreases probably due to the lower ion density in the plasma or/and the increased deposition of Si-containing ions on the extraction grid. With the increase of $SiCl_4$, etching rate also slows down due to the deposition of Si-containing species on the substrate surface, which has to be etched again. The effect of $SiCl_4$ addition on the etching yield is significant. For example, 2% addition of $SiCl_4$ reduces the etching yield by 15%. To be noted also is that the etching yield does not decrease linearly with the addition of $SiCl_4$. The reduction of etching yield decreases gradually.

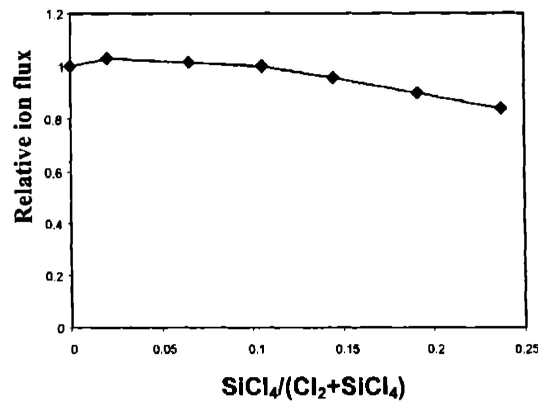

Figure 5-4: The relative ion flux as a function of $SiCl_4$ concentration in the feed gas. With the increase of $SiCl_4$ in the feed gas, the ion flux gradually decreases probably due to the lower ion density in the plasma or/and the increased deposition of Si-containing ions on the extraction grid.

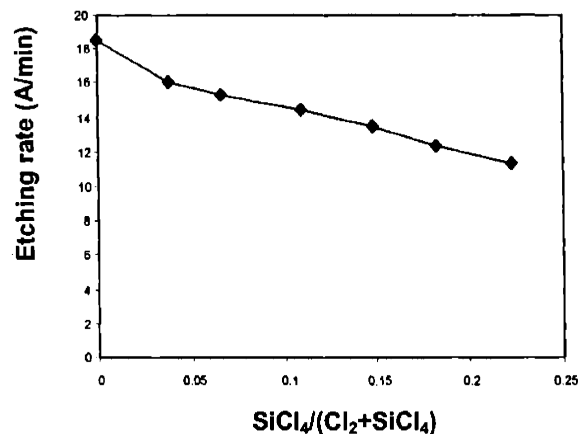

Figure 5-5: The etching rate as a function of $SiCl_4$ concentration in the feed gas. With the increase of $SiCl_4$, etching rate slows down due to the deposition of Si-containing species on the substrate surface, which has to be etched again.

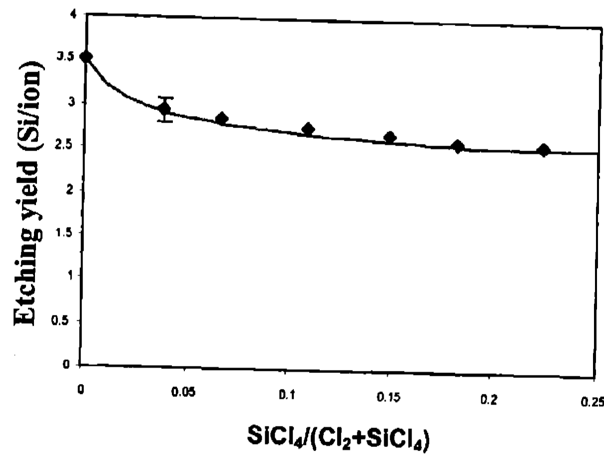

Figure 5-6: The etching yield as a function of $SiCl_4$ concentration in the feed gas. The line is model prediction explained later. The effect of $SiCl_4$ addition on the etching yield is significant. To be noted also is that the etching yield does not decrease linearly with the addition of $SiCl_4$. The reduction of etching yield decreases gradually.

5.2.2. The temperature effect on $SiCl_4$ reduction of etching yield

The reduction of etching yield with the addition of $SiCl_4$ has been attributed to the deposition of Si-containing species. The effect of $SiCl_4$ addition under different temperatures are shown in Figure 5-7. Under low concentration of $SiCl_4$, the etching yield decreases dramatically, but is relatively insensitive to the temperature change. This is probably due to the deposition of Si-containing species on the active site induced by ion bombardment, i.e. the ion enhanced deposition, which is mainly determined by rate of active sites generation, and therefore is less sensitive to substrate temperature. As the active sites are filled with deposited species, further reduction of etching yield is due to the deposition of neutrals on nonactive sites, which is relatively slow and sensitive to substrate temperature. Therefore, as the concentration of $SiCl_4$ increases, the reduction of etching yield gradually slows down, but is more sensitive to the temperature change.

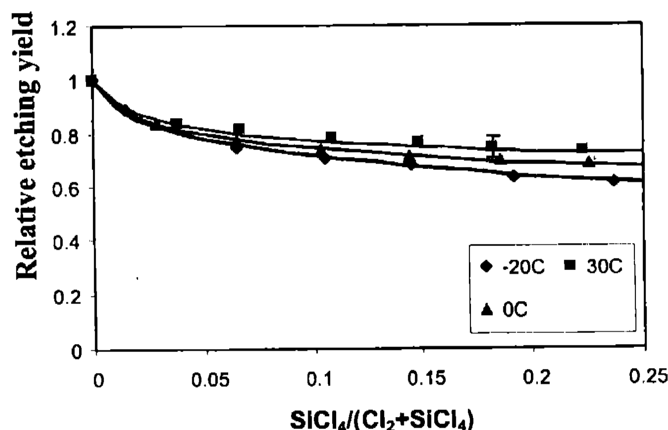

Figure 5-7: The etching yield as a function of $SiCl_4$ concentration under different substrate temperature. Lines are model predictions. Under low concentration of $SiCl_4$, the etching yield decreases dramatically, but is relatively insensitive to the temperature change. As the concentration of $SiCl_4$ increases, the reduction of etching yield gradually slows down, but is more sensitive to the temperature change.

The etching yield at different temperature for pure Cl_2, 2% $SiCl_4$ and 10% $SiCl_4$ are also illustrated in Figure 5-8. For pure Cl_2, the etching yield is approximately constant from -20 °C to 40 °C as the surface remains saturated with chemisorbed Cl atoms. As for 2% $SiCl_4$, the etching yield is suppressed by ion-enhanced deposition of Si-containing species, which is relatively temperature insensitive, and hence the temperature effect is modest. For 10% $SiCl_4$, the active sites have been filled with Si-containing species, the further reduction of etching yield is mainly due to the chemisorbtion of Si-containing species on the nonactive sites, which is relatively temperature sensitive.

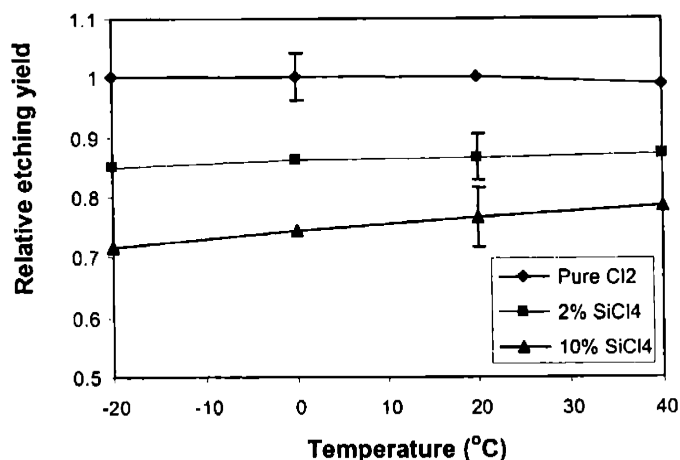

Figure 5-8: The etching yield as a function of substrate temperature for different composition. The temperature sensitivity of loading effect depends on the silicon concentration. For pure

Cl_2, etching yield does not depend on temperature, but with 10% $SiCl_4$ addition, the etching yield is very temperature sensitive.

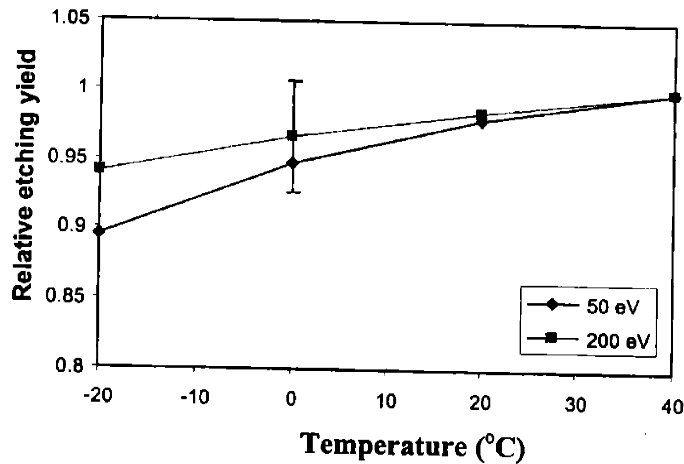

Figure 5-9: The etching yield as a function of substrate temperature under different ion energy level. Etching yield at lower energy level is more temperature sensitive probably because deposition of Si-containing species on nonactive sites is more important at lower energy level.

The temperature effect for two ion energy levels is shown in Figure 5-9. The averaged number of bonds broken by each incoming ion is proportional to the square root of ion energy, based on the collision cascade approximation.[6] With 200 eV ion energy, each incoming ion can break more bonds, resulting in more active sites. The etching yield reduction is in the ion enhanced deposition regime, and therefore is relatively temperature insensitive. With 50 eV ion energy, less active sites created by incoming ions are filled by Si-containing species, and the etching yield reduction is in the nonactive sites chemisorbtion controlled regime, therefore is rather temperature sensitive.

5.2.3. XPS analysis of surface

After etching and transfer of the sample under high vacuum to the analysis chamber, XPS analysis was performed on poly-silicon. The Cl(*2p*) and Si(*2p*) XPS spectra are shown in Figure 5-10 for polysilicon after etching with 10% $SiCl_4$ in Cl_2. Both Cl from deposited $SiCl_x$ species and adsorbed Cl neutral are on the surface, and contribute to the Cl(*2p*) XPS spectra. We can fit 4 peaks to the spectrum observed in Si(*2p*), corresponding to $Si_{(bulk)}$, SiCl, $SiCl_2$ and $SiCl_3$ respectively. The nonlinear least-squares fit yielded binding energy shifts

(relative to bulk Si) of 0.9, 2.1, and 3.3 for the respective Si chlorides, in good agreement with the results of Whitman *et. al.*[7] The relative areas for $SiCl:SiCl_2:SiCl_3$ are 1:0.22:0.19. Because the peaks are not resolved, there is considerable uncertainty in the peak widths and thus relative proportions of these peaks.

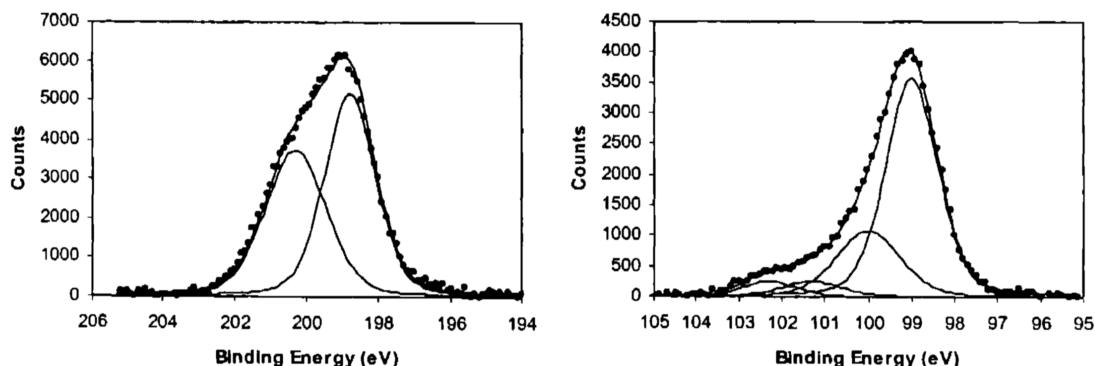

Figure 5-10: XPS spectra of Cl(*2p*) and Si(*2p*) on polysilicon after etching with 10% $SiCl_4$ in Cl_2.

The integrated XPS peak intensities for Cl(*2p*) relative to Si(*2p*) is much more precise. The integrated XPS peak intensities for Cl(*2p*) relative to Si(*2p*) are shown in Figure 5-11. With $SiCl_4$ in the feed gas, the averaged Cl/Si of Si containing species is similar to that of Si surface saturated with Cl. The halogen coverage does not change drastically with the addition of $SiCl_4$ in the feed gas. This is probably because that the deposited $SiCl_x$ species also contributes to the surface chlorination, although it competes for the surface sites with Cl neutrals.

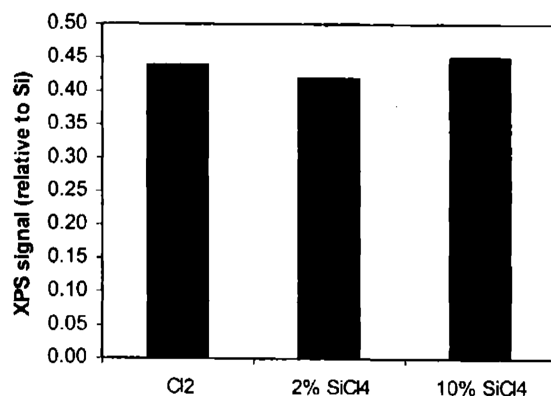

Figure 5-11: XPS integrated peak intensities [normalized to Si(*2p*) and corrected for sensitivity differences] after etching in Cl_2 plasma beam with $SiCl_4$ addition.

5.2.4. Kinetics model

The deposition of fluorocarbon species on silicon oxide has been extensively studied by researchers and ion enhanced deposition mechanism is suggested to explain the observed experimental results.[8,9] The deposition is enhanced by low energy ions striking surface, creating active sites for fluorocarbon species to deposit on. Neutrals can also be adsorbed on the nonactive sites with a relatively lower sticking coefficient. In their work, fluorocarbon species is the polymerization precursor. We believe that Si-containing species can also deposit on the silicon surface and the deposition is likely being enhanced by ion bombardment too.

Therefore, the deposition rate of Si-containing species is expressed as follows.

$$DR_{total} = DR_n + DR_i \tag{5-1}$$

where DR_{total} is total deposition rate, DR_n is neutral deposition rate, and DR_i is ion-enhanced deposition rate. Surface coverage (θ) of active sites is calculated from active site balance.

It is necessary to identify what factors make a site active. We may consider an active site to be one that has a dangling bond in its vicinity, a dangling bond being an unpaired electron of a Si atom. Active sites are generated by ions and consumed by neutral species and expressed as follows.

$$\frac{d\theta}{dt} = \Gamma_i Y_i (1-\theta) - \Gamma_{Cl} S_{Cl} \theta - \Gamma_{SiClx} S_{SiClx} \theta = 0 \tag{5-2}$$

where Γ_i is ion flux, Γ_{Cl} is Cl neutral flux, Γ_{SiClx} is Si-containing species flux, and Y_i is ion creation yield. S_{Cl} is sticking probability of Cl neutrals to active sites, and S_{SiClx} is sticking probability of Si-containing species to active sites. To simplify, we assume the active sites are mainly consumed by Si-containing species, i.e. $S_{Cl} \approx 0$. Considering the surface is nearly saturated with Cl, the sticking probability should be quite low, and therefore this simplification is rather reasonable.

$$\theta = \frac{1}{1 + \frac{\Gamma_{SiClx} S_{SiClx}}{\Gamma_i Y_i}} \tag{5-3}$$

$$DR_{total} = \Gamma_{SiClx} S'_{SiClx}(1-\theta) + \Gamma_{SiClx} S_{SiClx}\theta \tag{5-4}$$

where S'_{SiClx} is the sticking probability for Si-containing species to nonactive sites.

As the Si-containing species deposit on the surface, they are simultaneously etched, which is also enhanced by ion bombardment. A phenomenological model for Cl^+ ion-enhanced polysilicon etching with Cl has been developed by Chang *et. al.*, as shown in Table 5-1.[10]

Table 5-1. The simplified phenomenological surface kinetics model for Cl^+ ion-enhanced polysilicon etching with Cl.

Simplified kinetics model	Mechanism
$Cl_{(g)} + * \xrightarrow{s} Cl_{(s)}$	Sorption of atomic chlorine
$Cl^+_{(g)} + * \xrightarrow{C(\phi)} Cl_{(s)}$	Sorption of ionic chlorine
$Si_{(s)} + 4Cl_{(s)} \xrightarrow{\beta C(\phi)Cl^+} SiCl_{4(g)} + 4*$	Ion-enhanced etching

As measured by XPS of surface after etching by Cl_2 plasma, the extent of chlorination on the surface does not change noticeably with the addition of $SiCl_4$ in the feed gas. If the deposited $SiCl_x$ are treated the same as the silicon originally in the substrate and Cl adsorbed on the top surface, we would expect that the etching rate is simply reduced by the deposition. Therefore, the net etching rate is expressed as:

$$ER = ER_{wo} - DR_{total} \tag{5-5}$$

where ER is the net etching rate, ER_{wo} is the etching rate without $SiCl_4$, and DR_{total} is the deposition rate of the Si-containing species. ER_{wo} is proportional to the ion flux and surface chlorination rate. Since the surface chlorination does not change significantly, we can assume the etching yield without deposition (EY_{wo}), defined as

$$EY_{wo} = \frac{ER_{wo}}{\Gamma_i} \tag{5-6}$$

is only a function of ion energy. Therefore, the etching yield with $SiCl_4$ addition is simply

$$EY = \frac{ER}{\Gamma_i} = EY_{wo} - \frac{DR_{total}}{\Gamma_i} \tag{5-7}$$

At higher concentration of $SiCl_4$, active sites are saturated with Si-containing species and ion-enhanced deposition is almost constant. Equation (5-7) can be approximated as:

$$EY = EY_{wo} - Y_i - \frac{\Gamma_{SiClx}}{\Gamma_i} S'_{SiClx} \qquad (5\text{-}8)$$

Therefore, we can calculate Y_i and S'_{SiClx} from the intercept and slope by a linear regression of EY versus $\frac{\Gamma_{SiClx}}{\Gamma_i}$ at higher concentration of $SiCl_4$. The S_{SiClx} can be obtained by regression of EY versus $\frac{\Gamma_{SiClx}}{\Gamma_i}$ at lower $SiCl_4$ concentration. The model predictions to the experimental data are shown as lines in Figure 5-6 and 5-7. The values of the parameters at various temperatures are shown in Table 5-2.

Table 5-2. Model parameters for $SiCl_x$ deposition kinetics

	T (°C)	Y_i	S_{SiClx}	S'_{SiClx}
$SiCl_x$ Deposition	-20	0.94	0.51	0.0229
	0	0.93	0.46	0.0145
	30	0.90	0.4	0.0081

Obviously, Y_i and S_{SiClx} does not change significantly with temperature, while S'_{SiClx} is sensitive to the temperature change. Y_i seems to be a small number. But it is the average number of active sites created by ion bombardment that are available for Si-containing species deposition. Since the surface is saturated with Cl atoms, only a small fraction of bonds broken by ion bombardment is suitable for Si-containing species to be bonded to. Therefore, Y_i tends to be much smaller than the average number of bonds by an incoming ion. S_{SiClx} is the sticking probability of Si-containing species on an active site, and is mainly determined by which end of the linear molecule arrives at the surface first. Therefore it is close to 0.5, and does not change with temperature. Chae *et. al.* observed three times difference of sticking probability on active sites and on nonactive sites in fluorocarbon deposition.[9] In Si-containing species deposition, S'_{SiClx} is much smaller than S_{SiClx}, probably because $SiCl_x$ species has to compete with Cl atoms for the nonactive sites and the surface is saturated with Cl, therefore only a small fraction of nonactive sites are available for Si

containing species. S'_{SiClx} is quite sensitive to temperature change, and the corresponding activation energy can be calculated as –0.13 eV. Limb measured apparent activation energy of –0.12 eV in fluorocarbon deposition with pulsed capacitively coupled plasma, which is close to Si-containing species deposition on poly-silicon surface.[11] The agreement is probably fortuitous considering the difference between the fluorocarbon deposition and Si-containing species deposition and the simplifications we made in our kinetics model.

5.2.5. Implication of the kinetics model

Often observed in a real commercial high density plasma etcher is the dependence of etching rate on the gas flow rate. When the flow rate increase, the etching rate also increases. This has been attributed to the deposition of etching product onto the sample. Since the deposited layer has to be repeatedly removed, the etching rate is reduced. By increasing the gas flow rate, we can decrease the concentration of etching product in the etcher, therefore reducing the deposition effect.

Under typical operating condition, the etching rate can be reduced by 10 – 20%. What seems to be difficult to explain with this deposition mechanism is the fact that we typically don't see much deposition onto the feature sidewall, i.e. sidewall narrowing in. If we attribute 10 – 20% etching rate reduction to the etching product deposition, why don't we see this much deposition onto the feature sidewall?

This seemingly contradiction can be explained by our ion enhanced deposition model. In a real commercial etcher, the ions are highly directional, therefore, the ion flux to the feature bottom is much higher than to the feature sidewall. Higher ion flux results in more damaged sites, thus higher ion enhanced deposition. Therefore, the deposition rate on the feature bottom is much higher than on the feature bottom.

On the other hand, with less ion flux on the feature sidewall, the deposition on the nonactive site becomes important. Therefore, the deposition on the feature sidewall is temperature sensitive. By lowering the sample temperature, the deposition on the sidewall can increase, therefore compete with the lateral etching to avoid undercutting. This explains that by lowering sample temperature, we sometimes obtain a more straight feature sidewall.

5.3. Conclusions

The effect of oxygen addition on the etching rate of poly-silicon was measured with the plasma beam/QCM apparatus. The etching rate has a different sensitivity to the oxygen addition with different surface composition. When the surface is chlorine rich, for example, poly-silicon with exposure to Cl_2 plasma, the etching rate is not sensitive to small amount of oxygen addition. When the surface is oxygen rich, for example, silicon oxide with exposure to Cl_2 plasma, the etching rate is more sensitive to oxygen addition. This explains that in a real commercial etcher, by adding small amount of oxygen, the poly-silicon etching rate does not change much, but the silicon oxide etching rate decreases significantly, therefore the etching selectivity can be achieved.

The etching yield by the Cl_2 plasma beam is significantly affected by the $SiCl_4$ addition. The deposition of Si-containing species reduces the etching yield. The etching yield decreases drastically due to the ion-enhanced deposition of Si-containing species as the concentration of $SiCl_4$ is low. As the active sites created by ion bombardment are filled with $SiCl_x$, further reduction of etching yield is due to the chemisorbtion on nonactive sites, which is much slower than ion-enhanced deposition but more temperature sensitive. The surface halogen coverage after etching by Cl_2 with $SiCl_4$ addition is essentially the same as without $SiCl_4$ addition. A kinetics model has been developed to account for the effect of both ion-enhanced deposition and chemisorbtion on nonactive sites mechanism. The model represent the experimental data quantitatively well. This model can also explain the observed difference of feature profile under different temperatures.

5.4. References

1. C. C. Cheng, K. V. Guinn, V. M. Donnelly, and I. P. Herman, *J. Vac. Sci. Technol. A* **12**, 2630 (1994).

2. Lee C., D. B. Graves and M. A. Lieberman, *Plasma Chem. and Plasma Proc.* **16**, 99 (1996).

3. K. Tsujimoto, T. Kumihashi, and S. Tachi, *Appl. Phys. Lett.* **63**, 1915 (1993).

4. D. C. Gray, V. Homindra, and H. H. Sawin, *J. Vac. Sci. Technol. A* **12**, 354 (1994).

5. T. J. Dalton, and H. H. Sawin, presentation at the 41st Symposium of the American Vacuum Society, Denver, Colorado, 1994.

6. P. Sigmund, in *Sputtering by Ion Bombardment I*, Vol. 47 of *Topics in Applied Physics*, edited by R. Behrisch, 9.

7. L. J. Whitman, S. A. Joyce, J. A. Yarmoff, F. R. McFeely, and L. J. Terminello, *Surf. Sci.* **232**, 297 (1990).

8. A. J. Bariya, C. W. Frank, and J. P. McVittie, *J. Electrochem. Soc.* **137**, 2575 (1990).

9. H. Chae, S. A. Vitale, and H. H. Sawin, *J. Vac. Sci. Technol. A* **21**, 381 (2003).

10. J. P. Chang, A. P. Mahorowala, and H. H. Sawin, *J. Vac. Sci. Technol. A* **16**, 217 (1998).

11. S. J. Limb, Ph.D. Thesis, Massachusetts Institute of Technology (1997).

Chapter 6. Feature Profile Simulation of Poly-silicon Etching

As feature dimensions continue to shrink, a thorough understanding of the fundamental mechanisms that determine etching anisotropy is required to facilitate better process modeling, the next generation equipment design, and process development. Low pressure, high-density plasma sources, such as inductively coupled plasma, are favored in the integrated circuit manufacturing due to the increased control offered. The lower pressure (10 to 50 mTorr) reduces collisions in the plasma sheath, improving the ion bombardment directionality. Additionally, high-density plasma sources allow for greater linewidth and selectivity control by offering the ability to independently control the ion flux and ion energy by varying the power to the plasma source and wafer chunk. Therefore, both directional etching and reasonable selectivity are possible.[1] Maintaining high etching rates and reducing device damage is required to make the etching process economically viable. Etching feature profile and critical dimension control becomes increasingly important to the success of a deep-submicron etching process; therefore, its simulation and prediction are of great value.

It is important to be able to simulate the plasma etching processes because the large number of independent processing parameters makes purely empirical studies tedious and time consuming. Furthermore, empirical studies do not provide a basis for understanding the etching rates, etching profiles, selectivity, and process latitudes that are observed in plasma etching processes. To date, simulation work has given invaluable insight into the surface profile evolution during ion-enhanced plasma etching, using various techniques such as string algorithm[2], characteristics method[3], shock-tracing method[4], and direct simulation Monte Carlo[5] (DSMC) method. Dominant reaction mechanisms incorporated in these simulators include ion induced etching and ion reflection. Commonly observed etching peculiarities in plasma etching processes such as bowing, tapering, undercutting and microtrenching are predicted as different physical or chemical mechanisms are incorporated. But there is little side-by-side comparison between simulated results and observed feature profiles. We use Monte Carlo method associated with the kinetic model from beam studies to simulate feature profile evolution under different processing conditions and relate etching artifacts observed in the simulation to neutral and ion flux distribution, ion angular dependent etching yield, and surface coverage.

6.1. Monte Carlo simulation

6.1.1. Simulations and the Monte Carlo methods

Simulation has long been an important tool of designers, whether they are simulating a telephone communication system, a large-scale military battle, or a micro-reactor. Naylor et. al. define simulation as follows:[6]

> Simulation is a numerical technique for conducting experiments on a digital computer, which involves certain types of mathematical and logical models that describe the behavior of business or economic system (or some component thereof) over extended periods of real time.

Simulation, or *stochastic simulation*, is also defined as experimenting with the model over time; it includes sampling stochastic variables from certain probability distribution. Because sampling from a particular distribution involves the use of random numbers, stochastic simulation is sometimes called *Monte Carlo simulation*. Random numbers are essentially independent random variables uniformly distributed over the unit interval [0, 1]. The term "Monte Carlo" was introduced by von Neumann and Ulam during World War II as a code word for the secret work at Los Alamos; it was suggested by the gambling casinos at the city of Monte Carlo in Monaco. The Monte Carlo method was then applied to problems related to the atomic bomb. The work involved direct simulation of behavior concerned with random neutron diffusion in fissionable material. Shortly thereafter Monte Carlo methods were used to evaluate complex multidimensional integrals and to solve certain integral equations occurring in physics, which were not amenable to analytic solution.

6.1.2. Random variable generation

In this section, we consider some procedures for generating random variables from different distributions. These procedures are based on the following three methods: inverse transform method, composition method, and acceptance-rejection method.

Inverse transform method

Let X be a random variable with cumulative probability distribution function $F_X(x)$. Since $F_X(x)$ is a nondecreasing function, the inverse function $F_X^{-1}(y)$ may be defined for any value of y between 0 and 1 as $F_X^{-1}(y)$ is the smallest x satisfying $F_X(x) \geq y$, that is,

$$F_X^{-1}(y) = \inf\{x : F_X(x) \geq y\}, \quad 0 \leq y \leq 1. \tag{6-1}$$

It's easily proved that if U is uniformly distributed over the interval (0,1), then

$$X = F_X^{-1}(U) \tag{6-2}$$

has cumulative distribution function $F_X(x)$.

Composition method

This method is employed by Butler.[7] In this technique $f_X(x)$, the probability distribution function of the distribution to be simulated, is expressed as a probability mixture of properly selected density functions. Mathematically, let $g(x|y)$ be a family of one-parameter identifying a unique $g(x)$. If a value of y is drawn from a continuous cumulative function $F_Y(y)$ and then if X is sampled from the $g(x)$ for that chosen y, the density function for X will be

$$f_X(x) = \int g(x \mid y) dF_Y(y) \tag{6-3}$$

By using this technique some important distributions can be generated. This technique may be applied for generating complex distributions from simpler distributions that are themselves easily generated by the inverse transform technique or by the acceptance-rejection technique.

Acceptance - rejection method

This method is due to von Neumann[8] and consists of sampling a random variable from an appropriate distribution and subjecting it to a test to determine whether or not it will be acceptable for use.

Let X to be generated from $f_X(x)$. To carry out the method we represent $f_X(x)$ as

$$f_X(x) = Ch(x)g(x) \tag{6-4}$$

where $C \geq 1$, $h(x)$ is also a probability distribution function, and $0<g(x) \leq 1$. Then we generate two random variables U and Y from $U(0,1)$ and $h(y)$, respectively, and test to see whether or not the inequality $U \leq g(Y)$ holds:

1. If the inequality holds, then accept Y as a variable generated from $f_X(x)$.
2. If the inequality is violated, reject the pair. U, Y and try again.

6.2. Monte Carlo simulation for feature profile evolution

The Monte Carlo technique associated with two-dimensional feature representation and surface kinetics is used to simulate the profile evolution. The third dimension was "folded in", i.e. the computed fluxes were those that would fall on a line-and-space pattern. Processes with angular dependence such as ion enhanced chemical etching used the third dimension velocity component to correctly compute the incident angles.

The model employed in this study has been previously described and so will be only briefly discussed here.[9,10]

6.2.1. Monte Carlo model description

The calculation domain is discretized into a square cellular array with 25 Å sides, a dimension comparable to the characteristic length for compositional changes in ion induced processes; e.g., the surface halogenation layer depth caused during ion induced etching processes.

The Monte Carlo simulation is a probabilistic numerical approach in which many (millions) of typical particle trajectories are generated that provide a sufficiently large sample to predict the behavior of the real system. Since intermolecular collisions may be neglected due to the low chamber pressures involved, these trajectories are independent of each other and may be generated serially (at 10 mTorr, the mean free path of molecules is about 1 cm. The feature dimension is of the order of 1 μm. Therefore, only about 0.01% of the molecules undergo collisions with another molecule in the simulation domain.).

Reactant species were introduced at a source plane above the top of the feature. The initial lateral position of the particle was selected randomly along the source plane. Each particle's trajectory was determined by randomly sampling from their respective distribution functions – cosine distribution for neutrals and Gaussian angular distributions for ions.

After determining the particle's origin and trajectory, it was stepped one cell length at a time until it reached a surface cell. Reflection of the particles at the simulation domain's left and right boundaries provided symmetric boundary conditions. A particle that crossed either boundary was reflected specularly at the boundary and retained in the simulation domain. Scattered particles and product species that crossed the source plane from below were eliminated from the simulation.

When a particle strikes the surface, the surface kinetics model was used to probabilistically determine the fortune of the particle. If the particle was adsorbed onto the surface, the surface composition needs to be updated. Otherwise, if the particle was scattered back into gas phase, its trajectories needs to be tracked until it strikes another surface. This computation process is recursively repeated until the particle escapes the feature from the gap between neighboring lines.

(1) Scattering mechanism:

A particle that did not react with the surface was scattered. To properly determine the scattering angle, the surface normal was determined by least square fitting of the adjacent surface cells on either side and including the cell of impact. In a scattering event, a neutral particle scattered non-specularly, i.e. it is re-emitted from the surface after thermally equilibrated with the surface, and bears a cosine distribution. An ion underwent specular scattering in which the ion scatter angle was identical to the ion incident angle. The third velocity component of the ions was also used in calculating the ion incident and scattering angles. After scattering, an ion was assumed to retain all its initial energy.

(2) Surface reaction:

The surface reaction probabilities were determined by the kinetic models proposed in section , depending on the type of ions and materials included. The reaction probability of

ions was calculated based on the measured ion angular dependence, and the sticking probability of chlorine and bromine was determined based on the extent of surface halogenation.

Elemental balances were performed in surface cells every time a reactant particle reacted with a surface cell. The individual counters for the various types of particles present in the cell were updated. Each cell initially contained N particles; and the cell could either add more particles (deposition) till it reached a total of 2N or lose particles (etching) till it contained only N/6 particles. When a limit was reached, the cell of interest either deposited another cell or was etched; the surface was then redefined. The deposited cell was half the contents of the parent cell while the etched cell passed its residual contents to a neighboring cell based on per-determined rules.

6.2.2. Estimation of ion energy from top power and bias power

For low pressure, high-density plasma sources, such as inductively coupled plasma, the ion flux and ion energy can be independently controlled by varying the inductive power to the plasma source and wafer chunk bias power. A simple model is utilized to determine the mean ion energy according to inductive power and bias power. The ion flux is estimated as

$$I^{+} = \frac{W_{induct}}{E_{ion,created}} \qquad (6\text{-}5)$$

where W_{induct} is the inductive power, and $E_{ion,created}$ is the average energy needed to create an ion. In our simulation, $E_{ion,created}$ is 100 eV.

So the ion energy after acceleration by bias power is

$$E_{Ion} = \frac{W_{Bias}}{I^{+}} + E_{self-bias} \qquad (6\text{-}6)$$

where W_{Bias} is the bias power, and $E_{self-bias}$ is the self-bias energy of ion. 20 eV is used for $E_{self-bias}$ in our simulation.

6.2.3. Neutral and ion distribution functions

Before entering the feature area, the ionic and neutral species have very different angular distributions. The ions accelerated by the plasma sheath are directional while the neutral flux is isotropic. The neutrals entering the simulation domain are sampled from an isotropic distribution giving a cosine flux distribution at a planar surface. The angular distribution of a sample of neutral particles is shown in Figure 6-1.

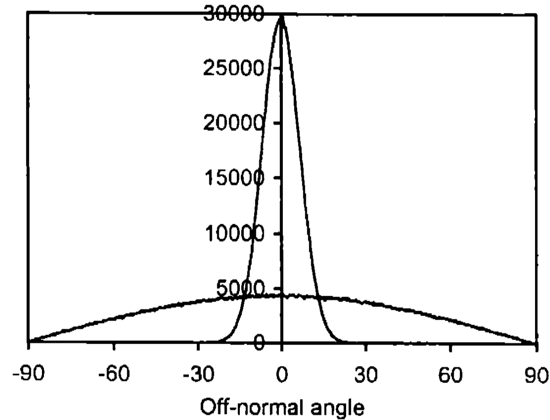

Figure 6-1: The angular distribution of neutral and ion species. The total number for each species is 500000. While the neutrals are sampled from an isotropic distribution giving a cosine flux distribution at a planar surface, the ions are sampled from Gaussian distribution and is characterized by its standard deviation, σ. In this figure, the standard deviation for ions is 0.075.

The ions are sampled from an anisotropic angular distribution. The ion angular distribution is Gaussian and is characterized by its standard deviation, σ.

$$N(\theta) = \frac{N_0}{\sqrt{2\pi}\sigma}\exp(-\frac{\theta^2}{2\sigma^2}) \qquad (6\text{-}7)$$

where, θ is the off-normal angle. The angular distribution for ions with σ of 0.075 is also shown in Figure 6-1. The standard deviation, σ, is related to the ion energy. To simplify, the sheath was assumed to be collisionless. The off-normal angle of an ion, at angle θ_1 with energy E_1 before bias acceleration, would become θ_2, and its energy would become E_2 as well.

$$\sqrt{E_1}\sin\theta_1 = \sqrt{E_2}\sin\theta_2 \qquad (6\text{-}8)$$

For small angle, $\sin\theta \approx \theta$, so

$$\sqrt{E_1}\theta_1 = \sqrt{E_2}\theta_2 \tag{6-9}$$

The angular distributions before and after the acceleration are characterized respectively by

$$N_1(\theta_1) = \frac{N_0}{\sqrt{2\pi}\sigma_1}\exp(-\frac{\theta_1^2}{2\sigma_1^2}) \tag{6-10}$$

$$N_2(\theta_2) = \frac{N_0}{\sqrt{2\pi}\sigma_2}\exp(-\frac{\theta_2^2}{2\sigma_2^2}) \tag{6-11}$$

While the change in distribution with acceleration is given by

$$N_1(\theta_1)d\theta_1 = N_2(\theta_2)d\theta_2 \tag{6-12}$$

Differentiating Eqn. 7 and combining with Eqn. 10 yields

$$\frac{\sigma_2}{\sigma_1} = \sqrt{\frac{E_1}{E_2}} \tag{6-13}$$

Therefore the angular distribution of the ions varies inversely with the square root of the sheath potential drop.

6.2.4. Estimate of neutral-to-ion flux ratio

The etching reaction is started with the surface chlorination, thus the etching rate, as well as the feature profile is dependent on the extent of chlorination. For 1 mTorr Cl_2 at 20°C with 50% dissociation, the neutral flux is 2.4×10^{17} #/cm²s. In typical low pressure, high-density plasma etching, the pressure of 2~10 mTorr is used, so the neutral flux is about 10^{18} #/cm²/s. The ion flux is about 5 mA/cm², which is corresponding to 3×10^{16} #/cm²/s. Therefore, the neutral-to-ion ratio is around 33:1, depending on the specific processing conditions, which is in the same range as our simulation.

6.3. Generalized kinetics model

The Monte Carlo algorithm permitted the incorporation of all the dominant physics and chemistry of the plasma etching process by using kinetically based probabilities for each surface process and performing an elemental balance on a surface cell each time it interacted with a reactant species particle. A phenomenological model that accounts for the energy, flux and angular dependencies of Cl^+ ion-enhanced polysilicon etching with Cl is constructed for profile simulation.[11,12] Since many reaction mechanisms occur simultaneously and are

convoluted, a simplified model is proposed to represent the overall kinetics and is represented in Table 6-1.

TABLE 6-1. The simplified phenomenological surface kinetics model for Cl^+ ion enhanced poly-silicon etching with Cl.

Simplified kinetics model	Mechanism
$Cl_{(g)} + * \xrightarrow{s} Cl_{(s)}$	Sorption of atomic chlorine $s = 0.066\left(\sqrt{E_{Ion}} - \sqrt{E_{threshold,Sorption}}\right)$
$Cl^+_{(g)} + * \xrightarrow{\alpha} Cl_{(s)}$	Sorption of ionic chlorine
$SiCl_{2(g)} \xrightarrow{\delta} Si_{(s)} + 2Cl_{(s)}$	Deposition of by-product, $\delta = 0.5$
$Si_{(s)} + Cl^+ \xrightarrow{f_{Phy}(\phi) g_{Phy}(E_{Ion})} Si_{(g)} + Cl_{(s)}$	Sputtering $f_{Phy}(E) = 0.04(\sqrt{E} - \sqrt{E_{threshold,Phy}})$
$Si_{(s)} + 4Cl_{(s)} \xrightarrow{f_{Che}(\phi) g_{Che}(E_{Ion}) Cl^+} SiCl_{4(g)} + 4*$	Ion-enhanced etching $f_{Che}(E) = 0.6(\sqrt{E} - \sqrt{E_{threshold,Che}}) - 0.46$

The generalized chemistry model consolidates all the etching yields and angular dependence information. In general, the etching yield for both sputtering and ion induced chemical reaction is a function of the ion energy $f(E)$, the ion incidence angle $g(\phi)$, and halogen coverage on the surface $h(\theta_{Cl})$. Ignoring interactions of these three factors, the etching yield can be expressed as

$$Y_i(E,\phi,\theta_{Cl}) = f_i(E) g_i(\phi) h_i(\theta_{Cl}) \quad (6\text{-}14)$$

where subscript i represents a different reaction mechanism, including physical sputtering and ion induced chemical reaction.

When a Cl^+ ion strikes a surface cell, a yield-coverage (E-θ) weighted angular dependence factor (α) is calculated, which is between 0 and 1 (since the angular curves for all processes are normalized to unity)

$$\alpha = \frac{f_{Phy}(E) g_{Phy}(\phi) + f_{Che}(E) g_{Che}(\phi) \theta_{Cl}}{f_{Phy}(E) + f_{Che}(E) \theta_{Cl}} \quad (6\text{-}15)$$

The probability of the ion being consumed is identical to this calculated value (α) and therefore the scattering probability is (1-α).

If the ion is consumed at the surface, the etching yields of all the possible products computed previously were used in determining the product distribution leaving the surface. The trajectory of each product is tracked until it escapes from the feature. If not consumed, the ion is assumed to scatter specularly and its trajectory is tracked.

6.4. Simulation results

Lane, *et. al.* did extensive experimental studies on polysilicon etching with chlorine in inductively coupled plasma etcher.[13] We utilize their results here to compare with our simulation. In their experiments, SiO_2 – masked samples were fabricated from 5000Å thick SiO_2 films deposited by plasma enhanced chemical vapor deposition (CVD) patterned in CHF_3/SF_6 plasmas using photoresist masks. The mask forms an angle of 83° with respect to the surface normal. This angle is constant across feature size and spacing.

6.4.1. Etching rates and aspect ratio dependent etching (ARDE)

The aspect ratio of a feature is defined as the ratio of the depth of a feature to its width: d_{main}/w. Figure 6-2 shows the definition of d_{main} and some of often observed etching artifacts. Figure 6-3 shows the dependence of etching rate on aspect ratio obtained from the simulation. Consistent with experimental results[13], no significant ARDE was observed, which suggests that the geometric shadowing of neutrals and ions, either at the feature center or side, does not play a significant role under these plasma conditions. Figure 6-4 shows the profile evolutions with different aspect ratio.

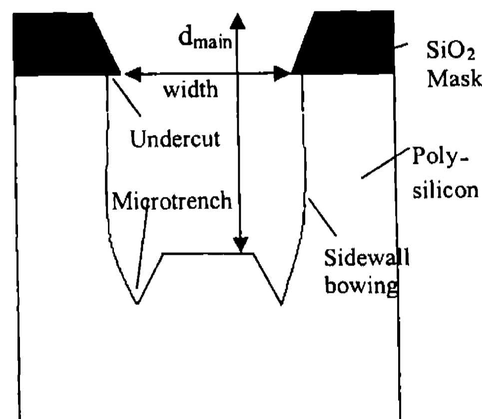

Figure 6-2: Common artifacts observed during plasma etching. The artifacts often observed during poly-silicon etching include: undercutting, sidewall bowing and microtrench.

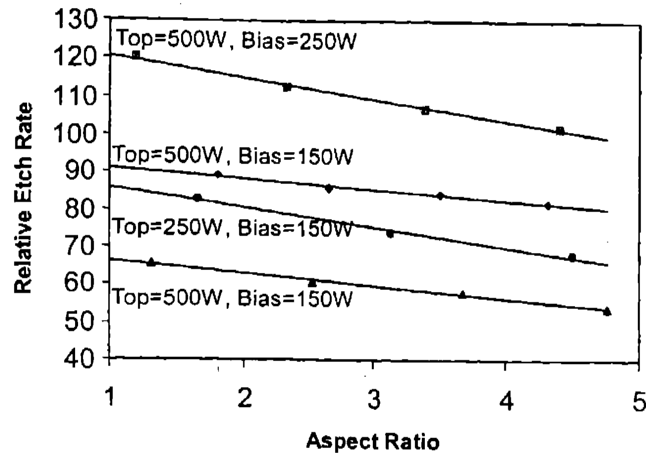

Figure 6-3: Simulation results for etch rate vs. aspect ratio under various top powers and bias powers. Other conditions are: $Cl:Cl^+:SiCl_2$=100:10:0, $\sigma_{ion} \propto E_{ion}^{-1/2}$. No significant ARDE was observed. This suggests that the geometric shadowing of neutrals and ions, either at the feature center or side, does not play a significant role under these plasma conditions.

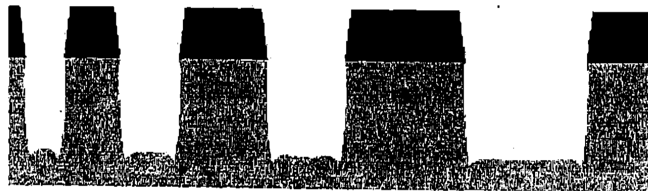

Figure 6-4: Simulated profile evolutions for different aspect ratio. The simulation conditions are: Ion energy=50eV, σ_{ion}=0.075, $Cl:Cl^+:SiCl_2$=100:10:0.

6.4.2. Feature profile analysis

Sidewall bowing

Bowing refers to the curvature of the sidewalls. Bowing can be caused by a variety of factors, e.g. non-directional ions, smaller etching yields for off-normal ions and sidewall deposition. Sidewall bowing affects the critical dimension of the feature and can cause microtrenching at the feature bottom.

Feature bottom microtrenching

Microtrenching is the enhanced etching at the foot of an etched sidewall, leading to the "molar" or "fang" shape. Typically, it is caused by the increased flux of ions at the trenches due to reflection from tapered/bowed sidewalls or possibly bending of ion trajectories because of charging effects. Microtrenching is undesirable during the poly-silicon etching step because the thin gate oxide can break through with ion flux at the microtrench locations damaging the MOS transistor.

Experimentally, microtrenching at the bottom of oxide-masked samples in a Cl_2 chemistry was not observed during the initial stages of the etching process. Microtrenching began midway during the etching process. Microtrenching was more severe for the narrower features as compared to the wider features.

Microtrenching has been shown to be caused in part by ion scattering from an inclined sidewall of the feature.[14] The absence of a tapered sidewall close to the feature bottom or bowed sidewalls is thought to be responsible for the absence of microtrenching initially since the relatively vertical sidewall minimizes the number of scattered ions and disperses the scattered ions rather than concentrating them at the feature bottom, while the mechanism for forming microtrenches is the scattering from a curved sidewall causing a focusing of the ions on the microtrench. Both cases are shown in Figure 6-5.

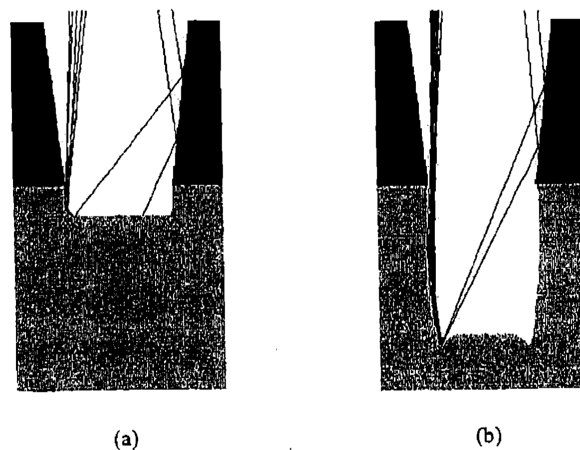

Figure 6-5: The mechanism of microtrenching forming. Microtrenching is partly due to the ion scattering from an inclined sidewall of the feature. The absence of a tapered or bowed sidewall is thought to be responsible for the absence of microtrenching initially.

(a). The initial stage, little amount of ions are focused at the foot .
(b). The final stage, large amount of ions are focused at the microtrenching region.

Two different feature profiles, shown in Figure 6-6, are studied. A large number of ions (10^6) are introduced into the simulation domain and their trajectories are tracked. Whenever an ion is determined to be able to etch a cell, it is eliminated from the simulation domain and we move to the next ion. By this way, we can do some statistic analysis while keeping the profile unchanged.

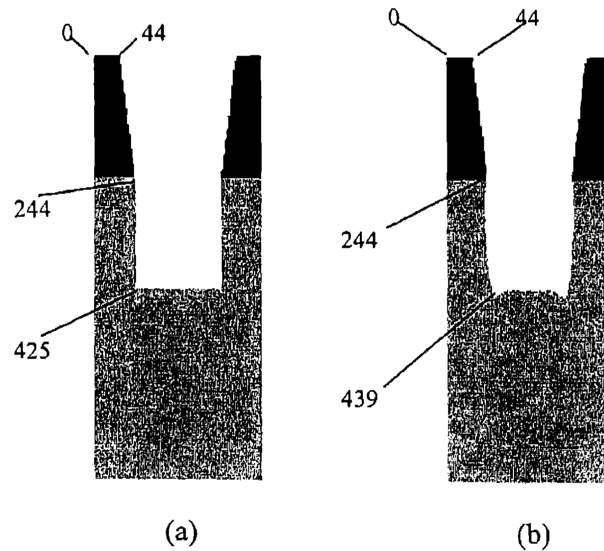

Figure 6-6: Two kind of profiles are studied for microtrenching mechanism: (a). Vertical sidewall. (b). Bowed sidewall. The numbers in the figure signify the location of cells in the interface curve.

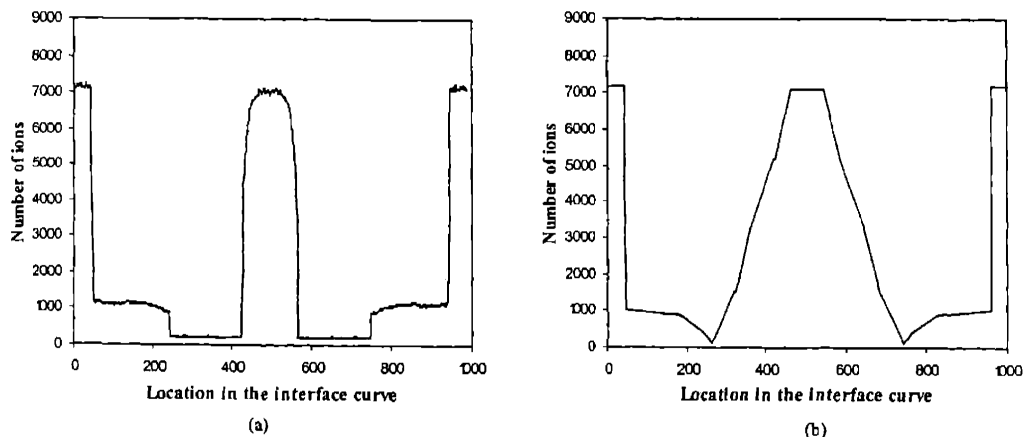

Figure 6-7: The number of ions which fell into the interface cells for the first time, not including those scattered from other surfaces. (a) For the vertical sidewall case, as shown in Figure 6-6(a). (b) For the bowed sidewall case, as shown in Figure 6-6(b).

The number of ions that impacted the interface cells for the first time is counted and shown in Figure 6-7 for both cases. These figures indicate that the number of ions impacting the interface cells for the first time does not differ significantly from each other except that a great number of ions impacted the bowed sidewall than the vertical sidewall.

The number of ions that impacted and stuck to the interface cell is counted as well and shown in Figure 6-8 for both cases respectively. When determining whether an ion should stick to the interface cell or scatter, the ion energy, the ion impact angle and the surface chlorination were taken into account. Therefore, the number of ions stuck to the interface cell is proportional to the etching rate at the location.

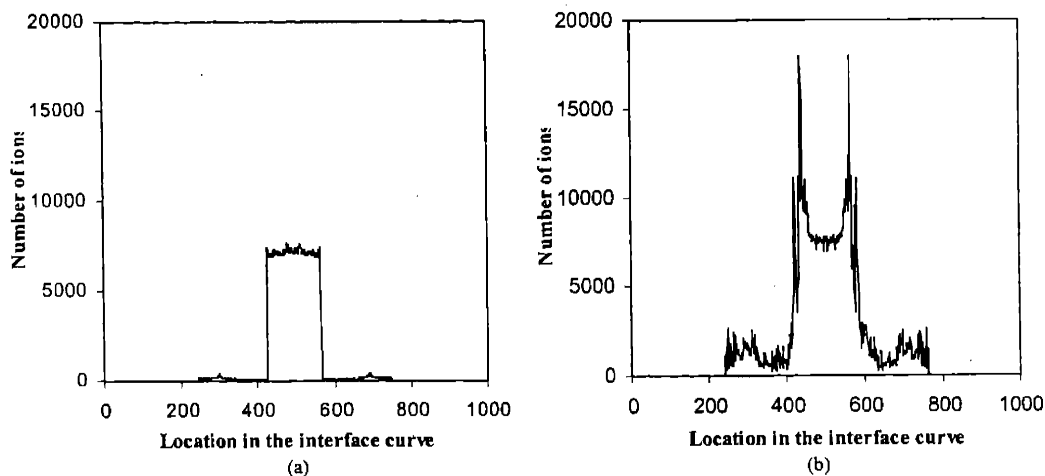

Figure 6-8: The number of ions which fell into and were stick to the interface cell. When determining whether an ion should be stick to the interface cell or scattered, the ion energy, the ion impact angle and the surface chlorination were taken into account. Therefore, the number of ions which were stick to the interface cell is proportional to the etching rate in that cell.
(a) For the vertical sidewall case, as shown in Figure.6-6(a).
(b) For the bowed sidewall case, as shown in Figure 6-6(b).

In Figure 6-8, the reflection from the bowed sidewall shows that the ions are focused in the microtrenching region, which significantly increases the etching. With vertical sidewall, almost no ions are focused at the foot of sidewall, thus no microtrenching happens. It was observed that many more ions strike the bowed sidewall than in vertical sidewall. This is in part due to greater surface roughness that specularly scatters the ions more broadly. The increased surface roughness was observed in this simulation for the bowed sidewall.

Undercutting

Undercutting refers to the lateral etching into a layer and can be considered as extreme sidewall bowing. Typically, undercutting occurs at the interface of two materials when one material is resistant to the etching species, e.g. immediately below an etch-resistant oxide mask. From Figure 6-4, we observe undercutting of the oxide mask at narrower feature widths, which is consistent with experimental results. This undercutting has been attributed to the ion scattering off the neighboring hardmask.[15,16] Ion scattering off the hardmask at a constant angle would impact the sidewall of a neighboring feature. As the feature width shrinks, the ions impact higher on the neighboring sidewall, causing the observed undercutting. Not included in this simulation is spontaneous etching and interface stress induced spontaneous etching which both would increase the undercutting.

6.4.3. Simulated feature profile evolution and comparison with experimental results

Feature profile evolutions under different processing conditions are discussed below. Simulated results are compared with experimental results.

Influence of neutral-to-ion ratio

The feature profile evolutions with different neutral-to-ion flux ratio are shown in Figure 6-9. The etching rates at various aspect ratios for these cases are shown in Figure 6-10. When the neutral-to-ion flux ratio is high, such as 100:1, the etching rate per ion is high, as expected. Significant ARDE is observed while the neutral-to-ion flux ratio is 100:1. The etching rate increases as the feature etches deeper, which is attributed to the narrowing of the feature at greater depth and the scattering of ions to the center by the bowed sidewalls. The ion flux at the center of bottom at different depth is shown in Figure 6-11. As we know, for ion-enhanced etching, the etching rate is also dependent on surface chlorination. The relative ion flux after considering the variation of chlorination, $I^{+}\frac{R_{Cl/Si}}{R^{0}_{Cl/Si}}$, is also shown in Figure 6-11. It is evident that the relative etching rate agrees well with the relative ion flux. No significant ARDE is observed for other cases.

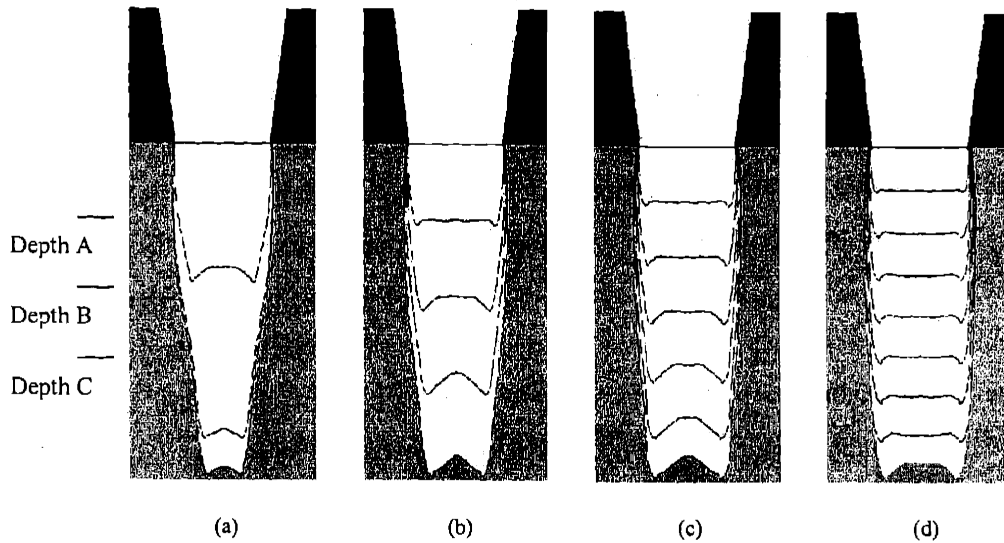

Figure 6-9: Simulated feature profile evolutions with different neutral-to-ion ratio. (a) $Cl:Cl^{+}:SiCl_2$=100:1:0, (b) $Cl:Cl^{+}:SiCl_2$=100:5:0, (c) $Cl:Cl^{+}:SiCl_2$=100:10:0, (d) $Cl:Cl^{+}:SiCl_2$=100:20:0. The other conditions are: ion energy=50eV, $\sigma_{ion} = 0.075$. The surface chlorination at depth A, B and C respectively are shown in Figure 6-12.

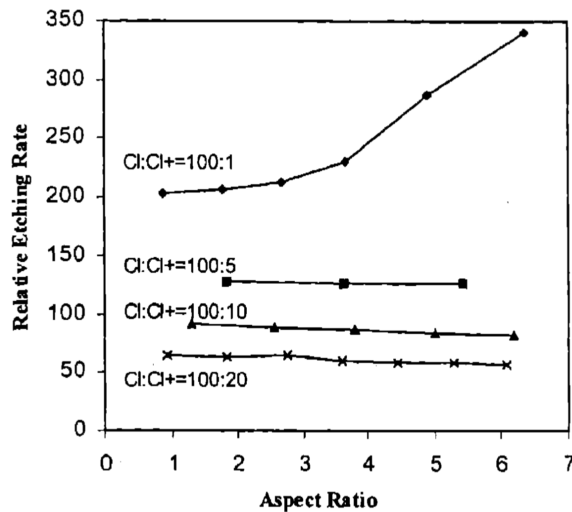

Figure 6-10: The etching rate for case shown in Figure 6-9 vs. aspect ratio. Significant ARDE is observed while $Cl:Cl^{+}$=100:1, while no significant ARDE is observed for other cases.

It is also obvious that the feature profiles are quite different from each other. With higher neutral-to-ion ratio, the feature narrows as the depth increases, while the sidewall is quite vertical. The bottom is flat with lower neutral-to-ion ratio. The variation of feature

profiles is partly due to the variation of surface chlorination. The surface chlorination for different cases at depth A, B and C is shown in Figure 6-12. The ion flux is relatively larger in the center of feature bottom due to larger view angle. So the feature profile would look like that shown in Figure 6-13 with sidewall tapered initially. For the highest neutral-to-ion ratio, the surfaces of both sidewall and bottom sidewall are almost saturated with chlorine. From the angular dependence of etching rate, we know the ion-enhanced etching peaks at 90° and goes to zero at 0°. Since the ions can only strike the sidewall surface at very small angle, the ratio of lateral etching rate to vertical etching rate, $R_{lateral}/R_{vertical}$, would be very small, and the sidewall keeps tapered, resulting in the observed profile. When the neutral-to-ion ratio becomes lower, the surface chlorination is less saturated. Since the absolute etching rate at the sidewall is still very low, it could still be saturated with chlorine. Therefore, the Cl/Si ratio is higher at sidewall than at bottom, causing the ratio, $R_{lateral}/R_{vertical}$, relatively larger and the lateral etching could catch up with vertical etching. So the sidewall is more vertical. We can even observe undercutting when the neutral-to-ion ratio is 100:20.

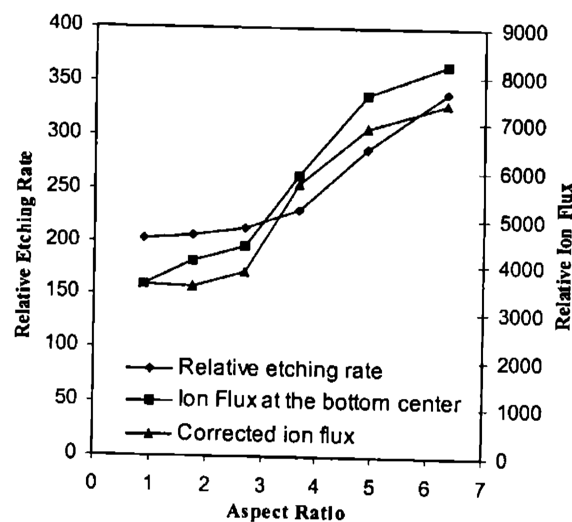

Figure 6-11: Ion flux at bottom center for case shown in Figure 6-9(a) vs. aspect ratio. For ion-enhanced etching, the etching rate is dependent on surface chlorination. After considering the variation of chlorination with aspect ratio, the corrected ion flux is also shown in this figure.

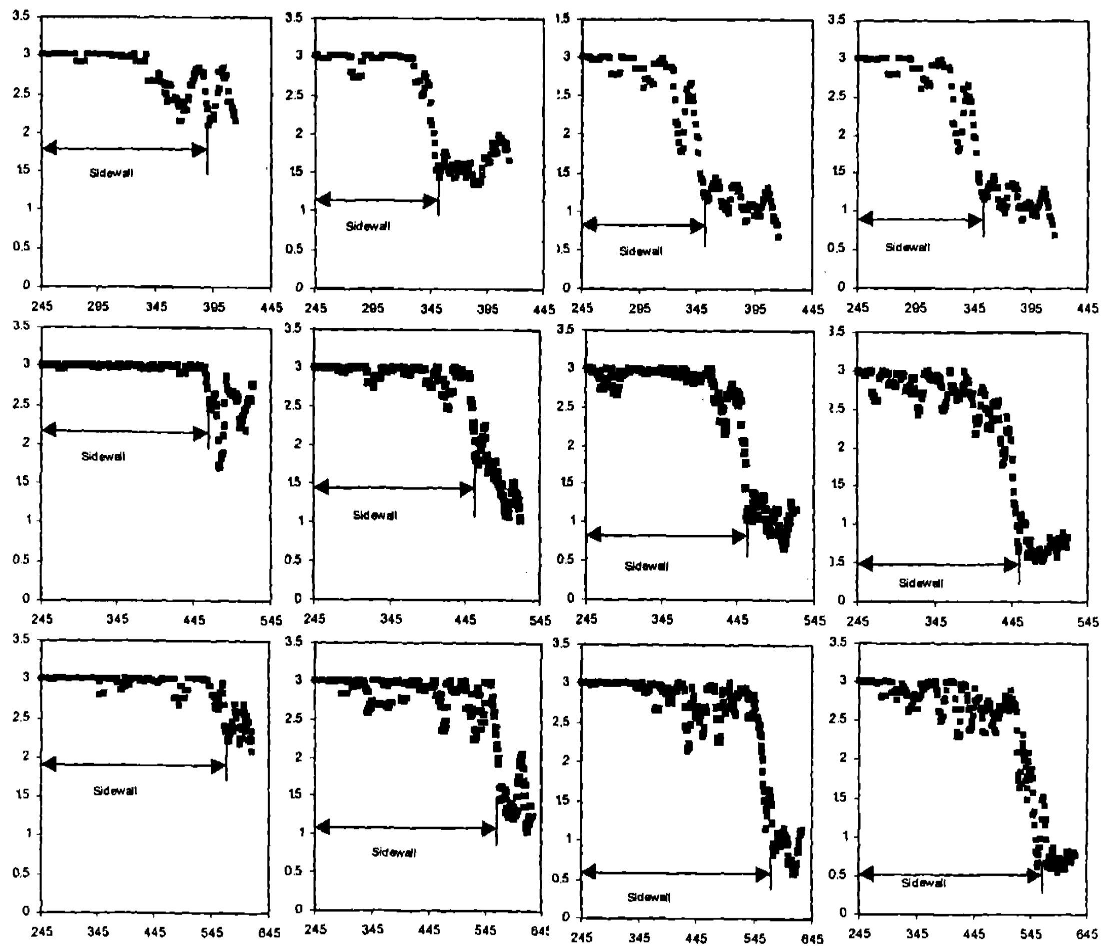

Figure 6-12: Surface chlorination for various cases shown in Figure 6-9 at depth A, B and C respectively. (a) $Cl:Cl^+=100:1$, (b) $Cl:Cl^+=100:5$, (c) $Cl:Cl^+=100:10$, (d) $Cl:Cl^+=100:1$. Since most ions strike the sidewall at very small angle, resulting in very small etching rate, the sidewall is almost saturated with chlorine. When the neutral-to-ion ratio becomes lower, the chlorination at the bottom would be less saturated.

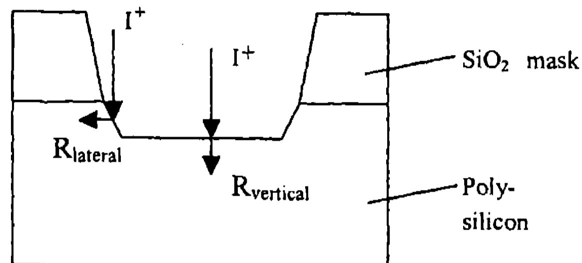

Figure 6-13: Schematic figure of feature profile evolution. The ion flux is relatively larger in the center of feature bottom due to larger view angle, resulting in the above feature profile

with sidewall tapered initially. Ions could also strike the sidewall, inducing the lateral etching. The evolution of sidewall profile would be determined by the ratio of lateral etching to vertical etching to some extent.

Experimental profiles under different pressures are shown in Figure 6-14.[13] From 2 mTorr to 10 mTorr, the feature profiles changed dramatically. The profiles under lower pressure are more ideal, with the sidewall more vertical and bottom flatter. The variation of profiles is due to the variation of species composition, with the neutral-to-ion ratio, Cl/Cl^+, smaller under lower pressure. Compared with Figure 6-9, Cl/Cl^+=100:5 and Cl/Cl^+=100:20, the experimental profiles match the simulation qualitatively. For example, the trench bottom width is 200 nm for Cl/Cl^+=100:5 and 235 nm for Cl/Cl^+=100:20, compare with 250 nm for 10 mTorr and 285 nm for 2 mTorr. Also the height of microtrenching is 75 nm for Cl/Cl^+=100:5 and 50 nm for Cl/Cl^+=100:20, compared with 105 nm for 10 mTorr and 70 nm for 2 mTorr.

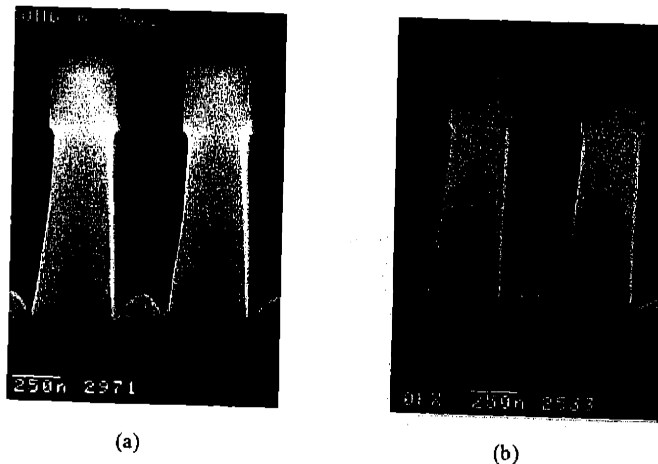

(a) (b)

Figure 6-14: Experimental cross sections of 0.35 μm nested trenches etched with 500W top power and 150W bias power at 80 sccm Cl_2, the pressures are (a) 10 mTorr; (b) 2 mTorr. Reprinted by permission from Ref. 18.

Influence of ion energy

The profile evolutions at different ion energy are shown in Figure 6-15. Increasing ion energy broadens microtrenches and flattens trench bottoms. Experimental profiles for the feature profile at different energy are shown in Figure 6-16. It can be seen that the simulated profiles agree well with experimental ones.[13]

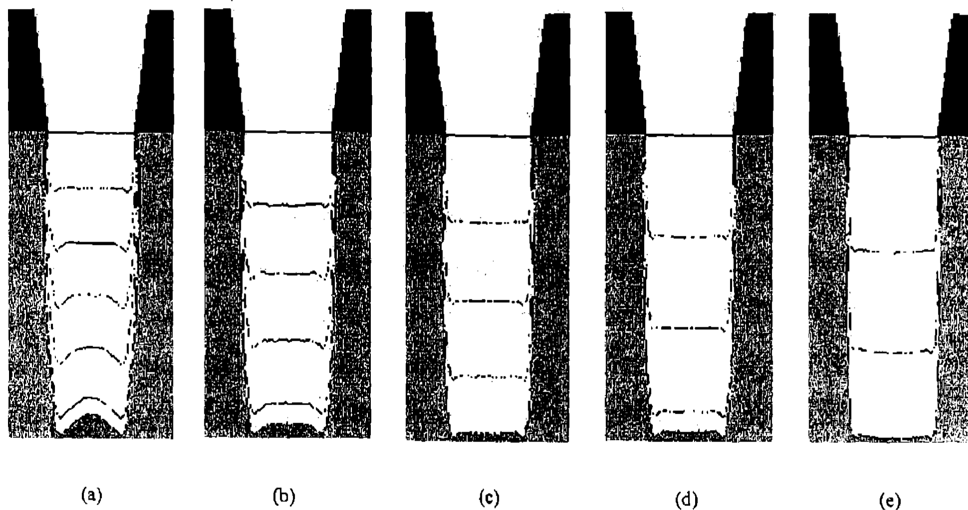

Figure 6-15: Simulated feature profile evolutions for various ion energy, (a) 50eV; (b) 70eV; (c) 90eV; (d) 120eV; (e) 160eV. The other simulation conditions are: $\sigma_{ion} \propto 1/\sqrt{E}$, Cl:$Cl^{+}$:$SiCl_2$=100:10:0.

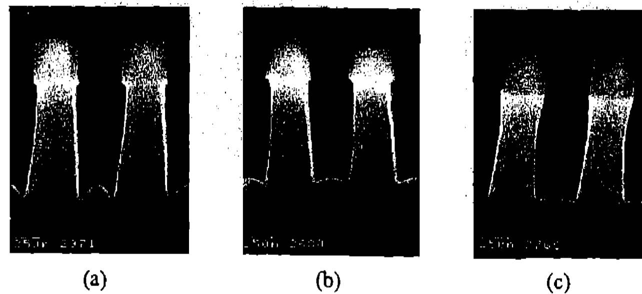

Figure 6-16: Experimental cross section of 0.35 μm nested trenches etched with 500W top power and (a) 150W; (b) 250W; (c) 350W bias power at 10 mTorr, 80 sccm Cl_2. Reprint by permission from Ref. 18.

From the above analysis, higher ion energy would result in narrower angular distribution of ions at the wafer surface. With a narrow ion angular distribution fewer ions impinge on, and are focused by, the sidewall. This results in a flatter trench bottom. The improved ion directionality, however, cannot explain the more ideal feature profile completely. Figure 6-17 shows the feature profile evolution by 50 eV ions which is given a σ_{ion} of 160 eV ions.

Compared with Figure 6-15(a), the profile in Figure 6-17(a) does not improve significantly, which indicates that the improved ion directionality is not the only reason for improved feature profile. The other possible reason is the variation of etching kinetics. According to the etching kinetics, the etching rate is proportional to the square root of ion energy, so higher ion energy would result in faster etching, and hence result in less chlorinated bottom surface. The effect is somewhat equivalent to the increase of ion-to-neutral ratio. The profile in Figure 6-17(b) is utilized to simulate this effect. We obtain almost the same profile as that etched by 160 eV ions, which proved our assumption.

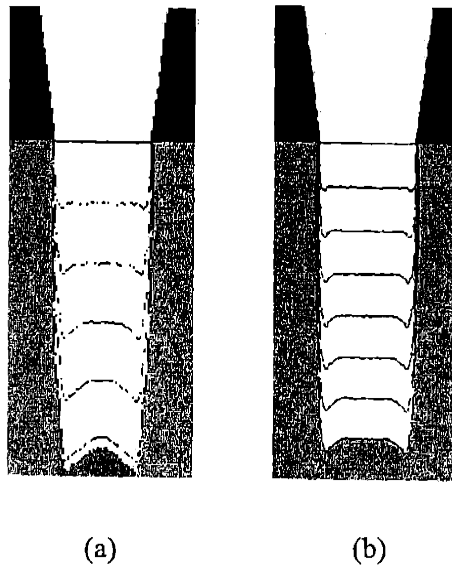

Figure 6-17: Simulated feature profile evolution for 50eV ions with an angular distribution of 160eV ions. The neutral-to-ion ratio is: (a) $Cl:Cl^{+}$=100:10, (b) $Cl:Cl^{+}$=100:20.

Influence of mask angle

As shown in Figure 6-18, mask angle influences the profile. With a more vertical mask, the bottom becomes flatter. At the initial stage, the profiles at the bottom are quite different for different mask angles. At 90°, the center of bottom etches faster, where more ions are focused due to more vertical mask. As the etching proceeds, the difference diminishes gradually, as expected. But the sidewall does not change significantly, since the possible etching mechanisms of the sidewall are non-directional ions, smaller etching yields for off-normal ions and sidewall deposition, which are almost unrelated to the mask.

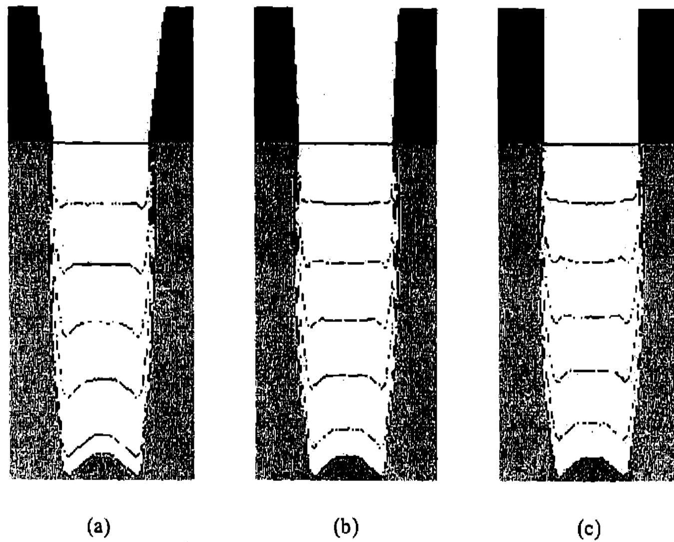

Figure 6-18: Simulated feature profile evolution for different mask angles: (a) 83°; (b) 87°; (c) 90°. The other simulation conditions are: ion energy=50eV, σ_{ion} =0.075, $Cl:Cl^{+}:SiCl_2$=100:10:0.

6.5. Conclusion

Feature profile evolution under different conditions were obtained by Monte Carlo simulation and compared. The neutral-to-ion ratio was found to result in the variation of surface chlorination, which could influence the feature profile evolution. Different ion energy would result in different etching rate and the surface chlorination, thus influence the feature profile as well. Other facts, such as the mask angle, are also found to have some effects on the feature profile by our simulation, which agree with experimental results.

6.6. References

1. J. W. Coburn, *Appl. Phys. A.: Solids Surf.* A **49**, 451 (1994).

2. J. I. F.Ulacia and J. P. McVittie, *J. Appl. Phys.* **65**, 1484 (1989).

3. E. S. G. Shaqfeh and C. W. Jurgensen, *J. Appl. Phys.* **66**, 4664 (1989).

4. S. Hamaguchi and M. Dalvie, *J. Vac. Sci. Technol. A* **12**, 2745 (1994).

5. R. N. Tait, S. K. Dew, T. Smy, and M. J. Brett, *J. Vac. Sci. Technol. A* **12**, 1085 (1994).

6. R. Y. Rubinstein, *Simulation and the Monte Carlo Method*, John Wiley & Sons (1981).

7. J. W. Butler, Machine sampling from given probability distributions, in *Symposium on Monte Carlo Methods*, edited by M. A. Meyer, Wiley, New York (1956).

8. J. von Neumann, *U. S. Nat. Bur. Stand. Appl. Math. Ser.* **12**, 36 (1951).

9. A. P. Mahorowala, H. H. Sawin, R. Jones, and A. H. Labun, *J. Vac. Sci. Technol. B* **20**, 1055 (2002).

10. A. P. Mahorowala and H. H. Sawin, *J. Vac. Sci. Technol. B* **20**, 1064 (2002).

11. J. P. Chang and H. H. Sawin, *J. Vac. Sci. Technol. A* **15**, 610 (1997).

12. J. P. Chang, A. P. Mahorowala and H. H. Sawin, *J. Vac. Sci. Technol. A* **16**, 217 (1998).

13. J. M. Lane, F. P. Klemens, K. H. A. Bogart, M. V. Malyshev, and J. T. C. Lee, *J. Vac. Sci. Technol. A* **18**, 188 (2000).

14. S. Ohki, M. Oda, H. Akiya, and T. Shibata, *J. Vac. Sci. Technol. B* **5**, 1611 (1987).

15. T. J. Dalton, J. C. Arnold, H. H. Sawin, S. Swan, and D. Corliss, *J. Electrochem. Soc.* **140**, 2395 (1993).

16. G. S. Hwang, C. M. Anderson, M. J. Gordon, T. A. Moore, T. K. Minton, and K. P. Giapis, *Phys. Rev. Lett.* **77**, 3049 (1996).

Chapter 7. Feature Profile Simulation of Dual Damascene Process

As CMOS transistor scaling proceeds into the deep sub-micron regime, the signal integration has necessitated integrated circuits feature with as many as eight layers of high density metal interconnect. The resistance capacitance (RC) delay of these metal interconnection has dominated the circuit performance. It is the major motivating factor for the semiconductor industry to switch from the traditional aluminum interconnect metal with silicon dioxide dielectric between the metal lines, to copper metal and low-k dielectric materials. The introduction of copper interconnects into integrated circuits has increased the use of dual damascene etch processes because of the difficulty in dry etching copper films.[1,2]

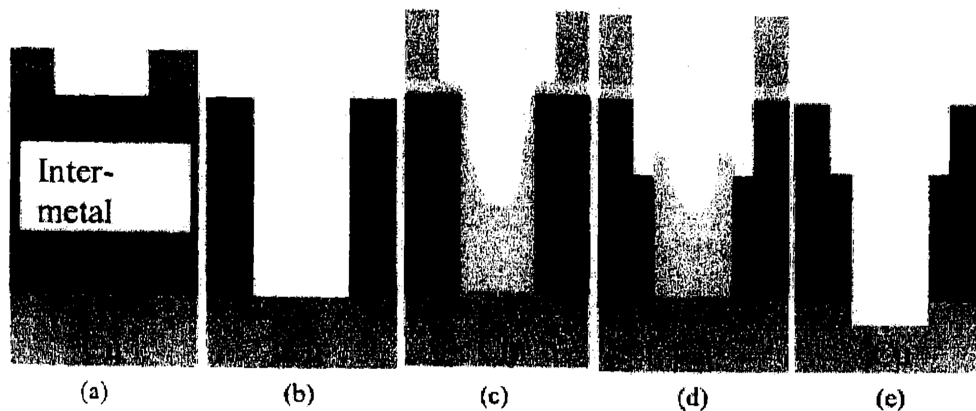

Figure 7-1: Process Sequence for the via-first dual damascene integration scheme: (a) via pattern; (b) via etch and photoresist ash; (c) trench pattern with BARC in vias; (d) trench etch; (e) photoresist ash and bottom stop layer removal.

Although either the trench or the via can be etched first in dual damascene etch process, most semiconductor manufacturers have chosen to adopt the via-first approach.[3,4] The via-first dual damascene etch process is shown in Figure 7-1. Wafers are first coated with photoresist and then lithographically patterned. Next, vias are formed by an anisotropic etching step, which stops on the bottom stop layer. It is important that the via etch does not break through this bottom layer, otherwise the via etch will sputter the copper located beneath the barrier up into the unprotected via hole. The copper will then quickly diffuse into the dielectric layer, leading to device failure. Next, the via photoresist layer is stripped, and bottom antireflection coating (BARC) is then deposited to fill a portion of the via. The BARC

protects the via during the subsequent trench etch. Next, the trench photoresist is applied and lithographically patterned. The trench etch is timed to stop at the desired depth. After trench etch, the resist and BARC from trench pattern is ashed, and the bottom stop layer is removed in a separate step. Then a barrier/seed layer is deposited, followed by electrochemical fill of the dual damascene structure with copper. The entire stack is then planarized by CMP, avoiding the dry etching of copper. Processing then continues with the formation of the next metal interconnect layer.

In the via-first dual damascene etch processes, some undesirable etching artifacts, including microtrenching, trench bottom rounding, faceting of the existing via holes and oxide fencing around the via hole, have been observed.[5,6] Figure 7-2 shows the oxide fencing after trench etch. These particular features can cause problems such as voids during copper fill of the dual damascene structure, and ultimately increased via resistance and device failure. To improve the fundamental understanding of the origin of the observed features, numerical profile simulations using Monte Carlo method were carried out, which have demonstrated great success in simulating poly-silicon trench etch process.[7,8]

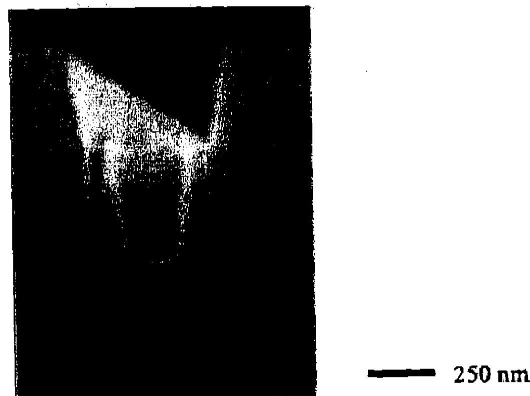

Figure 7-2: Scanning electron microscopy photograph of a via-first dual damascene trench etch illustrating oxide fencing around the via hole. Reprinted by permission from Ref. 7.

7.1. Surface kinetics model

In a polymerizing chemistry, such as fluorocarbon, the etching rate observed is the result of competition between etching and deposition.

$$ER_{net} = ER_{gross} - DR \tag{7-1}$$

Ion enhanced chemical etching models derived from site balance relationships determined by Langmuir adsorption kinetics have been extensively used to model a variety of etching systems.[9-11] We follow a similar approach for developing a phenomenological model that accounts for the energy, flux and angular dependence of ion enhanced SiO_2 etching with fluorocarbon reactants. This approach should capture most of the observed trench etch behavior, as long as we are in a process regime without significant deposition of fluorocarbon films (i.e., not near etch stop). Besides, not trying to separate the gross etching rate from the deposition rate, we are modeling these two as a whole, i.e. the net etching rate. Therefore, although the deposition rate is not explicitly extracted, its effect has already been incorporated in the model.

As proposed by Gray *et. al.*,[12] the SiO_2 etching rate includes three parts: thermal etching by neutrals, physical sputtering by ions, and ion enhanced etching

$$ER_{gross} = k_0 \Gamma \exp\left(\frac{-E_a}{kT}\right) + Y_P (1-\Theta)\Gamma_+ + Y_{IE}\Theta\Gamma_+ \qquad (7\text{-}2)$$

where k_0 and E_a are rate parameters for spontaneous chemical etching, Γ is the neutral flux, Y_P is the physical sputtering yield, Θ represents the fraction of surface sites occupied by the reactant species, Γ_+ is the ion flux, and Y_{IE} is the ion enhanced etching yield while the surface is saturated with reactant species.

It is well known that the spontaneous etching of SiO_2 with fluorocarbon neutrals is negligible under typical processing conditions, but the etching rate is greatly enhanced by ion bombardment. So the first term on the right side in Eq. (7-2) can be neglected. Due to the lack of knowledge of physical sputtering yield with reactive fluorocarbon ions, Y_P in the second term is approximated as the physical sputtering yield by Ar^+, which has a value of 0.17 to 0.25 while the ion bombardment energy increases from 300 eV to 500 eV.[13] Ion enhanced chemical etching yield, Y_{IE}, as appears in the third term, varies with etching chemistry and ion bombardment energy, and has a value of about 2 in C_2F_6 etching chemistry and 300eV.[14] This measured etching yield value is the net etching yield, therefore has already taken into account the deposition rate.

The following site balance equation is used to solve for Θ

$$n_0 \frac{d\Theta}{dt} = s\Gamma(1-\Theta) - a_{IE} Y_{IE} \Gamma_+ \Theta \tag{7-3}$$

where the first term on the right side represents the adsorption rate, and the second term is the fluorocarbon species removal rate due to the ion enhanced chemical etching reaction. s is the fluorocarbon neutral sticking coefficient, and a value of 0.5 is assumed. In the fluorocarbon via etch simulation performed at Lam Research, the fitted sticking coefficient of about 0.5 is also required to obtain good agreement with observed profile evolution.[15] a_{IE} is a stoichiometric coefficient representing the average number of fluorocarbon species that combines with SiO_2 to form the product species, and a value of 2 is assumed corresponding to the following apparent surface reaction

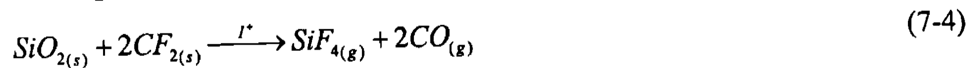

$$SiO_{2(s)} + 2CF_{2(s)} \xrightarrow{I^+} SiF_{4(g)} + 2CO_{(g)} \tag{7-4}$$

7.2. Angular dependent etching yield

To reveal the etching on the sidewalls where ion impingement is at grazing angle, the effect of ion incident angle has to be taken into account. The etching yield is a function of ion impingement angle. Depending on the etching mechanism, the shape of angular dependent etching yield curve may be different. For Ar^+ ion sputtering of silicon, the angular dependence follows the typical physical sputtering yield curve, with a maximum near 50° corresponding to the angle for maximum momentum transfer.[16] With reactive gases, the ion enhanced chemical etching does not show the same behavior as a function of angle.[16-21] For polysilicon etching with Cl/Cl^+ and HBr plasma beam, the etching yield is constant or slowly decreases from normally incident angle (0°) to 50°-60° off normal, and falls off rapidly above 60° off normal.[16,17,21] The possible reaction mechanism attributing to the observed angular dependence is that reactive atoms are implanted into the substrate more readily with normally incident ions. The normally incident ions consequently create mixing of the absorbed surface atoms into the lattice whereby enhancing the etching yield. In addition, the processes leading to the product formation by chemical sputtering are associated with the number of bonds broken within the surface layers, rather than momentum transfer to the surface atoms which is needed for physical sputtering. The number of bonds broken by the ion impingement

within the surface layers is not expected to vary significantly except at large off-normal angles where ion scattering occurs without losing much energy to the surface.

For SiO_2 etching in a fluorocarbon plasma, the angular dependent etching yield curve is similar to polysilicon etching in a Cl_2/HBr plasma.[14] The etching yield reaches the highest at the normally incident angle, and drops with increasing off-normal angle. But there exists some difference between different chemistries, as shown in Figure 7-3.

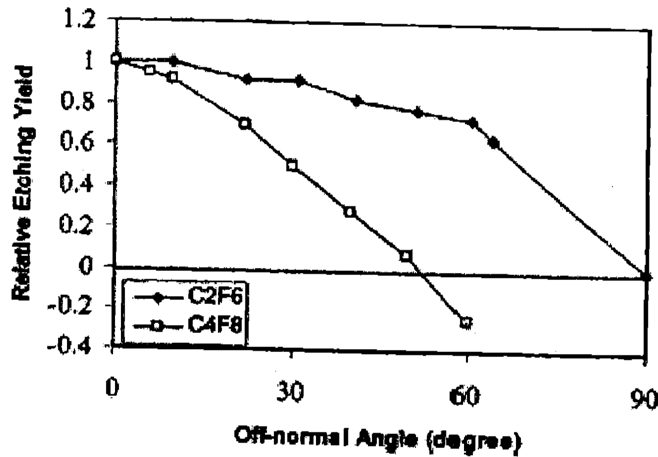

Figure 7-3: Angular dependent etching yield of SiO_2 in C_2F_6 and C_4F_8. Reprinted by permission from Ref. 15.

For a highly polymerizing chemistry such as C_4F_8, the etching yield drops faster than in a less polymerizing chemistry such as C_2F_6, and etching stops at a specific off-normal angle, and above this angle, net deposition happens. Kwon *et. al.* proposed an ion enhanced chemical etching and deposition competition mechanism, and developed a model with a single parameter, the ratio of etching rate to deposition rate, to fit the angular dependent etching yield curve in various chemistries, including C_2F_6, C_4F_8 and CHF_3.[22] They assumed that the ion enhanced chemical etching has an angular dependent etching yield curve similar to polysilicon etching with Cl_2, and the ion enhanced deposition has an angular dependent curve similar to typical physical sputtering curve. The net etching rate is the difference between ion enhanced etching rate and ion enhanced deposition rate. Therefore, different angular dependent etching yield curve can be achieved by adjusting the ratio of etching rate and deposition rate. In this work, we use the actually measured angular dependent etching yield curve in the simulation. Therefore, although we did not explicitly perform the deposition calculation, the effect of deposition on the angular dependent etching rate has been

implicitly included. The difference of angular dependent etching yield curve can have significant effect on feature profile evolution, as illustrated later in this article.

All the steps during via-first dual damascene processes can be simulated using the same methodology. A typical feature profile evolution simulated by the Monte Carlo method is shown in Figure 7-4. We focus on the trench etch step. To simplify the calculation, we assume that the photoresist is not etched. This simplification will not significantly affect the trend of oxide fencing forming, the main artifact we are trying to capture, as demonstrated later in this chapter.

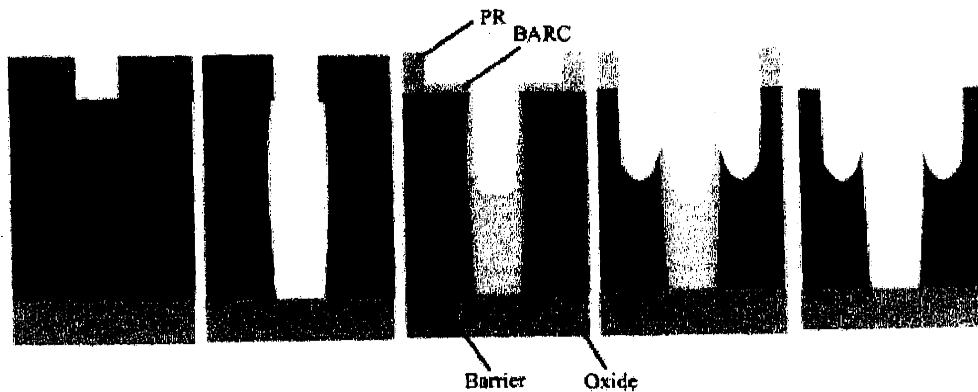

Figure 7-4: A typical profile evolution created by Monte Carlo simulation for dual damascene etching process.

7.3. Simulation results and discussion

We simulate the trench etching in a typical inductively coupled plasma etcher. The simulated process conditions are 2000 W source power, 1200 W bias power, and 50 mTorr. For all the work described here, except where noted, C_2F_6 etching chemistry is used.

7.3.1. Effect of ion and neutral flux distribution

Due to the collisions of ions in the presheath, the ions are not perfectly directional and have an angular distribution, which is normally assumed to be a Gaussian distribution and characterized by its standard deviation, σ.

$$N(\theta) = \frac{N_0}{\sqrt{2\pi}\sigma} \exp(-\frac{\theta^2}{2\sigma^2}) \tag{7-5}$$

where, θ is the off-normal angle. Under a typical processing condition in a commercial high density inductively coupled plasma etcher, σ is between 2° and 8°.[23] For all the work described here, except where noted, σ is taken as 5°. The ion angular distribution can have a significant effect on the profile evolution. Figure 7-5 compares the simulated feature profile evolution for the case of perfect ion directionality ($\sigma = 0^{\circ}$) and $\sigma = 5^{\circ}$. To simplify, assume no angular dependent etching yield, *i.e.* ions striking surface at different angles have the same etching yield. The etching selectivity to BARC is also assumed to be infinite, *i.e.* no BARC is etched during trench etch process. The neutral-to-ion flux ratio is 100:1, therefore the surface is saturated with neutrals and the etching is in the ion-limited regime.

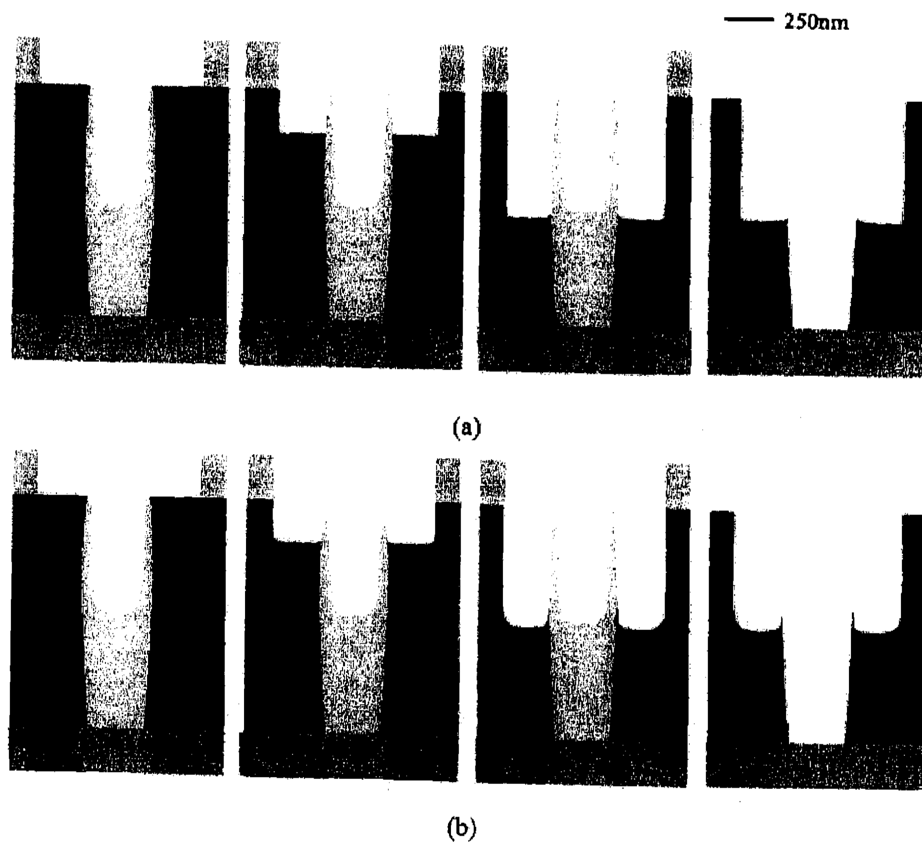

Figure 7-5: Effect of ion directionality on feature profile evolution by simulation: (a) perfect directionality; (b) Gaussian distribution with $\sigma = 5^{\circ}$. Assume ion enhanced etching yield does not depend on ion incidence angle, and neutral-to-ion flux ratio=100:1. Ion energy=300eV.

In Figure 7-5(a), due to the perfect ion directionality, the etching surface moves downwards smoothly as the etching process proceeds, and after the etching, an ideal profile is obtained. While in Figure 7-5(b), the broader ion angular distribution results in nonideal

profile. The bottom of trench is rounded and after the etching, oxide fencing remains at the corner of trench step. Undercutting is also observed, since ions striking the sidewall also cause etching, instead of being scattered, which exaggerate the sidewall etching to some extent.

To quantify the ion flux distribution, the number of ions striking each cell along the etching surface for a specific profile during trench etch is counted and shown in Figure 7-6. The ion flux to the top surface is relatively constant, where the fluctuation is due to the stochastic noise. Along the sidewall surface, the ion flux is relatively low, since the ions are highly directional. But along the trench bottom, there exists a significant variation of ion flux; the ion flux is the highest the center and drops gradually towards the corner due to the ion shadowing by SiO_2 sidewall or remaining BARC. To be noted also is that the variation is not symmetrical, since the shadowing effect of the sidewall and remaining BARC is different.

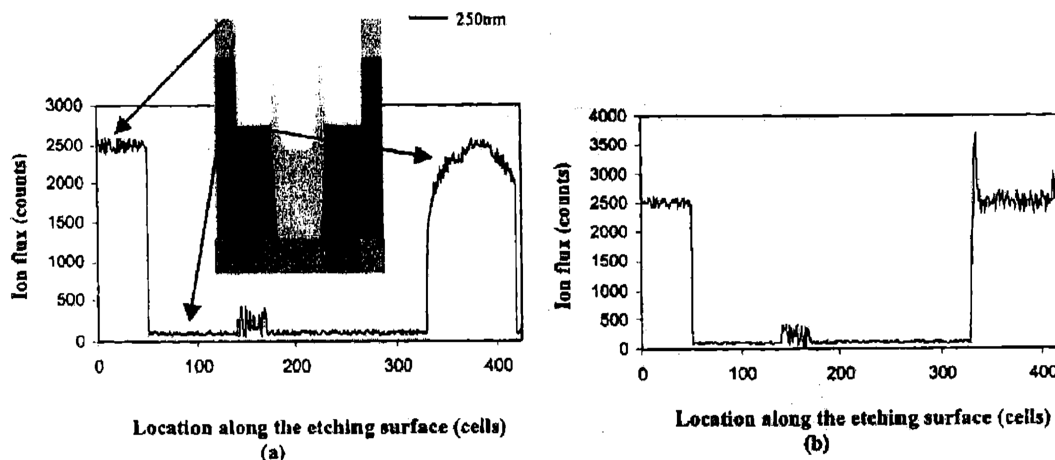

Figure 7-6: Ion flux distribution along the etching surface for a specific feature profile during trench etch. (a) Assume ion enhanced etching yield does not depend on ion incidence angle, therefore no ion reflection effect; (b) Assume ion angular dependent etching yield of C_2F_6 as shown in Figure 7-3.

Starting from this profile, as the etching proceeds, the higher etching rate at the center of bottom surface due to higher ion flux results in the rounding of the bottom surface. And after the etching, there is some oxide fencing remaining on the sidewall of BARC, as shown in Figure 7-7(a). In reality, ion enhanced etching yield also depends on the ion incident angle. With a rounded bottom surface, when ions strike at the center of bottom surface, the nearly normal striking angle results in higher etching yield than when ions strike cells near the

corner of bottom surface with some off-normal angle. On the other hand, ions striking sidewall at grazing angle tend to be scattered, instead of causing etching, and be focused at the foot of the sidewall. The ion flux distribution along the etching surface with angular dependent etching yield curve of C_2F_6 is shown in Figure 7-6(b). As the etching proceeds, the actual profile will be a result of both the ion reflection effect and ion angular dependent etching yield effect. The ion angular dependent etching yield causes the sidewall tapering, and the increased ion flux at the foot of sidewall due to ion focusing results in microtrenching, as shown in Figure 7-7(b). Several authors have shown both by numerical simulation and direct experiments that microtrenching can happen due to the ion reflection from feature sidewalls.[24-26]

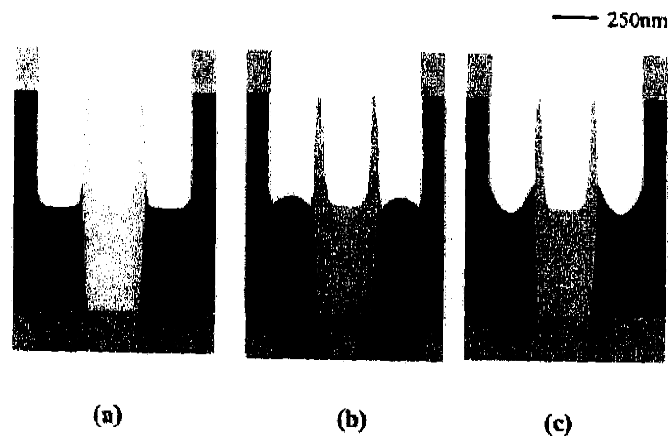

Figure 7-7: Continued profile evolution from the profile shown in Figure 7-6: (a) no angular dependent etching yield; (b) angular dependent etching yield shown in Figure 7-3 for C_2F_6; (c) neutral-to-ion flux ratio =10:1.

For the more practical case of an etch process which is weakly ion-limited, the neutral flux distribution also plays an important role. The neutrals entering the simulation domain were sampled from an isotropic distribution giving a cosine flux distribution at a planar surface. The cosine law follows from an assumption of complete randomness of the motion of individual molecules. Since the neutral flux at the center of feature bottom is higher than at the corner due to the sidewall shadowing effect, the etching rate at the center is higher than at the corner providing that the ion flux is the same, giving rise to bottom rounded profiles. Therefore, the actual feature profile is a result of the competition of relative importance between ion flux and neutral flux distribution effect, and the ion angular dependent etching yield as well. Under the neutral-to-ion flux ratio of 10:1, which is the typical case in a real inductively coupled etcher, the profile after etching is shown in Figure 7-7(c). Both theoretically and practically, it is possible to tune process parameters such as pressure or

power so that the relative importance of ion flux and neutral flux distribution can be adjusted and thus the feature profile,[27] which is beyond the scope of this work. For all the work described here, except where noted, the neutral-to-ion flux ratio is 10:1.

The feature profile evolution is controlled by both the ion and neutral flux distribution and angular dependent etching yield. It became obvious that factors such as feature size, via shape and etching selectivity to the BARC may affect the ion flux distribution. Etching chemistry may affect the angular dependent etching yield and the deposition onto sidewall surface. We will investigate the effect of these factors on profile evolution by simulation and compare the simulation results with observation obtained from literature.

7.3.2. Effect of via shape

In the via-first dual damascene integration scheme, the trench profile depends upon the via shape and whether any BARC is in the via hole prior to starting the trench etch. These effects are caused by the ion and neutral shadowing by the remaining BARC. Figure 7-8 shows the feature profile evolutions in the case of bowed via, straight via and tapered via.

In the case of bowed via, the largest diameter of via appears in the middle of the via hole. Due to this specific shape of BARC, the shadowing effect by remaining BARC is at minimum. As shown in Figure 7-8(a), there is no oxide fencing remaining after the trench etch. In the case of straight via, the perfectly vertical BARC cannot completely eliminate the shadowing effect since the ions are not perfectly directional and neutrals are cosine distributed. Therefore, after the trench etch, there is still some oxide fencing remaining, as shown in Figure 7-8(b). And in the case of tapered via, the largest diameter of via appears at the top of via hole. Therefore, there exists fairly amount of oxide material directly below the tapered BARC, which cannot "see" ions. The shadowing effect is the worst, and after the trench etching, the remaining oxide fencing is the highest, as shown in Figure 7-8(c). Therefore, it is possible to intentionally adjust the via profile to prevent the oxide fencing from forming. These simulation results qualitatively agree with the experimental results.

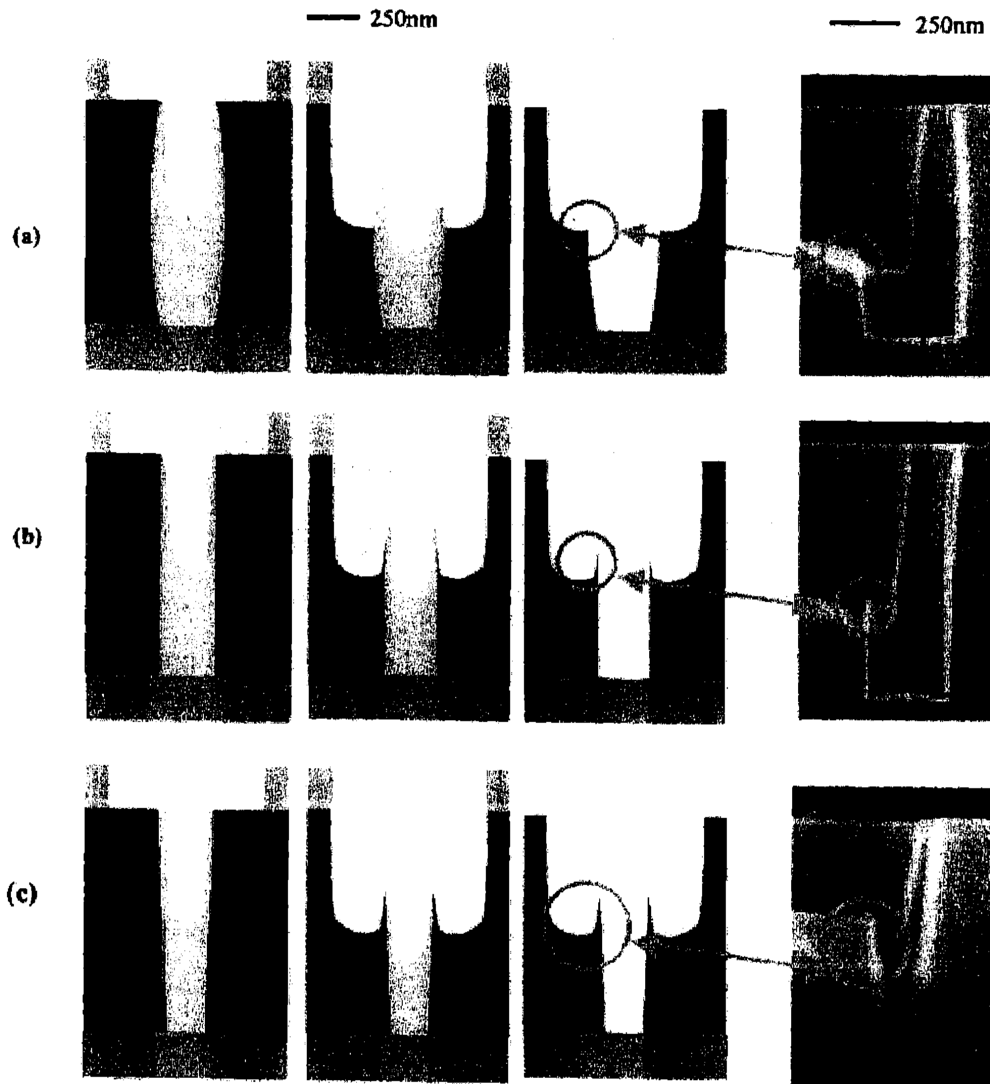

Figure 7-8: Effect of shape of via hole on the profile evolution during the trench etching, simulation compared with experimental: (a) bowed via; (b) straight via; (c) tapered via. Experimental results reprinted by permission from Ref. 6.

*7.3.3. **Effect of etching selectivity to BARC***

The etching selectivity of oxide to BARC determines the height of remaining BARC during the trench etch, thus the ion shadowing effect. As shown in Figure 7-9, by reducing the etching selectivity, the height of remaining BARC decreases and as well the oxide fencing. In the case of 1:2 etching selectivity, the BARC etches even faster than oxide material, so the height of BARC is always lower than the etched trench surface, and there is no ion shadowing effect at all. After trench etching, there is no oxide fencing remaining. Applied Materials has successfully minimized the fencing height by decreasing the selectivity

to BARC.[7] But this approach is not practical for advanced dual damascene structures with low initial photoresist thickness, since the etching selectivity to photoresist is also lower resulting in excessive etching of photoresist itself

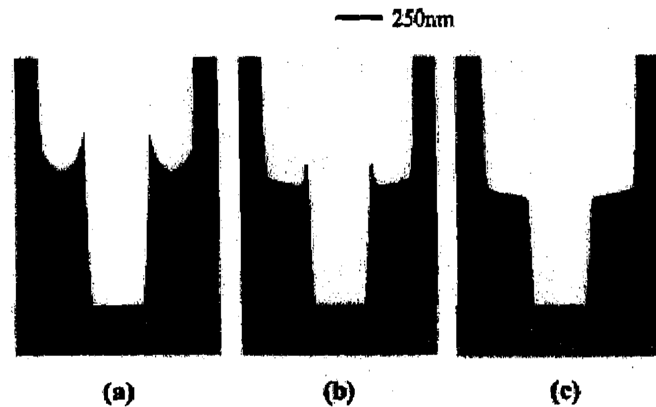

Figure 7-9: The effect of etching selectivity of SiO_2 to BARC on the profile evolution: (a) selectivity of 5:1; (b) selectivity of 2:1; (c) selectivity of 1:2.

7.3.4. Effect of etching chemistry

Jiang *et al.* discovered that the N_2 :Ar ratio in $C_4F_8/N_2/Ar$ chemistry is the key parameter in controlling the severity of the oxide fencing.[6] The oxide fencing can be eliminated at a low N_2:Ar ratio. It is believed that a low N_2:Ar ratio increases physical sputtering, thus shift the angular dependent etching yield curve in a C_4F_8 chemistry towards C_2F_6 chemistry. To study the effect of the difference in angular dependent etching yield on profile evolution, the simulations are carried out for two cases with different angular dependent etching yiled curve, as shown in Figure 7-10. To simplify, the deposited material is assumed to have the same composition as SiO_2, which may result in the deviation of simulated profile from the real one to some extent, but will not change the trend of oxide fencing formation.

As shown in Figure 7-11, in a less polymerizing chemistry such as C_2F_6, there is very little oxide fencing remaining after the etching. While in a more polymerizing chemistry such as C_4F_8, due to the deposition on the SiO_2 and BARC sidewall, the oxide fencing is much more severe. Therefore, tuning the etching chemistry is a potentially effective approach to achieve ideal feature profile.

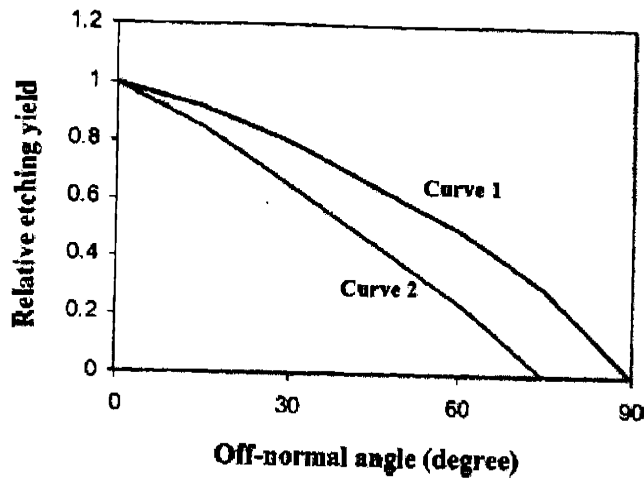

Figure 7-10: Two angular dependent etching yield curves for the study of effect of etching chemistry on profile evolution. Curve 1: less polymerizing chemistry; curve 2: more polymerizing chemistry.

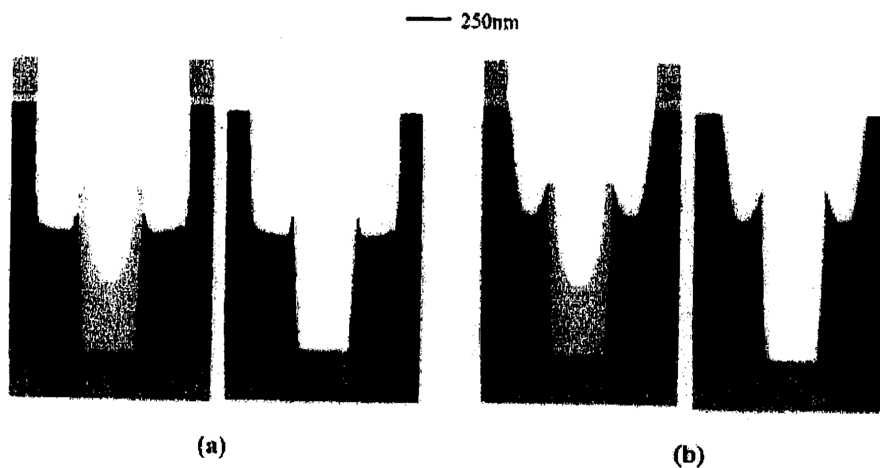

Figure 7-11: The effect of etching chemistry on profile evolution: (a) with angular dependent etching yield curve 1 shown in Fig. 10; (b) with angular dependent etching yield curve 2 shown in Fig. 10.

In practice, different etching chemistry also results in different etching selectivity. For example, less polymerizing chemistry such as C_2F_6 generally has a lower etching selectivity. Although the effect of both the less polymerizing etching chemistry and lower etching selectivity gives rise to a more ideal profile, the restraint arising from low initial photoresist thickness limits the extensive use of this approach.[28] Therefore, these effects have to be taken into account together, and care is needed when tuning the etching chemistry to optimize the feature profile.

7.3.5. Inclusion of photoresist etching

In the simulation shown above, for simplification, the photoresist (PR) is assumed not to be etched. To investigate the effect of this simplified assumption on the feature profile, we compared simulated profiles with and without photoresist etching, as shown in Figure 7-12. To isolate the effect of BARC etching, in both cases we assume that BARC is not being etched. The angular dependent etching yield of photoresist is assumed to be the same as the SiO_2 substrate, due to the lack of data available, and etching selectivity of SiO_2 to PR is 3:1. As shown in Fig. 12, the PR has been completely removed in the case that PR is allowed to etch, therefore gives the maximum effect of PR etching on feature profile evolution. It is obvious that the simulated profile with PR etching shows slightly lower oxide fencing than that without PR etching. With PR etching, the aspect ratio of the final feature is lower than without PR etching, resulting in less severe sidewall shadowing and ion reflection effect. If the difference of aspect ratio with and without PR etching is significant, neglecting PR etching in the simulation might result in quantitative disagreement of simulation results from experimental results. However, for practicing process engineers, what matters most is the identification of trends. In this regard, the simulations assuming that PR is not etched provide an accurate prediction of expected trends, as long as the PR is not totally etched away during trench etch.

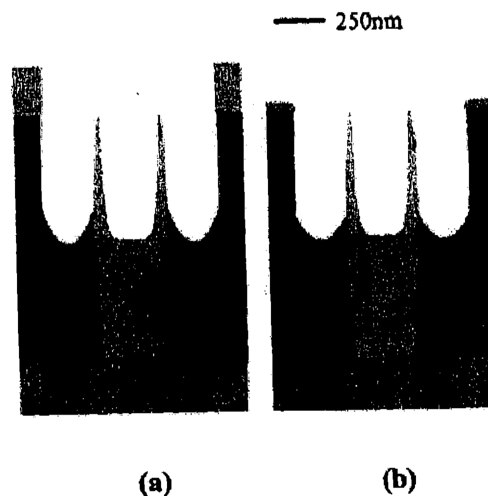

Figure 7-12: Comparison of simulated feature profile (a) without photoresist etching; (b) with photoresist etching, etching selectivity of SiO_2:PR=3:1.

7.4. Conclusion

The mechanisms of oxide fencing that occurs during trench etch of a via-first dual damascene scheme is investigated. Monte Carlo simulations are carried out to predict the feature profile evolution and oxide fencing formation under different conditions. The simulation results qualitatively agree with the experimental results and facilitate our understanding of profile evolution. Both the simulation results and experimental results suggest that the oxide fencing depends on the shape of via hole, and is most severe with a tapered via. The oxide fencing height is also dependent upon the oxide:BARC selectivity during the trench etch.

The oxide fencing is also affected by the etching chemistry used. With a less polymerizing chemistry such as C_2F_6 or adding Ar to C_4F_8, the oxide fencing is relatively small. While with a more polymerizing chemistry such as C_4F_8, due to the deposition onto the SiO_2 and BARC sidewall, the oxide fencing is much more severe. These results demonstrate that the fabrication using via-first dual damascene etching processes can be optimized by intentionally controlling the via shape and tuning the etching chemistry without the use of a middle stop layer.

7.5. References

1. J. G. Ryan, J. E. Heidenrich, W. J. Cote, R. M. Geffken, and T. N. Theis, in *Advanced Metallizationand Interconnect Systems for ULSI Applications in 1997, Proceedings of ULSI XIII*, IEEE, p. 399 (1998).

2. R. DeJule, *Semicond. Int.* **6**, 94 (2000).

3. M Naik, S. Parikh, P. Li, J. Educato, D. Cheung, I. Hashim, P. Hey, S. Jeng, T. Pan, F. Redekar, V. Rama, B. Tang, and D. Yost, in *Proceedings of the International Interconnect Technology Conference*, IEEE, p. 191 (1999).

4. Z. Sui, C. Frum, H. Shan, D. Lymberopoulos, B. J. Su, and Yi-Hong Chen, *Solid State Technol.*, **45**, 28 (2002).

5. P. Jiang, F. G. Celii, W. W. Dostalik, and K. J. Newton, *J. Vac. Sci. Technol. A*, **19**, 1388 (2001).

6. T. Kropewnicki, K. Doan, B. Tang, and C. Bjorkman, *J. Vac. Sci. Technol. A*, **19**, 1384 (2001).

7. R. N. Tait, S. K. Dew, T. Smy, and M. J. Brett, *J. Vac. Sci. Technol. A*, **12**, 1085 (1994).

8. R. J. Hoekstra and M. J. Kushner, *J. Vac. Sci. Technol. A*, **16**, 3274 (1998).

9. R. A. Gottscho, C. W. Jurgensen, and D. J. Vitkavage, *J. Vac. Sci. Technol. B*, **10**, 2133 (1992).

10. T. M. Mayer and R. A. Barker, *J. Vac. Sci. Technol.*, **21**, 757 (1982).

11. J. A. Levenson, E. S. G. Shaqfeh, M. Balooch, and A. V. Hamza, *J. Vac. Sci. Technol. A*, **15**, 1902 (1997).

12. D. C. Gray, I. Tepermeister, and H. H. Sawin, *J. Vac. Sci. Technol. B*, **11**, 1243 (1993).

13. J. M. E. Harper, J. J. Cuomo, P. A. Leary, G. M. Summa, H. R. Kaufman, F. G. Bresnock, *J. Electrochem. Soc.*, **128**, 1077 (1981).

14. H. Chae, Ph.D. thesis, Massachusetts Institute of Technology, 2000.

15. D. Keil, D. Cooperberg, L. Li, G. Mueller, T. Nguyen, K. Khajehnouri, V. Vahedi, and G. Hills, in *Plasma Processing XII*, G. S. Mathad, D. Misra, and K. B. Sundaram, Editors, PV 98-4, p. 114, The Electrochemical Society Proceedings Series, Pennington, NJ (1998).

16. S. A. Vitale, H. Chae, and H. H. Sawin, *J. Vac. Sci. Technol. A*, **19**, 2197 (2001).

17. J. P. Chang, A. P. Mahorowala, and H. H. Sawin, *J. Vac. Sci. Technol. A*, **16**, 217 (1998).

18. T. M. Mayer, R. A. Barker, and L. J. Whiteman, *J. Vac. Sci. Technol.*, **18**, 349 (1981).

19. H. Okano and Y. Horiike, *Jpn. J. Appl. Phys.*, **20**, 2429 (1981).

20. B.-O. Cho, S.-W. Hwang, G.-R. Lee, and S. H. Moon, *J. Vac. Sci. Technol. A*, **18**, 2791 (2000).

21. W. Jin, S. A. Vitale, and H. H. Sawin, *J. Vac. Sci. Technol. A*, **20**, 2106 (2002).

22. O. Kwon, W. Jin and H. H. Sawin, in Plasma Processing XIV, G. S. Mathad, M. Yang, R. E. Sah, and M. D. Allendorf, Editor, PV 2002-17, p. 251, The Electrochemical Society Proceeding Series, Philadelphia, PA (2002).

23. J. R. Woodworth, M. E. Riley, P. A. Miller, and G. A. Hebner, *J. Appl. Phys.*, **81**, 5950 (1997b).

24. S. Ohki, M. Oda, H. Akiya, and T. Shibata, *J. Vac. Sci. Technol. B*, **5**, 1611 (1987).

25. A. C. Westerheim, A. H. Labun, J. H. Dubash, J. C. Arnold, H. H. Sawin, and V. Yu-Wang, *J. Vac. Sci. Technol. A*, **13**, 853 (1995).

26. R. J. Hoekstra, M. J. Kushner, V. Sukharev, and P. Schoenborn, *J. Vac. Sci. Technol. B*, **16**, 2102 (1998).

27. D. Keil, B. A. Helmer, G. Mueller, and E. Wagganer, *J. Electrochem. Soc.*, **148**, 383 (2001).

28. T. Kropewnicki , Private communication (2002).

Chapter 8. Three-dimensional Profile Evolution Simulation

The development of 2-1/2 dimensional (2-1/2D) profile simulators for fabrication of microelectronics features has demonstrated great success in simulating poly-silicon trench etch and dual damascene processes, but increasingly complex devices that have three-dimensional (3D) structure require improved dimensionality in profile simulators to capture the most important features. To correctly capture the surface roughness also requires 3D simulation.[1]

8.1. Introduction

Similar to the 2-1/2D simulator, the Monte Carlo computation of the ion and neutral fluxes on the feature for the 3D simulator was performed using the simulation domain shown in Figure 8-1. The domain was discretized into a cubic cellular array with 25 Å sides, a dimension comparable to the characteristic length for compositional changes in ion induced processes. The cells were treated as having uniform compositions. Periodic boundary conditions are used for the domain.

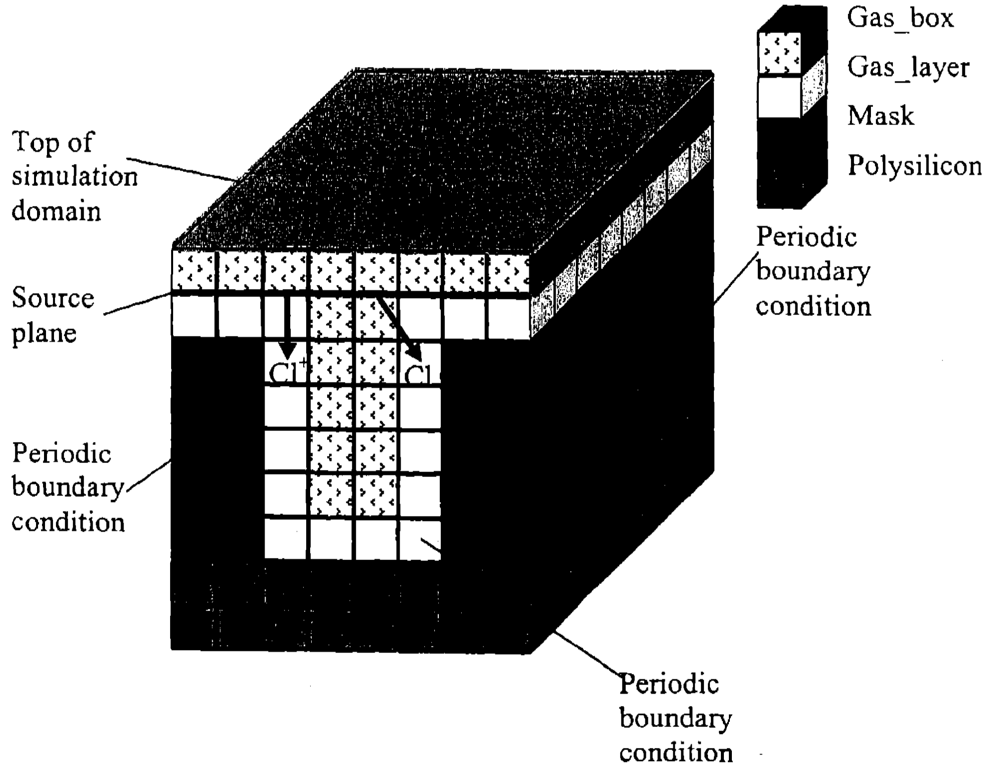

Figure 8-1: Schematic diagram of the 3D simulation domain. The simulation domain was

discretized into square cells with 25 sides. Periodic boundary conditions are used. A source plane was assigned above the feature from which the ions and neutrals emanated and passed into the feature without gas-phase collisions.

8.2. Ion and neutral trajectories computation

Reactant species were introduced at a source plane above the top of the feature. The initial position, (x, y), of the particle was selected randomly on the source plane. Each particle's trajectory was determined by randomly sampling from their respective distribution functions – cosine distribution for neutrals and Gaussian angular distributions for the ions.[2] Acceptance-rejection criteria were used to sample from either distribution.[3] All three (x, y, and z) velocity components were determined.

After determining the particle's origin and trajectory, it was stepped one cell length at a time until it reached a surface cell. A particle that crossed the left boundary entered into the feature from the right side, retaining its original velocity. A particle that crossed other three boundaries is treated similarly.

To test the 3D ion and neutral trajectory computation, the flux onto various surfaces in the feature is tracked and compared with the 2-1/2D case. The size of the sample feature used for flux computation is shown in Figure 8-2. The neutral and ion flux onto the cross-sectional surface, as shown by the dashed line in Figure 8-2(a), were tracked and compared with the corresponding 2-1/2D case, as shown in Figure 8-2(b). During this process, no surface reaction was turned on so that the feature profile keeps unchanged. The neutral flux and ion flux calculated by 3D simulator and 2-1/2D simulator are compared in Figure 8-3(a) and (b), respectively. The agreement as shown in Figure 8-3 demonstrated the correctness of neutral and ion trajectory calculation in the 3D simulator.

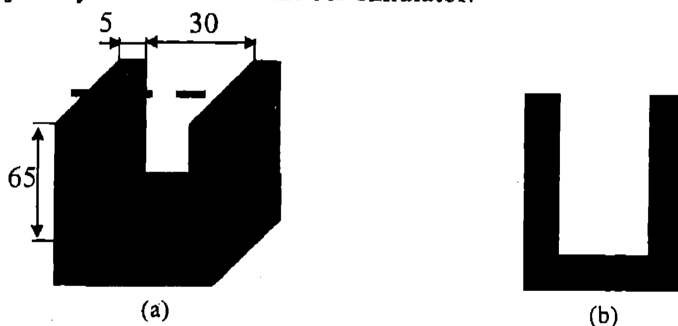

Figure 8-2: Sample feature for the comparison of neutral and ion flux calculated by 3D and 2-1/2D simulator, respectively. (a) 3D structure; (b) 2-1/2 structure.

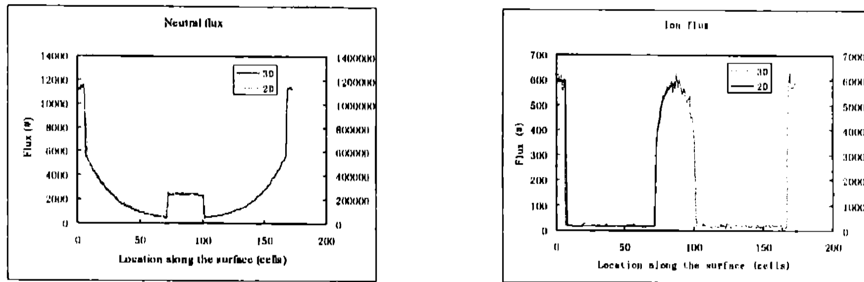

Figure 8-3: Comparison of flux calculated by 3D simulator and 2-1/2D simulator for the structure shown in Figure 8-2. (a). neutral flux; (b). ion flux.

8.3. Surface normal calculation

The main mechanism for the 3D simulator is not significantly different from the 2-1/2D simulator. The chemical reaction kinetics module is exactly the same as the 2-1/2D simulator. The cell removal and creation module is similar, except that we have to consider six neighboring cells instead of four when we implement the operation. The main difference lies in the surface normal calculation and surface representation.

In the 2-1/2D simulator, the surface is represented by collecting the center of neighboring cells. But for the 3D simulator, for the simplification of coding, the surface is represented by the outer edge of each cell. The disadvantage is that representing the surface by the outer edges of the cells led to exaggerated shadowing of off-normal fluxes and increased the flux to the cells that protruded from a surface, as pointed out by Mahorowala.[4] A new method of surface representation is recommended in Section 9.2.

8.3.1. Six-point normal calculation

Since the neutrals were assumed to have thermally equilibrated with the feature surface, the trajectories of neutrals species that were not incorporated were calculated assuming a cosine distribution about the surface normal. The six-point technique was used to determine the surface normal, as shown in Figure 8-4. The six-point surface cell normal was determined by the presence/absence of the six adjacent neighboring cells. The surface normal can only vary discretely. However, the broad non-specular nature of neutral scattering from the surface made it unnecessary to determine the local surface normal more accurately.[5]

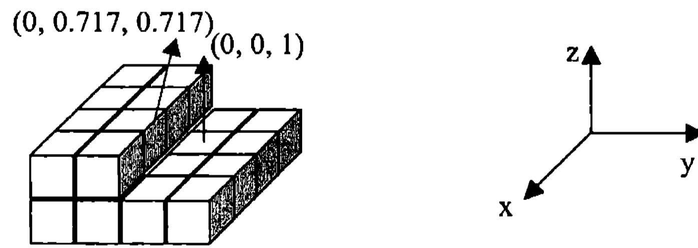

Figure 8-4: Six-point surface normal computation. The six-point surface cell normal was determined by the presence/absence of the six adjacent neighboring cells. The surface normal can only vary discretely.

8.3.2. Least-square surface normal approximation for specular scattering

The two dominant ion-surface interactions – etching and scattering are strong functions of the ion incidence angle. It would be impossible to correctly simulate etching artifacts such as microtrenching and faceting without an accurate surface normal calculation algorithm. Due to the stochastic nature of the simulations, microscopic roughness of the order of 1-2 cells is inevitable. Calculating the surface normal at a cell location based on the positions of its immediate neighbors is therefore subject to noise. This problem was overcome by calculating a surface normal based on a least square fitting of the surface normal.

The surface cells used to determine the surface normal were selected from the neighboring cells lying in a diamond pattern characterized by their diagonal. The cell type (0 for gas cell, and 1 for solid cell), Y, is regressed against the location of the cell, X. The regression coefficient c is the surface normal.

$$Y = cX + \varepsilon \tag{8-1}$$

$$c = (X'X)^{-1}X'Y \tag{8-2}$$

8.4. The validation of 3D simulation with 2-1/2D simulation

Several cases are run with the 3D simulator, and compared with 2-1/2D simulator to validate the 3D simulation code. We start with simple assumptions, and proceed towards more realistic models.

8.4.1. Etching with unit sticking probability for ions

In this case, ions are assumed to have unit sticking probability onto the surface, and etching yield is assumed to be constant independent of ion incident angle. The resultant feature profile is shown in Figure 8-5. The feature sidewall widening observed is due to the etching induced by off-normal ions. With the angular distribution of ions, the ion flux in the center of feature bottom is greater than in the corner, as shown in Figure 8-3, causing the etching in the center faster than in the corner, and therefore the feature bottom rounding. Comparison of the cross-sectional view in 3D simulation with 2-1/2D simulation shows identical feature profile, proving the correctness of the 3D simulation.

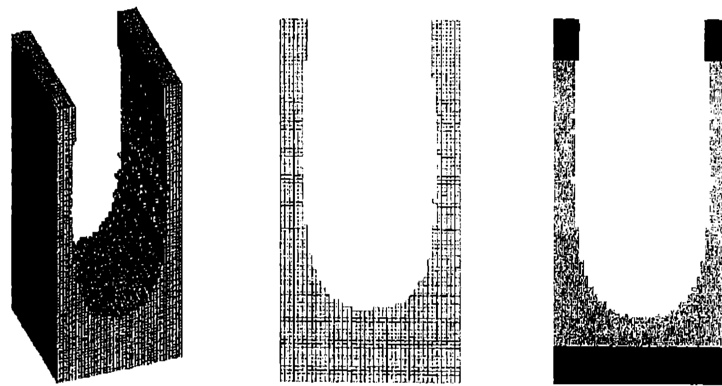

Figure 8-5: The comparison of feature profile simulated with 3D simulator and 2-1/2D simulator with unit sticking probability and no angular dependence of etching yield. (a). 3D view of profile created by 3D simulator; (b). Cross-sectional view of profile created by 3D simulator; (c). Profile created by 2-1/2D simulator.

8.4.2. Etching with angular dependent etching yield

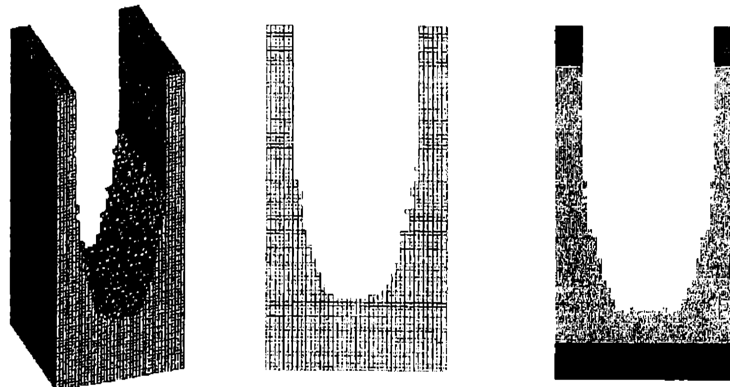

Figure 8-6. The comparison of feature profile simulated with 3D simulator and 2-1/2D simulator with unit scattering probability and angular dependence of etching yield. (a). 3D

view of profile created by 3D simulator; (b). Cross-sectional view of profile created by 3D simulator; (c). Profile created by 2-1/2D simulator.

In this case, ions are still assumed to have unit sticking probability onto the surface, but the etching yield depends on the ion incident angle. The angular dependent etching yield measured with Cl/Cl^+ beam is used for the simulation. The etching yield is almost constant while the ion incidence angle drops from normal to 45° off-normal. Then the etching yield drops to zero at 90° off-normal. The resultant feature profile is shown in Figure 8-6. Due to the angular dependence of etching yield, the off-normal ions striking the sidewall don't cause significant etching, therefore no sidewall widening is observed. The angular dependence of etching yield is coupled with ion flux distribution along the surface, causing the etching rate in the corner of feature bottom is much slower than in the center. Therefore significant amount of residual is observed in the corner of feature bottom, which needs extended etching time to clear. Comparison of profile created with 3D simulator and 2-1/2D simulator indicated agreement once again.

8.4.3. Etching with angular dependent sticking probability

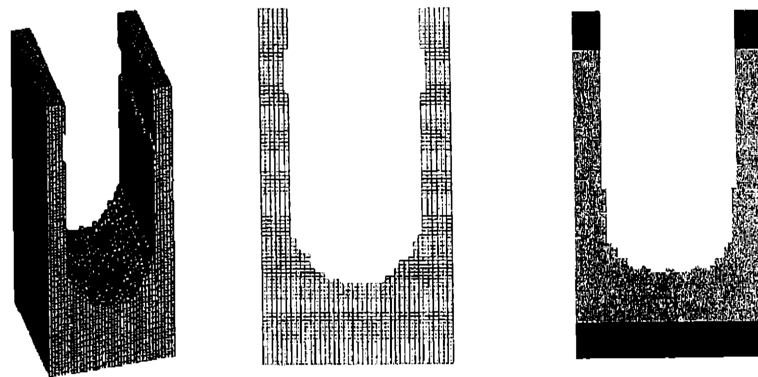

Figure 8-7: The comparison of feature profile simulated with 3D simulator and 2-1/2D simulator with ion scattering turned on. (a). 3D view of profile created by 3D simulator; (b). Cross-sectional view of profile created by 3D simulator; (c). Profile created by 2-1/2D simulator.

In reality, the sticking probability of ions depends on the incident angle. At glancing angle, ions are more likely to scatter without losing energy onto the surface. The observed drop of etching yield with large off-normal angle has been attributed to the ion scattering. If we assume that the drop of etching yield is solely because of ion scattering, the measured etching yield versus ion incident angle will translate to the ion sticking probability versus ion

incidence angle while etching yield is the same for each ion that sticks on the surface. Ions are assumed to be specularly scattered off the surface, and scattered ions are tracked until they strike other surfaces. The feature profile simulated with 3D simulator and 2-1/2D simulator are shown in Figure 8-7. Because the ions striking the sidewall were mainly scattered and focused on the corner of feature bottom, partly compensating the relatively smaller ion flux due to smaller view factor, feature narrowing is not observed. The agreement of 3D simulation and 2-1/2D simulation confirms the correctness of scattering calculation. The small difference immediately below the oxide mask might be due to the difference of surface normal calculation since different cells are used in the calculation.

8.4.4. Surface roughness analysis

Due to stochastic noise, neutral and ion flux vary at different locations on the surface. Therefore, etching rate at different locations may vary too, resulting in the so-called surface roughness. The neutral and ion flux onto a plane surface composed of 40x40 cells was counted while 5,000,000 ions and 95,000,000 neutrals are thrown onto the surface. The average ion flux onto a single cell is 3125 and the standard deviation is 56, while the average neutral flux is 59364 and the standard deviation is 243. Since the neutral flux is much higher than ion flux and its sticking probability is relatively low, the variation of neutral flux on the surface is less important in determining surface roughness. Therefore, the neutral flux can be considered as uniformly distributed on the surface, and the surface roughness is solely determined by the variation of ion flux along the surface. Suppose the etching yield of each ion is 1 and each cell consists of 30 silicon atoms initially, the ion flux calculated above will translate to the vertical etching of about 104 cells with a standard deviation of 2 cells. In the real simulation, when the local etching rate is higher in a specific site, it will be surrounded by relatively higher neighboring cells, which will shadow neutral and ion flux to the site. Therefore, the etching rate in the site will be slowed down. Obviously this kind of attenuation will smooth the surface. On the other hand, the surface roughness will also affect the local surface normal, which correlates with angular dependent etching yield and scattering, tends to make surface rougher. These two factors interact with each other, making the prediction of surface roughness with simple models difficult. With Monte Carlo simulator, these factors can be taken into account simultaneously, which makes the prediction of surface roughness possible.

A typical surface after etching is shown in Figure 8-8. The surface roughness seems to be uniform. Root-mean squared (RMS) roughness can be calculated for the surface to quantify the surface roughness. For example, a RMS of 0.6 cell was calculated for this surface, which means the surface elevation can vary with a standard deviation of 0.6 cell (i.e. 15Å). Obviously, the surface roughness due to ion flux nonuniformality on the sample surface in a pure etching regime is minimal. The significant surface roughness experimental observed might be due to some other mechanism, such as micromasking, as proposed by Rasgon, *et al.*[6]

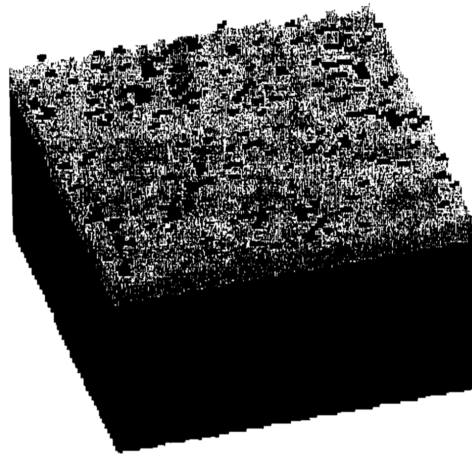

Figure 8-8: A typical simulated surface after etching (40x40 cells). Ion energy = 100 eV, neutral-to-ion flux ratio = 10:1.

8.5. Conclusions

We have constructed a three-dimensional (3D) Monte Carlo simulator to improve the fundamental understanding of feature profile evolution and surface roughness. Comparison of simulated results by the 3D simulator with the 2-1/2D simulator developed earlier in our lab verified the correctness of the 3D simulation code.

Under typical operating conditions, the simulation results give minimal surface roughness. This suggests that the nonuniformality of ion flux on the sample surface has limited effect on the formation of surface roughness. Some other mechanisms, such as micromasking, might explain the significant surface roughness experimental observed under certain operating conditions.

8.6. References

1. R. J. Hoekstra and M. J. Kushner, *J. Vac. Sci. Technol. A* **16**, 3274 (1998).

2. F. Ulacia, J. I., Petti, C. J., and J. P. McVittie, *J. Electrochem. Soc.* **135**, 1521 (1988).

3. G. A. Bird, *Molecular Gas Dynamics*, Oxford University Press, London (1976).

4. A. P. Mahorowala and H. H. Sawin, *J. Vac. Sci. Technol. B* **20**, 1064 (2002).

5. A. P. Mahorowala, Ph.D. thesis, Massachusetts Institute of Technology, 1999.

6. S. A. Rasgon and H. H. Sawin, *AVS 50th International Symposium*, Baltimore, MD (2003).

Chapter 9. Conclusions

9.1. Conclusions

This work has characterized the Cl_2/HBr ion enhanced plasma-surface interactions with poly-silicon as a function of the gas composition, ion energy, ion incident angle and other important process parameters. A realistic inductively coupled plasma beam apparatus capable of generating ions and neutrals representative of real commercial etcher was constructed and utilized to simulate accurately a high density plasma environment. Etching rate of poly-silicon, the oxygen effect and loading effect are quantified to better describe the etching of patterned poly-silicon in fabricating the gate electrode of a transistor in VLSI manufacturing process. The kinetics model derived from these measurements are incorporated into a Monte Carlo based feature profile simulator, and profile evolution has been simulated under various processing conditions.

To avoid the difficulty of constructing multiple beam sources independently to mimic the composition of a real commercial etcher, a realistic inductively coupled plasma was built as the source of ions and neutrals. The beam fluxes (Cl, Cl_2, Br, HBr, ClBr, Cl^+, Cl_2^+, Br^+, HBr^+, etc.) are representative of the composition of a real commercial etcher and are characterized by a mass spectrometer. $SiCl_4$ and O_2 can also be added to the feed gas to simulate the effect of etching product buildup in a real commercial etcher, i.e. the loading effect, and the oxygen effect when O_2 is intentionally added into the etcher to improve the etching selectivity of Si-to-oxide.

The etching yields of poly-silicon by Cl_2 and HBr plasma beam at different ion energies were measured. The etching yields were found to scale linearly with $(\sqrt{E_{ion}} - \sqrt{E_{th}})$, where the threshold energies, E_{th}, are 10 eV for both Cl_2 and HBr. The etching yields at different neutral-to-ion flux ratio were measured and the sticking coefficients are derived for reactive neutrals for Cl_2 and HBr. The sticking coefficient for HBr system is lower probably due to the relatively larger size of bromine atom compared with chlorine and its relatively lower chemical reactivity. The etching yields for mixed Cl_2+HBr plasma at different compositions were also measured. The etching yield by the HBr plasma beam is similar to the

Cl_2 plasma beam, although the etching rate by the HBr plasma is about 40% lower due to the lower ion flux. The angular dependence of etching yield by both Cl_2 and HBr strongly suggests the mechanism of ion enhanced chemical etching. With Cl_2 plasma beam, the etching yield almost keeps constant until the off-normal ion incident angle increased to 45°, while with the HBr plasma beam, the etching yield starts dropping even with small off-normal angle. The etching yield by Cl_2+HBr plasma at different composition exhibits a similar trend as pure HBr. The difference of angular dependent etching yield between Cl_2 and HBr might contribute to the difference of feature profile evolution in these two chemistries, i.e., more anisotropic etching in HBr plasma, as suggested by Monte Carlo feature profile evolution simulation.

The XPS peak for Cl(2*p*), Br(3*d*), and Si(2*p*) are integrated to quantify the relative concentration of different species on the sample surface after exposure to the plasma beam. The Cl coverage after etching with pure Cl_2 plasma beam is about 1.4 times higher than the Br coverage after etching with pure HBr plasma beam. The lower Br coverage is likely due to site blocking by coadsorbed H and adjacent adsorption site blocking by the larger Br atom. The Si(*2p*) was deconvoluted to differentiate Si(bulk), SiCl, $SiCl_2$ and $SiCl_3$. About 70% of the chlorine bromine adsorbed onto the surface is in the form of di- and tri-chloride. Similar results are observed for bromine. Inversion method was used to extract the depth profile from the angular resolved XPS measurement. The halogenation layer is about 15 – 25 thick, and the concentration of halogen decays exponentially as depth increases.

The effect of oxygen addition on the etching rate of poly-silicon was measured with the plasma beam/QCM apparatus. The etching rate has a different sensitivity to the oxygen addition with different surface composition. When the surface is chlorine rich, the etching rate is not sensitive to small amount of oxygen addition. When the surface is oxygen rich, the etching rate is more sensitive to oxygen addition. This explains that in a real commercial etcher, by adding small amount of oxygen, the poly-silicon etching rate does not change much, but the silicon oxide etching rate decreases significantly, therefore the etching selectivity can be achieved. The loading effect was studied by adding $SiCl_4$ into the feed gas to simulate the effect of etching product buildup in a real commercial etcher. The etching yield by the Cl_2 plasma beam is significantly affected by the $SiCl_4$ addition. The deposition of Si-containing species reduces the etching yield. The etching yield decreases drastically due to the ion enhanced deposition of Si-containing species as the concentration of $SiCl_4$ is low. As

the active sites created by ion bombardment are filled with $SiCl_x$, further reduction of etching yield is due to the chemisorbtion on nonactive sites, which is much slower than ion-enhanced deposition but more temperature sensitive. The surface halogen coverage after etching by Cl_2 with $SiCl_4$ addition is essentially the same as without $SiCl_4$ addition. A kinetics model has been developed to account for the effect of both ion-enhanced deposition and chemisorbtion on nonactive sites mechanism. The model represents the experimental data quantitatively well.

Feature profile evolution of poly-silicon gate etching under different conditions were obtained by Monte Carlo simulation and compared. The neutral-to-ion ratio was found to result in the variation of surface chlorination, which could influence the feature profile evolution. Different ion energy would result in different etching rate and the surface chlorination, thus influence the feature profile as well. Other facts, such as the mask angle, are also found to have some effects on the feature profile by our simulation, which agree with experimental results. The feature profile simulator was also used to simulate the dual damascene process, specifically the oxide fencing formation. The effect of various factors, including the via shape, etching selectivity, and etching chemistry was studied by the simulation and compared with experimental results from literature.

We have constructed a three-dimensional (3D) Monte Carlo simulator to improve the fundamental understanding of feature profile evolution and surface roughness. Comparison of simulated results by the 3D simulator with the 2-1/2D simulator developed earlier in our lab verified the correctness of the 3D simulation code. Under typical operating conditions, the simulation results give minimal surface roughness. This suggests that the nonuniformality of ion flux on the sample surface has limited effect on the formation of surface roughness. Some other mechanisms, such as micromasking, might explain the significant surface roughness experimental observed under certain operating conditions.

9.2. Suggestions for future work

To better characterize the etching kinetics of poly-silicon in HBr plasma, the role of hydrogen need to be determined. The higher etching yield for HBr plasma than Br_2 plasma has been attributed to hydrogen, but no direct evidence has been provided.

As the feature size continues to scale down, the surface roughness becomes more important. Up to now, the source of surface roughness and the subsequent transfer of the roughness has been unclear. The dependence of surface roughness on ion energy, ion incident angle, and etching chemistry should be systematically determined with beam scattering experiments.

The 3D simulator need to be further verified and modified to facilitate the feature profile simulation of 3D structure. For simplification, the feature surface has been represented by the outer edge of each cell, which may result in severe distortion of ion and neutral fluxes. A better mechanism might be to fit a local 3D surface to the neighboring cells of the cell of interest and calculate the intersection of incoming particle with the surface by solving the resultant nonlinear equation.

The 3D simulation might help us to understand the surface roughness. But to capture the surface roughness, the etching kinetics we measured macroscopically, i.e. the etching yield as a function of neutral-to-ion flux ratio, ion energy, ion incident angle, etc., might not be enough. A new kinetics on a smaller length scale directly capturing surface roughness, i.e. the surface roughness as a function of various parameters mentioned above, might have to be determined and incorporated into the simulator.

Appendices

A. Mechanical drawings

	Page
Photo of the plasma beam apparatus	164
The plasma beam source	
3D view (010-001)	165
Top view (010-002)	166
Front view (010-003)	167
Cross-section view 1 (010-004)	168
Cross-section view 2 (010-005)	169
Extraction grid holder (015-001)	170
Quartz plate (020-001)	171
Quartz liner	
Front view (030-001)	172
Cross-section view 1 (030-002)	173
Cross-section view 2 (030-003)	174
Quartz plate holder metal piece 1	
Top view (060-001)	175
Cross-section view (060-002)	176
Quartz plate holder metal piece 2	
Top view (070-001)	177
Cross-section view (070-002)	178
Coil (080-001)	179
Teflone ring	
Top view (100-001)	180
Cross-section view (100-002)	181
Mass spectrometer housing	
3D view	182
Front view	183

Photo of the plasma beam apparatus

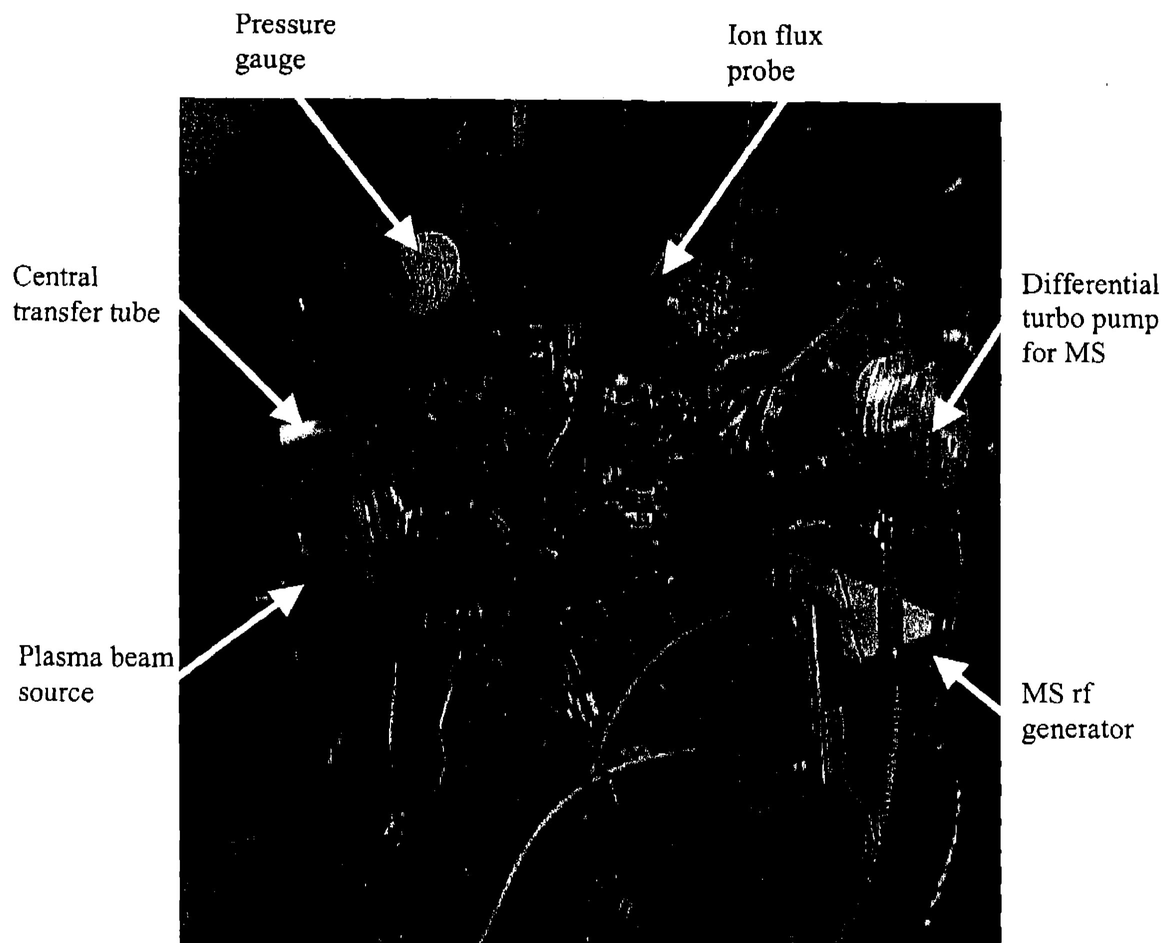

3D view of the plasma beam source (010-001)

Drawing # 010-001

Material: SS-304

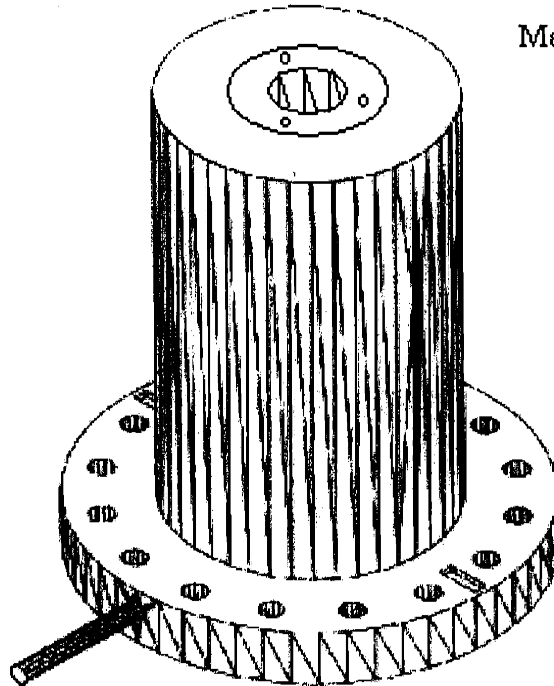

Top view of the plasma beam source (010-002)

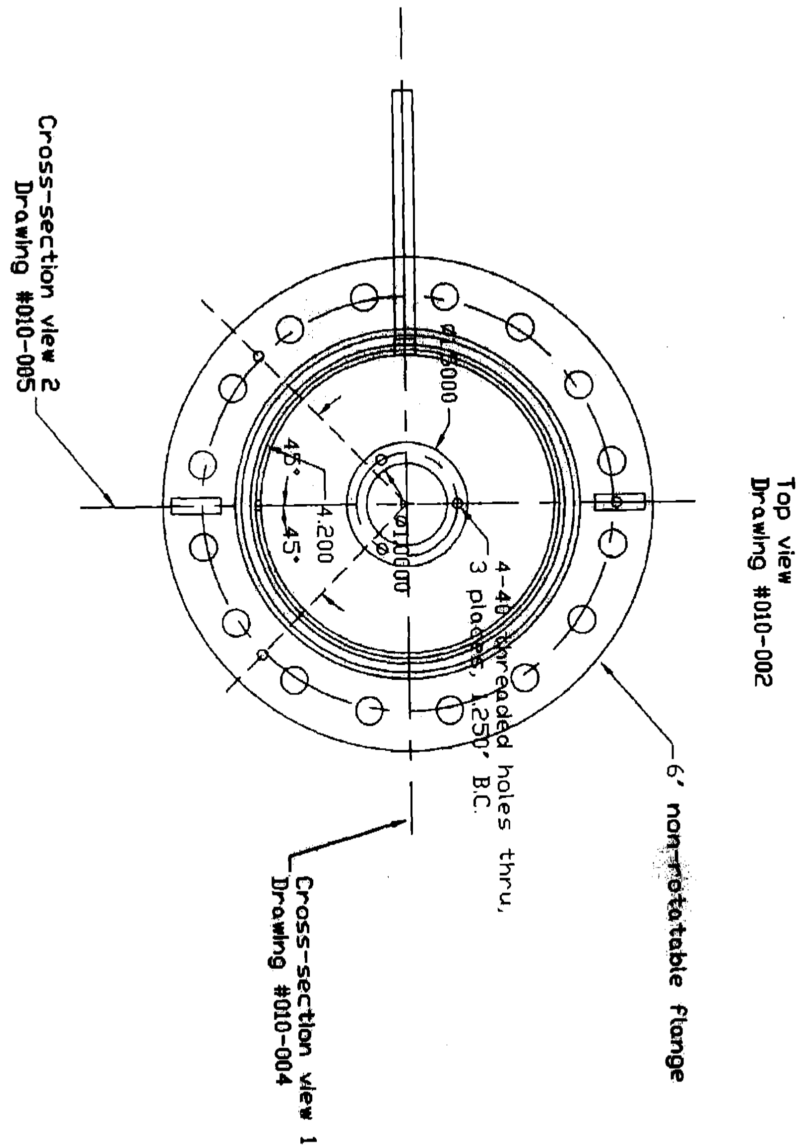

Unless specified, tolerances are -/+0.005' for distance, -/+0.1 degree for angle.

Front view of the plasma beam source (010-003)

Front view
Drawing #010-003

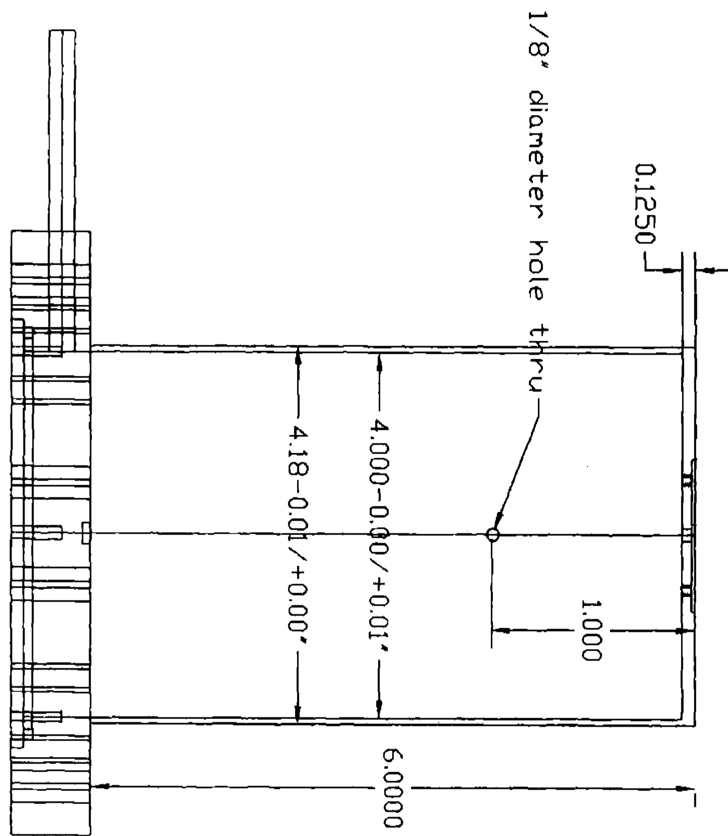

Unless specified, tolerances are -/+0.01" for distance.

Cross-section view 1 of the plasma beam source (010-004)

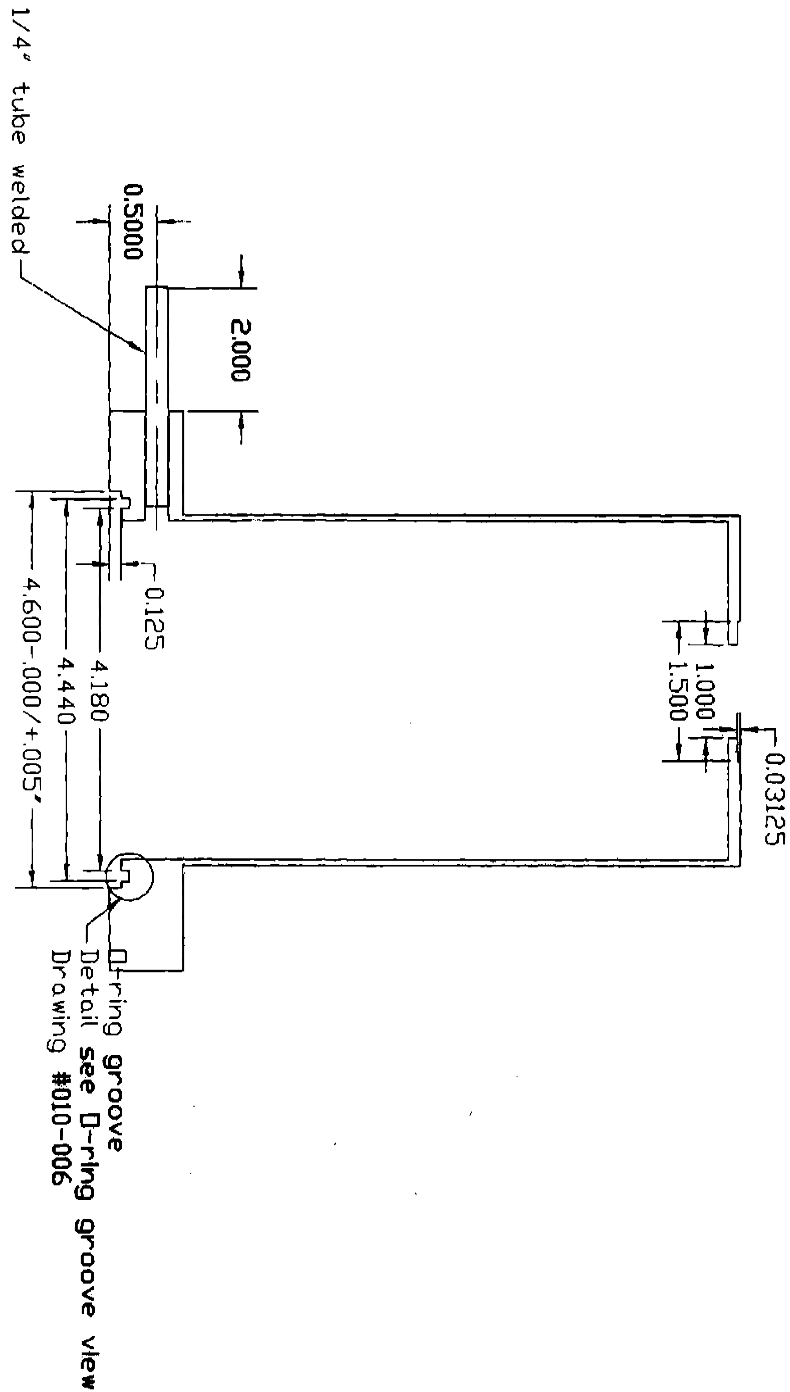

Unless specified, tolerances are -/+0.005" for distance.

Cross-section view 2 of the plasma beam source (010-005)

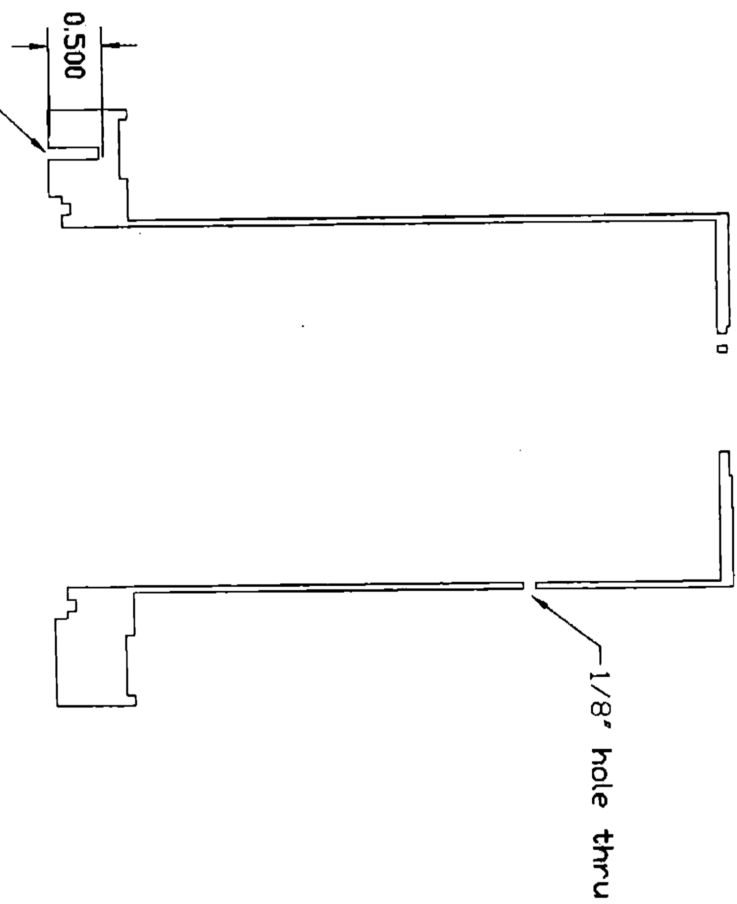

Extraction grid holder (015-001)

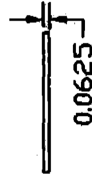

Metal piece
Drawing #015-001
Material: SS-304

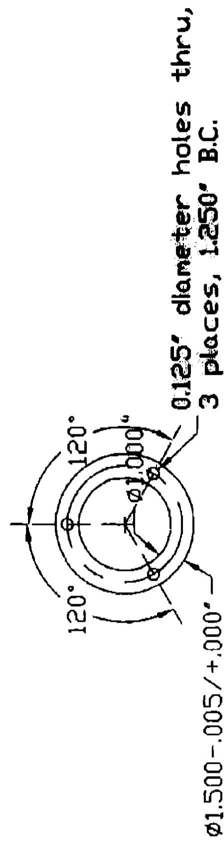

Unless specified, tolerances are -/+0.005" for distance, -/+0.1 degree for angle.

Quartz plate (020-001)

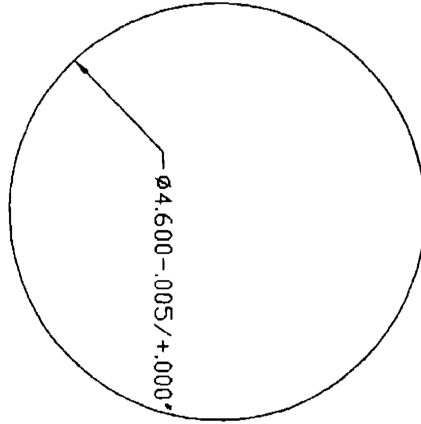

Quartz plate
Drawing #020-001

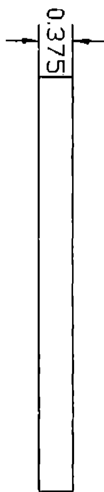

Unless specified, tolerances are -/+0.005" for distance.

Quartz liner (030-001)

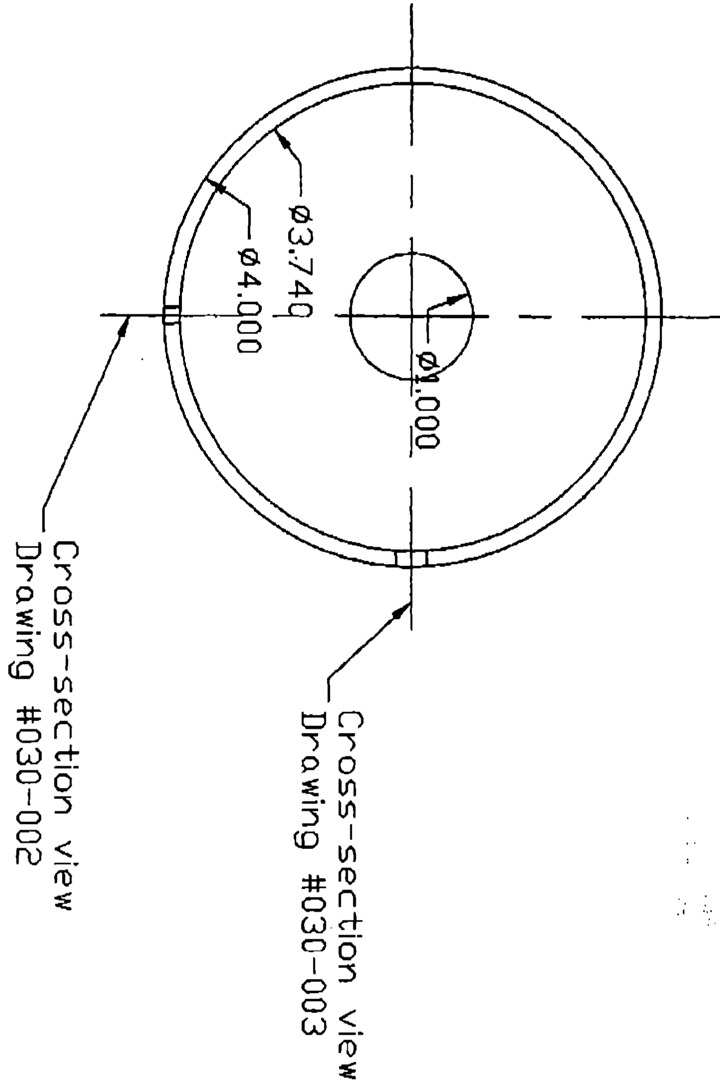

Cross-section view 1 of the quartz liner (030-002)

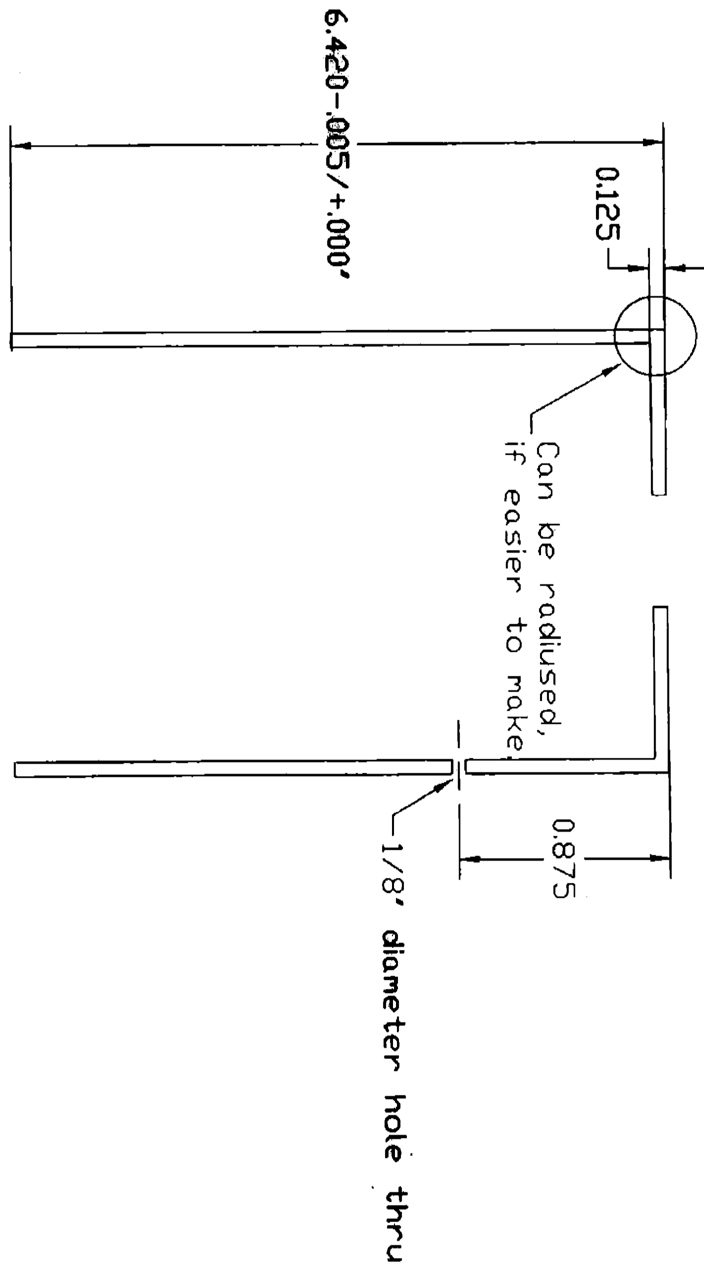

Unless specified, tolerances are -/+0.005' for distance.

Cross-section view 2 of the quartz liner (030-003)

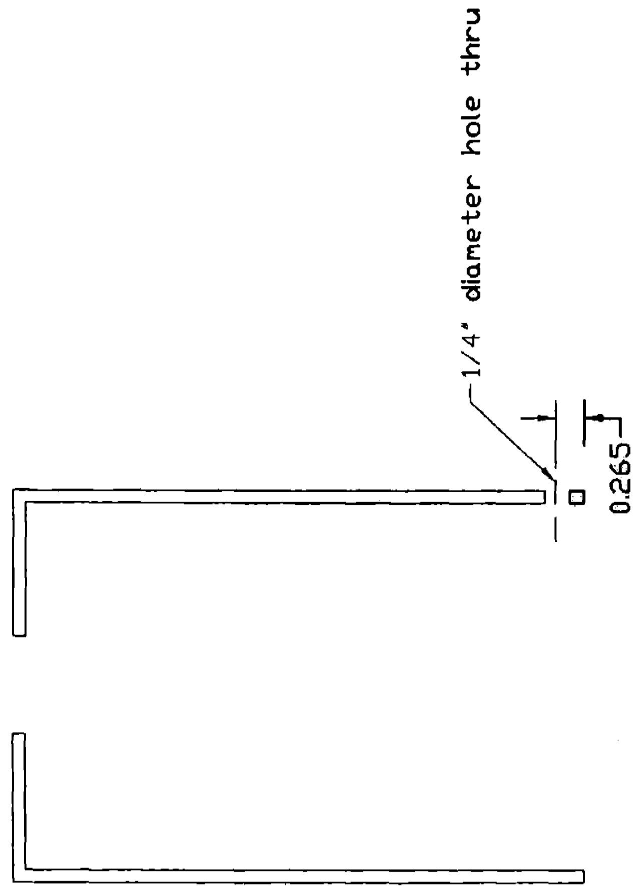

Top view of the quartz plate holder metal piece 1 (060-001)

Metal piece 1
Drawing #060-001
Material: Aluminium alloy

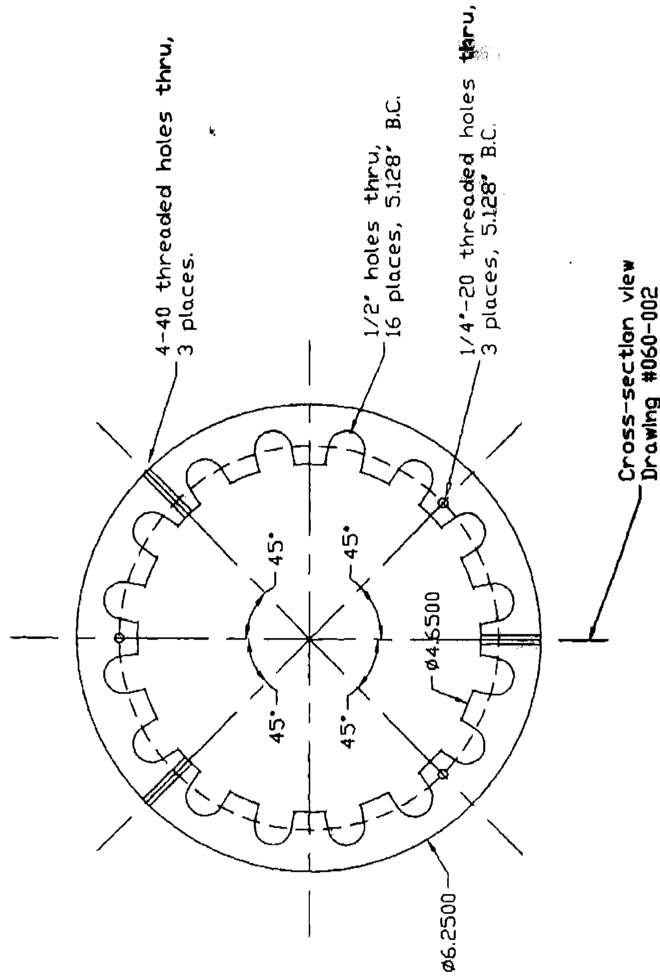

Unless specified, tolerances are -/+0.01" for distance, -/+0.1 degree for angle.

Cross-section view of the metal piece 1 (060-002)

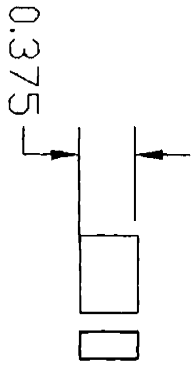

Cross-section view for metal piece 1
Drawing #060-002

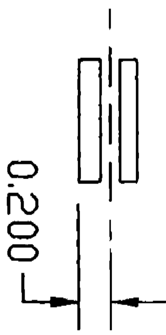

Unless specified, tolerances are -/+0.01" for distance.

Top view of the quartz plate holder metal piece 2 (070-001)

Metal piece 2
Drawing #070-001
Material: Aluminium alloy

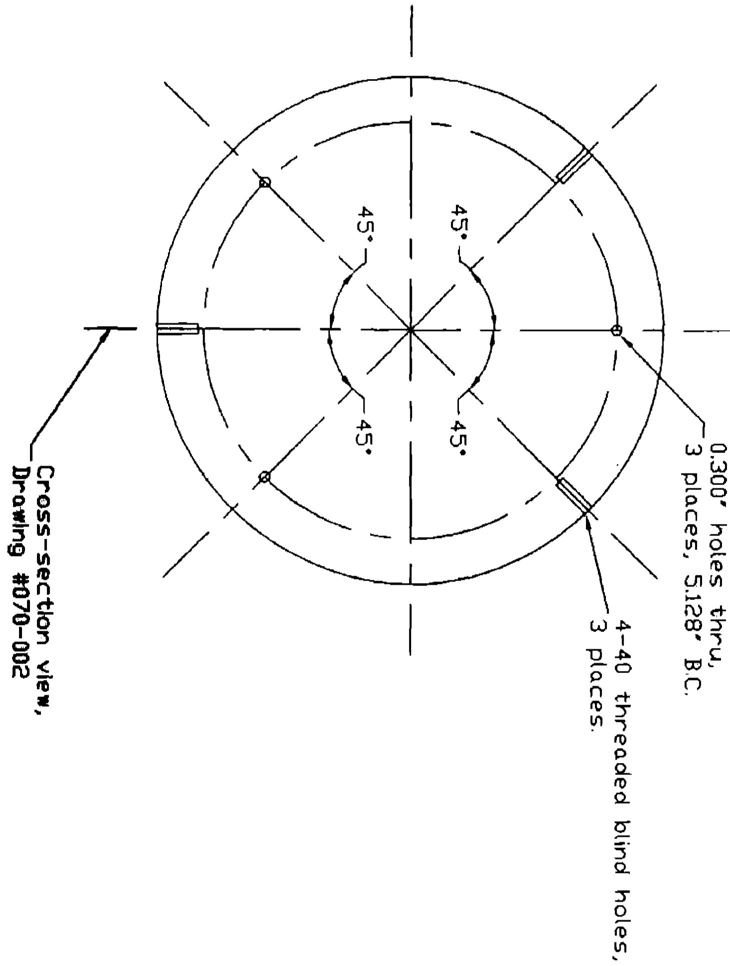

Unless specified, tolerances are -/+0.01" for distance, -/+0.1 degree for angle.

Cross-section view of metal piece 2 (070-002)

Cross-section view for metal piece 2
Drawing #070-002
Material: Aluminium alloy

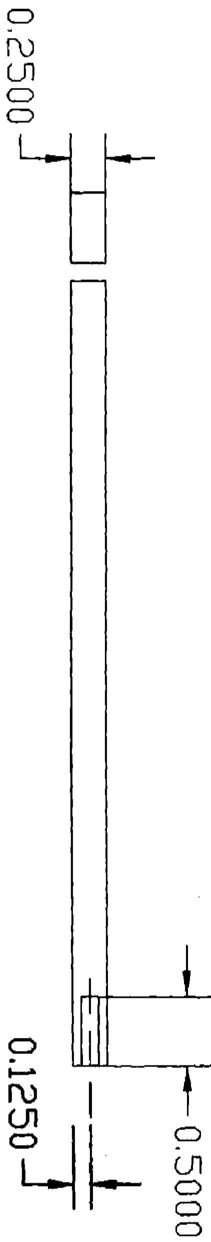

Unless specified, tolerances are -/+0.01" for distance.

Coil (080-001)

3/16" thick coil
Drawing #080-001
Material: Copper

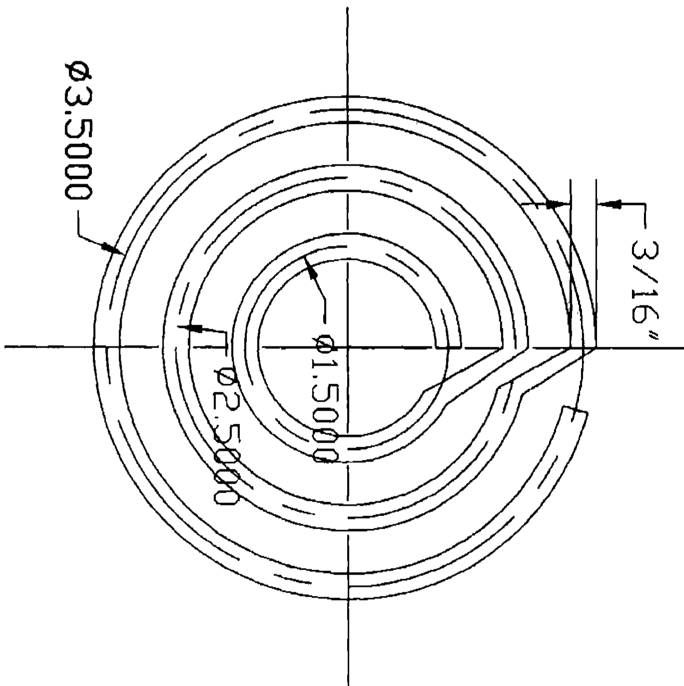

Unless specified, tolerances are -/+0.1" for distance.

Top view of the teflone ring (100-001)

Teflone ring
Drawing #100-001
Material: Teflone

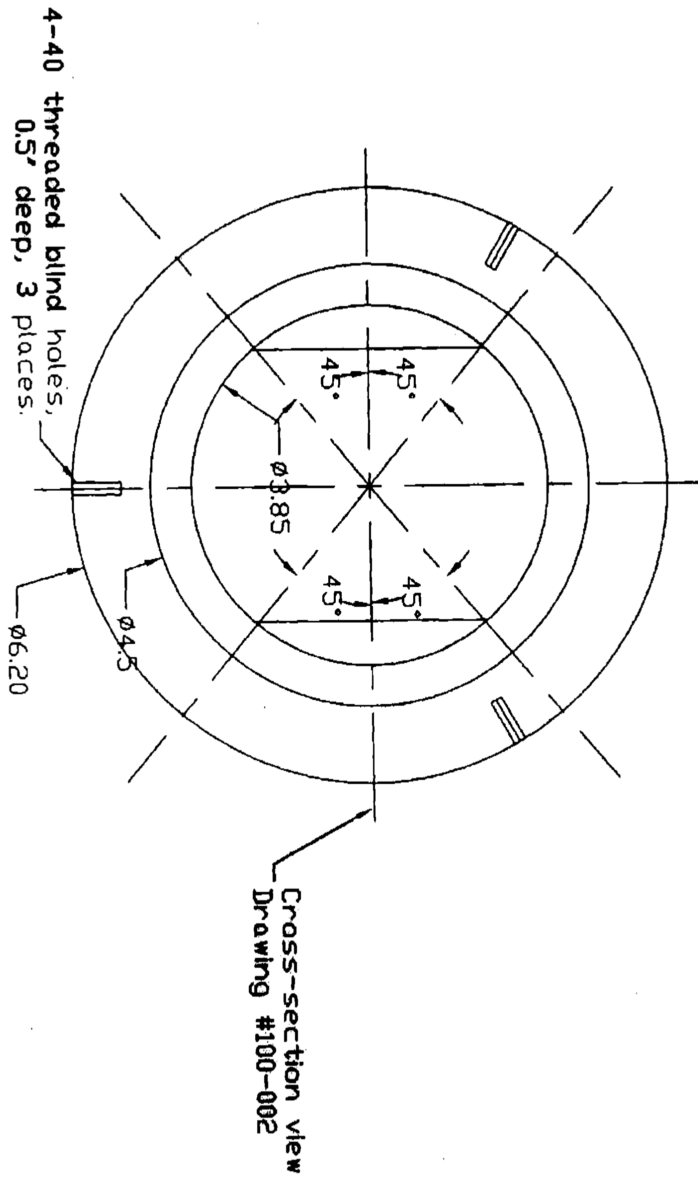

Unless specified, tolerances are -/+0.01" for distance, -/+1 degree for angle.

Cross-section view of the teflone ring (100-002)

Cross-section view
Drawing #100-002

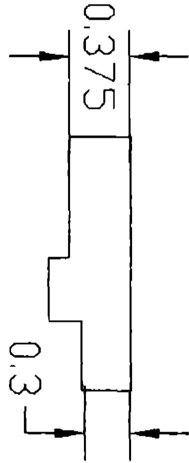

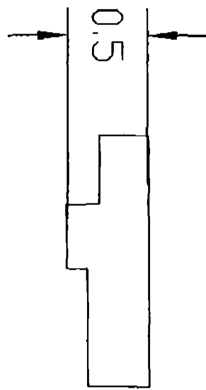

Unless specified, tolerances are -/+0.01" for distance.

3D view of MS housing

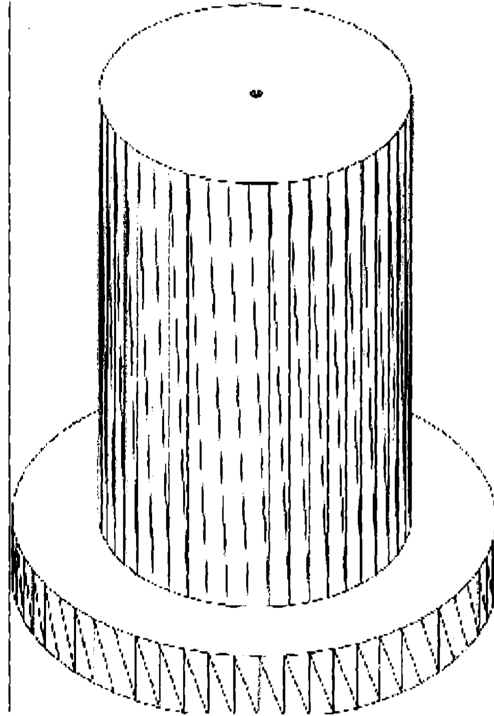

Front view of the MS housing

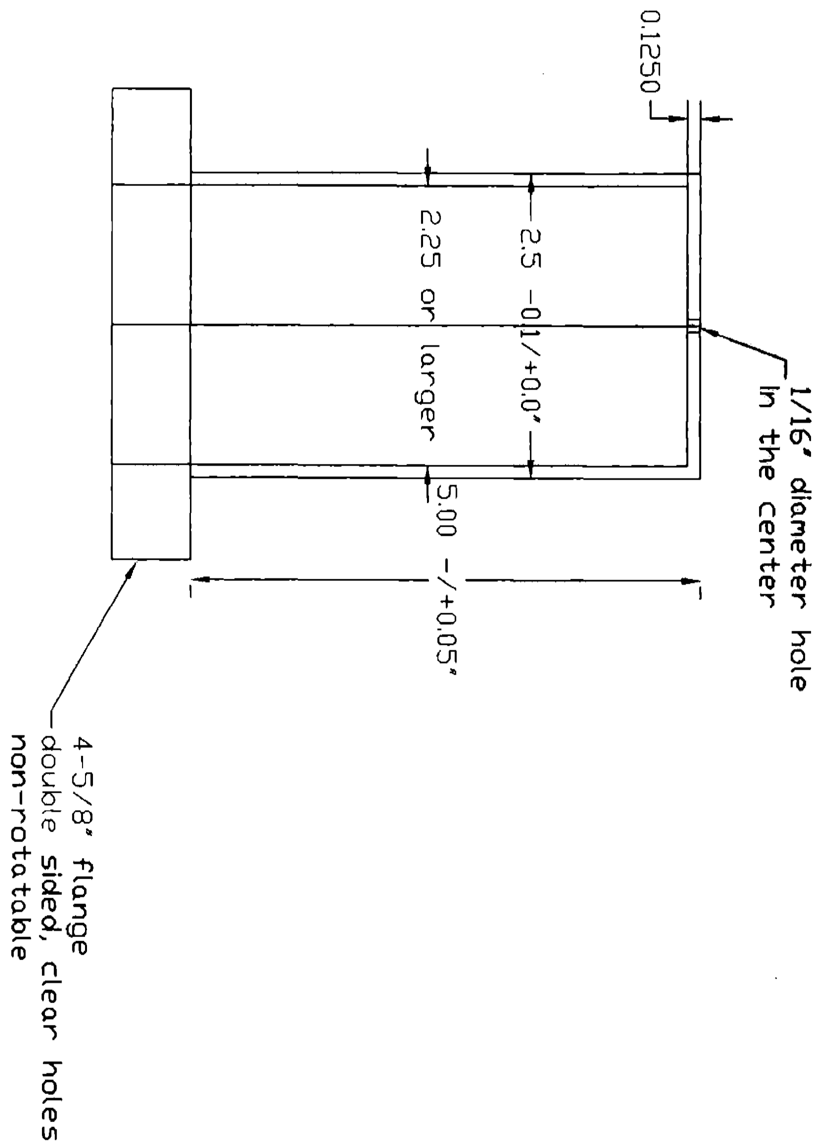

B. Operating Procedure for Plasma Beam Chamber

Plasma Beam Source

- Check chamber pressure ~$1x10^{-8}$ torr after overnight bake
- Check cooling water (plasma power supply and plasma beam source)
- Pump out gas lines to base pressure ~ 30 mtorr
- Open diapharm valves all the way to the gas cylinder
- Turn on gas flow
- Turn on plasma power supply
- Check if there is a glow discharge visible
- Turn on acceleration voltage
- Measuring ion current with gridded probe

Regenerate the Cryo Pump

- Close the gate valve to the pump (keep the main chamber at rough vacuum)
- Shut down the compressor
- Open the roughing valve to the corrosive line
- Allow the pump to warm up to room temperature
- Bake the pump overnight (~70C)
- Turn heating tape off
- Wait till the temperature cools down to room temperature
- Check the Helium pressure and recharge if necessary
- Check the base pressure on the corrosive line ~100 mtorr
- Close the roughing valve
- Turn on the compressor
- Temperature of the pump should reach 15K within 2 hours
- Rough out the main chamber down to base pressure
- Open the gate valve

Emergency Shutdown of Reactive Scattering Reactor

- Valve off all gas feeds to chamber at the gas manifold
- Valve off corrosive gas flows at the cylinder
- Close the gate valve to the turbo pump
- Turn off the turbo pump controller
- Turn off all the electronics

Emergency Shutdown of Reactive Scattering Reactor

In case of a power outage:

From running –

- Ensure the gate valve between the chamber and the cryo is closed.
- Valve off all the gas feed lines to the scattering chamber.
- Turn off all the electronics
- Turn off the compressor

- Valve off the chlorine, HBr and $SiCl_4$ gas line
- Evacuate the lab

From standby –

- Ensure the gate valve between the chamber and the cryo is closed.
- Turn off all the electronics
- Turn off the compressor
- Evacuate the lab